



Final Design Package

CU Hyperloop
University of Colorado Boulder
November 9th, 2024

SKO BUFFS!!

Contents

I Team Overview	4
I.A Subteams	5
I.B Team Members	5
I.B.1 Business Development	5
I.B.2 Marketing	5
I.B.3 Fluids	5
I.B.4 Propulsion	5
I.B.5 Structures	5
I.B.6 Integration	5
I.B.7 Soil Removal	5
I.B.8 Tunnel Support	5
I.B.9 Circuits	5
I.B.10 Software	5
I.C Team Advisors	5
II Top Level Design Description	6
II.A Improvements	7
II.A.1 Motor Controller	7
II.A.2 Grippers	7
II.A.3 RIMU	8
II.A.4 Other Improvements	8
III System Modeling	8
III.A Soil Modeling	8
III.B Friction Analysis	9
III.B.1 Coefficient of Friction	9
III.B.2 Friction Calculations	9
III.B.3 Results of Analysis	10
III.C Dynamics Modeling	11
III.C.1 Teeth Penetration	11
III.C.2 Net Thrust Force	11
III.C.3 Cutting Head Torque	11
III.D Dig Path	12
III.D.1 Turning Analysis	12
III.E Full System Modelling	13
III.F Dig Time Estimation	15
IV Excavation System	15
IV.A System Overview	15
IV.B Cutting Head	15
IV.B.1 Cutting Head Plate	16
IV.B.2 Cutting Head Teeth	16
IV.C Drive System	17
IV.C.1 Motor	17
IV.C.2 Gearbox	17
IV.C.3 Load Path	17
IV.D Excavation Analysis	18
V Propulsion System	19
V.A New Features	19
V.B Grippers	20
V.C Chains	20
V.D Fabric and Velcro	21

V.E	Fixtures to Structure	21
V.F	Plate Tearout	22
V.G	Pneumatics	22
V.H	Pneumatic Circuit	23
V.I	Hexapod	23
V.J	Hexapod Angles FBD	24
V.K	Actuator and Ball/Socket loads	24
VI	Cooling System	26
VI.A	System Overview	26
VI.B	P&ID	26
	VLB.1 Cooling Plate and Cooling Blocks	27
	VLB.2 Motor Cooling System	27
	VLB.3 PCB Chips Cooling	28
	VLB.4 Cooling Shell	28
	VLB.5 Heat Exchanger (Water Chiller)	29
	VLB.6 Pumps	29
VI.C	Analysis	29
	VI.C.1 Cooling Shell Heat Analysis	29
	VI.C.2 Cooling Shell Geometry Analysis	30
	VI.C.3 Cooling Shell Fluid Analysis	30
	VI.C.4 Steady Heat Temperature Analysis	31
VII	Soil Removal	31
VII.A	System Overview	31
VII.B	Vacuum Chamber	31
VII.C	Clog Detection	32
VII.D	Material Path	32
	VII.D.1 Agitators	32
	VII.D.2 PVC Extension Fitting	33
VII.E	Soil Lab	34
VII.F	Soil Settlement	34
VIII	Ground Condition System	34
VIII.A	System Overview	34
VIII.B	P&ID	35
	VIII.B.1 ACP 214	35
	VIII.B.2 Pump	35
	VIII.B.3 Flowmeter	36
	VIII.B.4 Drainage Line	37
VIII.C	Analysis	37
IX	Tunnel Support	38
IX.A	Tunnel Support Overview	38
IX.B	Support Segments	38
IX.C	Filament Extrusion	39
IX.D	R axis	43
IX.E	Z axis	44
IX.F	Theta Axis	45
IX.G	Segment Ejection	46
X	Structural Design and Analysis	48
X.A	System Overview	48
X.B	Front Structure	48
X.C	Hexapod Shell	51

X.D	Rear Structure	54
X.E	DAWGS	58
X.F	Manufacturing and Assembly	58
XI	Launch Structure	59
XI.A	Launch Structure Overview	59
XI.B	Tilt Frame	59
XI.C	Launch Structure Analysis	62
XI.D	Equipment Lifting and Transport Structural Analysis	64
XII	Software System	65
XII.A	Overall Overview and Architecture	65
XII.B	Hexapod	67
XII.C	Grippers	68
XII.D	Excavation	68
XII.E	GUI	69
XII.F	Testing	72
XII.G	Mqtt Broker	72
XII.H	Tunnel Support	73
XII.H.1	Overview	73
XII.H.2	Hexapod Reliance	73
XII.H.3	Control Design Overview	73
XII.H.4	Theta Axis Simulation and Tuning	76
XIII	GNC System	81
XIII.A	Guidance	81
XIII.A.1	Dig Path	81
XIII.A.2	Trajectory Planner	81
XIII.B	Navigation	84
XIII.B.1	Inclinometers	84
XIII.B.2	Inertial Measurement Units	84
XIII.B.3	Sensor Fusion - Unscented Kalman Filter	90
XIV	Electrical System	92
XIV.A	General Philosophy	92
XIV.B	Printed Circuit Board Overview	92
XIV.B.1	Hexapod Board	92
XIV.B.2	Tunnel Support Board	93
XIV.B.3	Excavation Board	94
XIV.B.4	Rotational Inertial Measurement Unit (RIMU) Board	96
XIV.B.5	Front Inclinometer Board	98
XIV.B.6	Rear Gripper Board	100
XIV.B.7	Segment Ejection Board	102
XIV.B.8	Ground Conditioning System (GCS) Board	103
XIV.B.9	Pneumatic Board	105
XIV.B.10	Power Board	106
XIV.B.11	Cooling Board	108
XIV.C	Excavation Harnessing	109
XV	High Power	110
XV.A	General Overview	110
XV.B	Power Budget	110
XV.C	Protective Equipment	110
XV.D	2 Step Re-energization	111
XV.E	Completed	113

XVI TBM Production Schedule	113
XVI.A Provide a Breakdown of What Has Been Produced Already vs What Still Needs to Be Produced	113
XVI.B Already Produced	113
XVI.C Needs to Be Produced	113
XVII Full TBM Functional Test Program	114
XVII.A Provide Minimum Viable Test Plans for Critical Machine Systems	114
XVII.B Provide All Available Test Results of Tests Already Conducted	114
XVIII Hazardous Materials	114
XVIII.A None	114
XIX Materials Injected into the ground	115
XIX.A ACP 214	115
XX Description of Safety Features	115
XX.A Mechanisms to mitigate a Complete loss of TBM Power	115
XX.B Single Points of Failure withing the TBM	115
XX.C Recovery Plan if TBM becomes Immovable	115
XX.D Description of Failure Modes	115
XX.E Descriptions of Safety Interlocking Mechanisms	116
XXI Budget and Financial Overview	116
XXI.A Total Budget for 2024-2025 Competition Season	116
XXI.B Current Financial State	116
XXI.C Funding Plan	116
XXI.C.1 Current Industry Sponsors and Contribution Level	116
XXI.D Team Sponsors	116
XXI.E Anticipated Expenses	117
XXI.F Summary	119

Nomenclature

ADC	=	Analog to Digital Converter
GUI	=	Graphical User Interface
IMU	=	Inertial Measurement Unit
PCB	=	Printed Circuit Board
TBC	=	The Boring Company
TBM	=	Tunnel Boring Machine
Hexapod	=	Stewart Platform
FEA	=	Finite Element Analysis
UTS	=	Ultimate Tensile Strength

I. Team Overview

CU Hyperloop is a student team from the University of Colorado Boulder. Founded in 2017, the team competed in both the 2018 and 2019 SpaceX Hyperloop Pod Competition in addition to the 2021, and the 2022-2024 Not-A-Boring Competition. CU Hyperloop maintains a strong presence on our team website (<https://www.cuhyperloop.org/>) and operates our own social media accounts on Instagram and LinkedIn (@CUHyperloop). Our mission is to push the boundaries of high-speed, cost-effective tunneling while empowering the next generation of engineers through real-world challenges.

A. Subteams

The team is composed of 8 subteams that each focus on a primary area of the project. The subteams are **Excavation**, **Business Development**, **Marketing**, **Fluids**, **Propulsion**, **Structures**, **Soil Removal**, **Tunnel Support**, **Circuits**, and **Software**. These subteams usually split into functional work groups (e.g. guidance group, high power group) to address each sub-system concern. We also conduct design reviews with external advisors and sponsors. This serves to not only make time to review our designs but also bring in outside ideas and suggestions from the engineering industry. The overall team structure is needed to enable all project parts to receive adequate attention. To ensure communication between subteams, the team has set up communication systems such as Slack and weekly all-team presentations where each subteam presents weekly progress, and the team discusses future work. These measures create a fluid and collaborative work environment that results in a large surface area for ideation.

B. Team Members

Project Manager: Zaphod Schmidt

Chief Engineer: Mateo Medellin

1. Business Development

- 1) **Lead:** Matis Uhl de Morais
- 2) John Gonzales
- 3) Jake Copeland
- 4) Jacob Smith
- 5) Jonas Ho
- 6) Hampton Langenbeck

2. Marketing

- 1) **Lead:** Matis Uhl de Morais
- 2) Parker Allen
- 3) Lily Scott
- 4) Tashi Sherpa

3. Fluids

- 1) **Lead:** Ahmed Zahid
- 2) Mario Castro
- 3) Kedar Manoj

4. Propulsion

- 1) **Lead:** Mateo Medellin
- 2) Landon Holligan
- 3) Anselme Idoine
- 4) Isaac Kness
- 5) Raaghav Lele

5. Structures

- 1) **Lead:** Ben Archuleta
- 2) Henry Spradlin
- 3) Jeffrey Reiling
- 4) Maryann Gorka

6. Integration

- 1) **Lead:** Nikita Johnson
- 2) Floating members from other subteams

7. Soil Removal

- 1) **Lead:** Ahmed Zahid
- 2) Floating members from other subteams

8. Tunnel Support

- 1) **Lead:** Chris Hildebrand
- 2) Alex Jamka
- 3) Alex Jangro
- 4) Ethan Kravig
- 5) Berkley Huffman

9. Circuits

- 1) **Lead:** Alex Kistamma
- 2) Christian Green
- 3) Jeffrey Allen
- 4) Bilim Sydykov
- 5) Anthony Hamamji
- 6) Samir Dherar

10. Software

- 1) **Lead:** Mason Choi
- 2) Vishnu Duriseti
- 3) Adlai S
- 4) Melanie Porter
- 5) Annika Polavarapu
- 6) Harika Kondur
- 7) Jason Swartz
- 8) Joey Weber
- 9) Joseph Wallace
- 10) Renata Zurita
- 11) Zachary Robinson

C. Team Advisors

- 1) Bobby Hodgkinson

2) Henry Scott

II. Top Level Design Description

CU Hyperloop designed a micro Tunnel Boring Machine that excavates a tunnel with a minimum of a 0.54 m useful tunnel diameter. The dirt is excavated using a 0.63 m high-strength steel cutting head that is recessed into the body of the TBM. The cutting head is powered by a single brushless DC electric motor connected to a 1:59 gear reducer. The TBM is propelled into the dirt by 6 electric linear actuators arranged in a Stewart platform configuration otherwise known as a hexapod. As the TBM moves forward, soil enters the removal chamber directly behind the cutting head. In the soil chamber, the soil is agitated by 3 steel agitators attached to the cutting head shaft. The soil is then pumped to the surface using an industrial dry vacuum capable of removing 30 gallons of soil per minute. To keep the TBM from sliding backward, a set of inflatable grippers locks the back of the machine into the surrounding soil using a pair of bike tubes surrounded by an abrasion-resistant material and steel chain. After the hexapod has successfully extended, the rear grippers retract and a set of front grippers locks the front of the machine into place while the back is pulled forward. This inchworm motion occurs 185 times throughout the 37.5 m tunnel dig. Note that this is the total length that the TBM must move from the initial launch to the beginning of retrieval operations to ensure that the shortest distance between tunnel entrance and exit is 30 m. A full dig path can be seen in figure 5. While the TBM is being pushed and pulled forward, a 0.584 m diameter cylindrical robot-style 3D printer is printing an 8-inch long tunnel support section. As the machine moves underground, each pull prompts 6 linear actuators to push out the printed tunnel support section. This 0.584 m diameter plastic tube fills the area where the back section of the machine is being removed. Over the dig a total of 162 rings will be used and 60 kgs of PLA will be printed.

The TBM is 3.85 m long and weighs approximately 830 kilograms. The structure of the TBM is composed of 8 distinct sections which are separable from each other for maintenance. These sections are bolted to each other to ensure easy removal. In the front of the machine, there is the forward section which contains the soil removal chamber, the front three grippers, and 2 of our electrical boards. Right behind that is the gearbox section. This section primarily serves to be the mounting location for the gearbox for the cutting head drive system. Behind the gearbox section is the hexapod. The hexapod is enclosed in an articulating shell that protects the soil from collapsing. Behind the hexapod, which performs both forward thrust and steering, is the back gripper section. This section is where the three back grippers are mounted. In addition, it also serves as the main electrical mounting location for controlling the hexapod and excavation drive system. The backmost section of the TBM is the tunnel support section. This section itself is composed of 2 subsections. The first section is the storage section where power supplies, manifolds, theta motors, network switches, and contactors are stored. The second section is the tunnel support 3D printer part of the TBM comprised of a large slewing bearing and two R and Z movement axis arms that print a plastic tunnel segment on an aluminum water-cooled shell. The last part of the machine is the DAWG(gantry) which is a small cart that is pulled behind the machine and routes all the umbilicals into the machine properly.

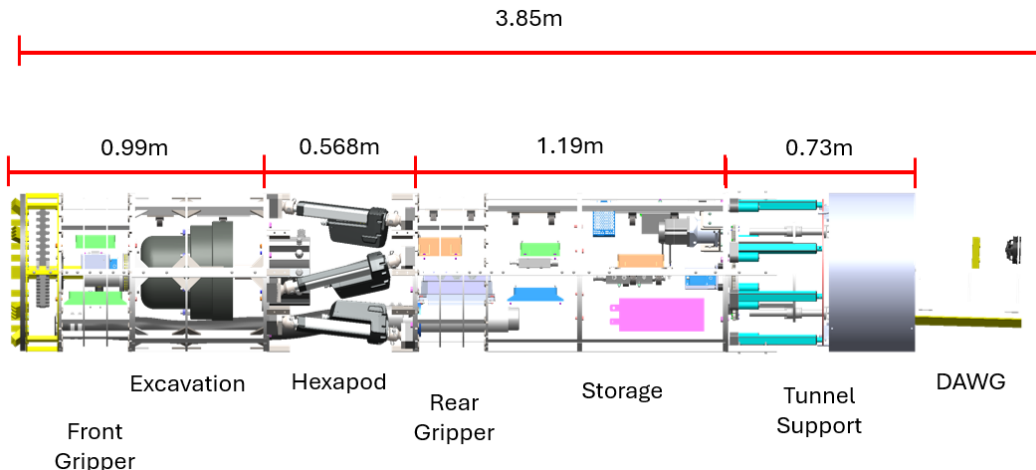


Fig. 1 Overall Machine Dimensions

Excavation	200kg
Propulsion	55kg
Tunnel Support	90kg
Structure	485kg
Total	830kg

Table 1 Mass Budget of Machine

Onboard sensors and control units enable the autonomous navigation and operation of the TBM. The state of the machine is computed through a sensor fusion of hall effect sensors on the hexapod, inclinometers, IMUs, and more. In addition to position, sensors are also used to measure the health of the machine measuring the temperature within the machine in addition to metrics such as the amount of soil in the soil chamber and whether or not a machine push can start. The onboard components and sensors are connected to a nodal architecture of 7 control boards that communicate with each other and the ground-station Linux computer at the surface using the Redis. The microcontroller nodes feed data to the ground-station where control commands are computed and the state of the machine is displayed on the GUI. Commands are then sent back to the nodes to be executed.

A. Improvements

1. Motor Controller

We experienced a critical failure with the motor controller we used last year. Despite thorough investigation, pinpointing the exact cause was challenging. However, we identified that a high-voltage spike from an inductive load caused electrical damage to the motor controller. When the current through an inductive load, such as a motor or a contactor coil, is suddenly interrupted, the inductor generates a high-voltage spike in the opposite direction as it attempts to maintain current flow. This spike likely damaged sensitive components, leading to incorrect transmission and interpretation of CAN frames. To prevent this issue from recurring, we installed a flyback diode between the contactor and the motor controller. This addition provides protection against voltage spikes, safeguarding the motor controller from potential electrical damage.

Furthermore, we recognized that the motor controller software we previously used was inherently flawed and difficult to integrate with our systems. As a result, we switched to a different motor controller that features open-source CAN broadcast functionality and improved software documentation. This new motor controller also offers dual control methods, providing redundant systems to ensure motor control even if one method fails. To further enhance reliability, we selected a model housed in a sealed, waterproof enclosure, protecting it from environmental exposure that could lead to electrical damage.

We also improved our wiring harness by sealing it in a custom-printed, waterproof PLA enclosure. This design not only protects the harness but also organizes the wiring to prevent short circuits. The same level of protection has been applied to the 12VDC contactor used to power the machine. Additionally, we implemented both software and hardware mechanisms to control motor activation, including flipping brakes, engaging the foot switch, and turning the key. Collectively, these enhancements have eliminated single points of failure in the excavation motor sub-assembly, significantly improving the system's robustness and reliability.

2. Grippers

Grippers, while never Christened with soil, were not only painful to build, but once built, were painful to work with/around. This was due to the mounting system and choice of fabric not being as durable as we had imagined, respectively. The gripper fabric is now name-brand Kevlar 49, with superior strength and abrasion resistance to our last aramid material. Additionally, to avoid punctures, the fabric entirely encases inner tubes now, with the only fastener being velcro to close the fabric around the tube. The gripper assembly is fastened to the structure using grade 80 transport chain.

3. RIMU

Due to an oversight in CAD, the RIMU box last year did could not be installed on the machine. We have both made the RIMU assembly smaller, and the section which houses it more accessible.

4. Other Improvements

Additional (non-critical failure mitigations) improvements include a new tunnel support system, improved manufacturing methods, managing space better (DAWG), Corrected analysis and design of launch system, and improved modularity of the machine.

Every component on the machine that was not purchased, except the cutter head, soil removal hose, and some machined hexapod components, have been redesigned. We estimate that 70% of the machine is new from last year

III. System Modeling

A. Soil Modeling

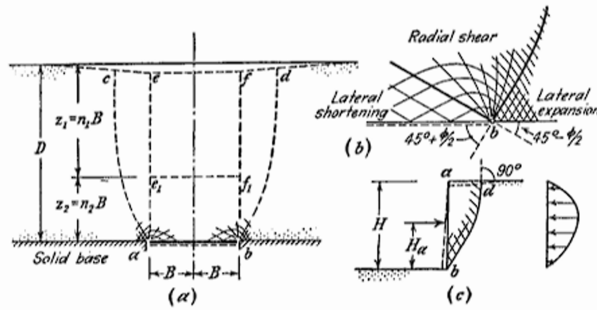


Fig. 2 Terzaghi's Soil Arching Theory

In order to effectively model the soil around the TBM, Terzaghi soil arching theory was used. This model looks at shearing resistance along the contact zone (sliding surfaces ac and bd) that develops between the yielding and the stationary soil. The pressure acting on the trapdoor (along ab) or along the top of our TBM is reduced when the yielding solid also moves down with the trapdoor. This is because the shearing resistance that keeps the soil above from caving in our tunnel keeps the yielding soil in its original position. This pressure reduction contributes to what is known as the soil arching effect. Utilizing the text Theoretical Soil Mechanics by Karl Terzaghi, the model simulates the methods outlined in Chapter 5 "Arching in Ideal Soils". With soil arching and some standard assumptions used in different industries, the expected vertical and horizontal soil pressure expected on the TBM was calculated. The variables in use are depth, active pressure coefficient K_a (Rankine's Lateral Earth Pressure coefficient K for passive, active, and static cases), and Silo width B (TBM diameter multiplied by an equation from the GB50332 Chinese national standard model assumption). To begin the modelling, Rankine's lateral earth pressure coefficients were calculated using the equations below where ϕ is the soil friction angle.

$$K_0 = 1 - \sin(\phi) \quad (1)$$

$$K_a = \frac{1 - \sin(\phi)}{1 + \sin(\phi)} \quad (2)$$

$$K_p = \frac{1 + \sin(\phi)}{1 - \sin(\phi)} \quad (3)$$

Using the provided boring logs, a ϕ value of 36.5° was used. This resulted in $K_o = 0.4052$, $K_a = 0.2541$, and $K_p = 3.93$. The other key fundamental parameter calculated was the soil silo width. This was calculated using the GB soil dynamics model with the equation below.

$$B = D(1 + \tan(45^\circ - \frac{\phi}{2})) \quad (4)$$

In this equation, D is the excavated diameter of the cutting head. For the excavated diameter of 63.5 cm, that results in a value of 0.947. In addition to these calculated constants, the boring logs were also used to find an average soil weight of 18,162 N/m³ and a cohesion constant of 3,447 Pa. These constants were then plugged into the below equations to calculate the effective vertical, and associated horizontal earth pressures acting on the TBM at different depths

$$\sigma_V = \frac{B\gamma}{K_a \tan(\phi)} (1 - e^{-K_a \tan(\phi) z/B}) \quad (5)$$

$$\sigma_{H_a} = K_a \sigma_v - 2c\sqrt{K_a} \quad (6)$$

$$\sigma_{H_p} = K_p \sigma_v + 2c\sqrt{K_p} \quad (7)$$

$$\sigma_{H_p} = K_p \sigma_v \quad (8)$$

All of this was calculated using an iterative method for different depths during our dig. Plotting the resulting soil pressures vs depth yields the following logarithmic relationship.

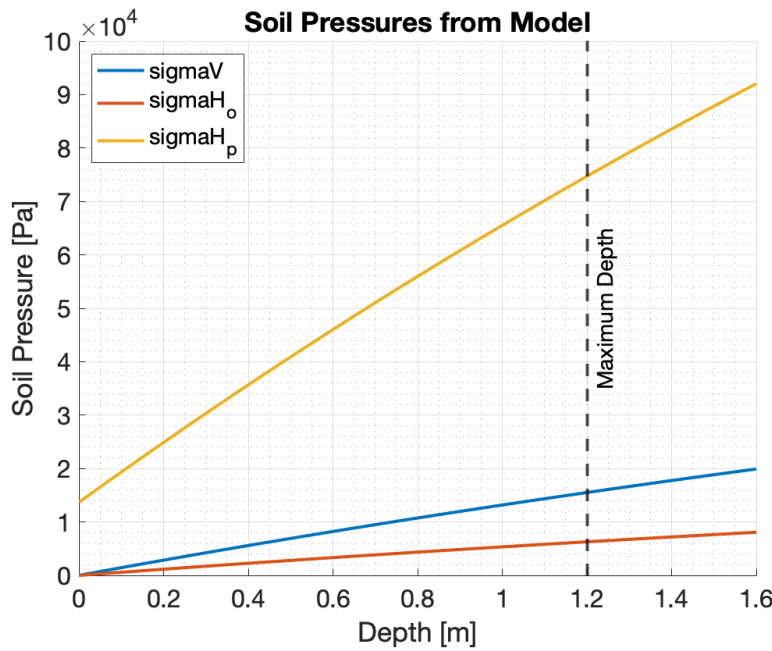


Fig. 3 Effective Soil Pressures for the TBC Boring Log

B. Friction Analysis

1. Coefficient of Friction

The coefficient of friction between steel and soil was carefully researched to ensure a proper calculation of the coefficient of friction. Using the research paper "Friction between Cohesive Soils and Steel", the team decided to use $\mu_s = 0.55$ and $\mu_k = 0.5$. In addition, the material of the grippers was determined to have a coefficient of friction of $\mu_k = 0.7$ and $\mu_k = 0.75$ based on results from "A study on the coefficient of friction of soil/geotextile interfaces."

2. Friction Calculations

The friction the TBM experiences was calculated using the coefficients of friction discussed above. More specifically, the friction was found for the front and back sections of the TBM by splitting them into subsections and then analyzing

the top and bottom halves of those subsections to find their static and kinetic friction values. The subsections and associated sections are seen in the table below.

Subsection	Associated Section
Soil Removal Shell	Front Section
Gearbox Section Shell	Front Section
Front Gripper	Front Section
Back Gripper Section Shell	Back Section
Tunnel Support Storage Shell	Back Section
Back Gripper	Back Section
Release Shell	Back Section

Table 2 Friction Sections and Subsections

These were then combined through the chain to find the overall friction values for the front and back sections. For each half of the subsections, the soil pressure was assumed to be constant with the resultant soil pressure calculated at the centroid of the half. This assumption was made to significantly reduce the complexity of the calculations. The team is confident in the validity of this assumption due to the linear nature of the relationship between soil pressure and depth on the scale of the TBM. For the horizontal pressure, the at-rest pressure was used since the TBM is neither moving into nor away from the wall of the tunnel. The total force on each top half of each subsection was calculated through the following equation, where A_{CSVert} is the vertical cross-sectional area of the subsection and A_{CSHorz} is the horizontal cross-sectional area of the subsection.

$$F_{Top} = A_{CSVert} * P_{vertical} + A_{CSHorz} * P_{horizontal_{high}} \quad (9)$$

To calculate the total soil force on the bottom half of each subsection a similar approach was used. However, instead of having a vertical pressure, the normal force of the subsection was used. This yielded the following equation

$$F_{Bottom} = F_{normal} + A_{CSHorz} * P_{horizontal_{low}} \quad (10)$$

Summing these results and multiplying by the appropriate coefficient of friction yields the following equation for the friction force acting on a single section.

$$F_{friction} = (F_{Top} + F_{Bottom}) * \mu \quad (11)$$

The results of the above equations were combined to calculate both the static and kinetic friction for both the front and back sections. The hexapod was assumed to be fully extended so that the calculated values would be the worst-case scenario. For the static friction calculations, the area of the grippers was excluded because they will be locked into the soil when the associated section is stationary.

3. Results of Analysis

Performing the analysis process detailed above resulted in the following maximum values for friction. These values occurred when the TBM was at the maximum depth of 1.2 m when measured from the center axis of the machine. Note that the reported static values of friction below do not include the grippers since when a given section is stationary the accompanying grippers will be inflated.

Section	Maximum Friction [N]
Back Section Static Friction	15040
Back Section Kinetic Friction	15108
Front Section Static Friction	7293
Front Section Kinetic Friction	7940

Table 3 Friction acting on sections of the TBM

C. Dynamics Modeling

The results of the soil model were used to create a full system dynamics model for the system to estimate key performance metrics. These metrics include the cutting head torque, friction force exerted on the machine, required forward propulsion force, and total dig time.

1. Teeth Penetration

To enable the calculation of values for all different cutting conditions a non-dimensional quantity called teeth penetration was developed and used. Teeth penetration is the measure of how much of the tooth length is actively digging dirt. It is non-dimensionalized by the height of the tooth and has units of $\frac{m}{m}$. As such, the value can range from 0 to 1 where 1 is when the tooth is fully penetrated into the dirt and 0 is when no part of the tooth is penetrated into the dirt. Using this quantity enabled the condition that the cutting head was in to be simply summed up by a single value when interested in the torque. In addition, it is also able to be used to find the total speed of the machine when multiplied by the angular velocity of the cutting head. The variable P is used to represent the value of teeth penetration in the below equations

2. Net Thrust Force

The net thrust force required for a given teeth penetration is found by summing the forces in the axial direction of the cutting head. Since the teeth contain serrations the modelled forces differ depending on if the penetration exceeded the depth of these serrations. If the penetration is less than that of a serration, the friction and shear forces need to be calculated for each serration, however if the penetration is more than the depth of the serration, the tooth can be treated as if it does not have any serrations since the force required to penetrate the tooth is very similar to if it didn't have the serrations. For the inner teeth, the following equation was used in the case without the serrations. In this set of equations, σ_{H_o} is used for the friction on the sides of the tooth since they are sliding parallel to the soil. Conversely, σ_{H_p} is used for the required force on the front face of the tooth. In the below equation $A_{ToothSideSA}$ is the surface area of the side of each tooth, $A_{teethFront}$ is the area of the tooth when looking from mining direction, E is the Young's modulus of the soil, and $L_{toothheight}$ is the height of each tooth.

$$F_{frictionSides} = \sigma_{H_o} * A_{ToothSideSA} * P * \mu_k F_{Tooth} = \sigma_{H_p} * A_{teethFront} + P * L_{toothHeight} / D * E * A_{teethFront} + F_{frictionSides} \quad (12)$$

The expression for the outer teeth varies slightly to account for the rake angle, however the overall concept remains the same. For the cutting head centerpiece, the expression remained identical, simply using different geometric parameters. In addition to the teeth, the resistance of the soil on the cutting head plate also needs to be overcome.

$$F_{Head} = \sigma_{H_p} * A_{CuttingHead}; \quad (13)$$

Finally, these results were combined in the following equation to find the total net thrust required. In this equation $N_{InnerTeeth}$ is the number of inner teeth on the cutting head.

$$F_{Thrust} = F_{Head} + F_{InnerTooth} * N_{InnerTeeth} + F_{OuterTooth} * N_{OuterTeeth} + F_{Centerpiece} \quad (14)$$

This results in a maximum net thrust force of 13383 N.

3. Cutting Head Torque

The cutting head torque was calculated by summing up all of the forces that the cutting head experiences in the radial direction. There are 2 main forces that the cutting head has to overcome, friction and the force required for a tooth to penetrate the soil. To find the force required to penetrate the soil, the strength of the soil in the plane of the tooth was multiplied by the effective cross-sectional area of the tooth to find the total force required to spin the tooth. To account for the fact that previously dug soil would be rotating with the head near the base of each tooth, the cross sectional area was split into 2 distinct components. The component that is actively cutting new soil is multiplied by the shear strength of the soil while the component that is rotating already cut soil is multiplied by the at rest earth pressure. These 2 equations are given below. In these equations $N_{Serration}$ is the amount of serrations per tooth, $P_{Serration}$ is the penetration of the serration, and $\theta_{Serration}$ is the angle of each serration.

$$A_{CSInnerActive} = P * A_{CSInner} + N_{Serration} * P_{Serration} * A_{SerrationSA} * \cos(\theta_{Serration}) \quad (15)$$

$$A_{CSInnerInactive} = A_{CSInner} + N_{Serration} * P_{Serration} * A_{SerrationSA} * \cos(\theta_{Serration} - A_{CSInnerActive}) \quad (16)$$

To find the shear strength of the soil the following equation was used where C is the cohesion constant of the soil.

$$\tau = C + \sigma_{H_o} * \tan(90 - \phi) \quad (17)$$

To calculate the friction on each of the cutting teeth the following equation was used. Teeth penetration does not factor into this equation since regardless of penetration the tooth is always surrounded by soil.

$$F_{fTooth} = A_{ToothSideSA} * \sigma_{H_o} + \sigma_{H_p} * A_{ToothEndSA} \quad (18)$$

Next, the results of the above equations were all combined in the equation below to get the total force acting on each tooth in the radial direction.

$$F_{Tooth} = F_{fTooth} + \tau * A_{CSInnerActive} + A_{CSInnerInactive} * \sigma_{H_o} \quad (19)$$

Finally, this result was multiplied by the distance from each tooth to the center of rotation to get the torque value

Another component of the torque is the friction on the cutting head plate. This was calculated using the passive earth pressure and multiplying it by the average distance the plate was from the center of rotation. This value was found to be 0.2051 m.

$$T_{fHead} = \mu * \sigma_{H_p} * A_{CuttingHead} * L_{midpoint} \quad (20)$$

The last primary component of the torque on the cutting head originates from the shear force in the cutting head openings. The equation used to calculate this component is seen below where $A_{ShearOpening}$ is the total shear area across all of the holes in the cutting head

$$T_{Opening} = A_{ShearOpening} * \sigma_{H_o} * L_{midpoint} \quad (21)$$

Finally, all of the torques due to the individual components were added together to get the total torque required.

D. Dig Path

The dig path is such that the machine launches from the surface, performs a 30 m radius turn to flat at a 1.2 m depth, travels the required distance forward, and then climbs to the surface. A 1.2-meter depth was chosen because the forces on the machine increase with depth. However, going shallower than 1.5 tunnel diameters from the top of the tunnel means that the tunnel is more likely to collapse due to the arching effect on the soil not being as present.

1. Turning Analysis

The machine is capable of doing a turn with a radius of 20 meters. At this radius both the front and back sections of the machine fit within the excavated diameter of 63.5 cm. This is illustrated in the image below.

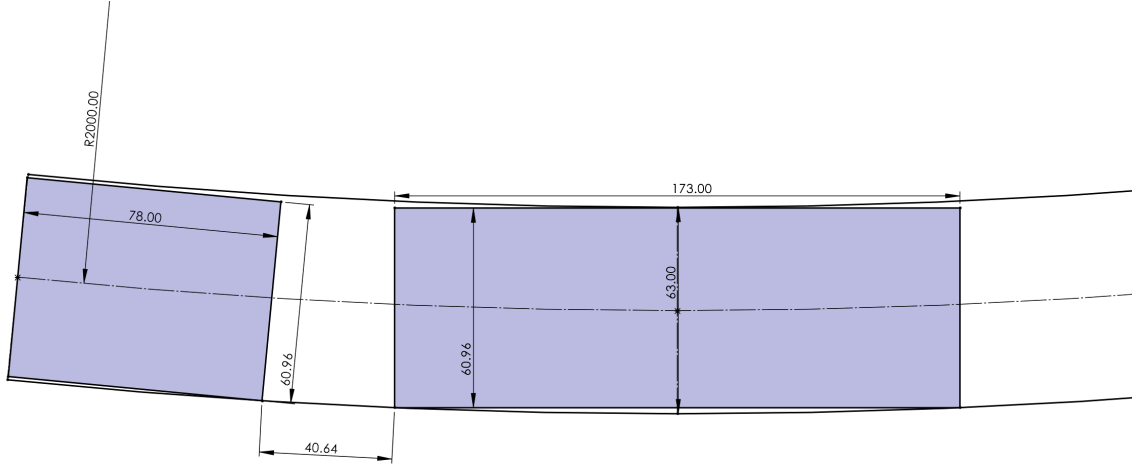


Fig. 4 Turning Analysis for the TBM

The nominal turn radius of the dig path was set at 30 meters. This was done so that in the event that the TBM gets off course, it is able to execute a tighter turn than nominal in order to get back on track. The full dimensioned dig path is seen below. The total length including launch and retrieval is 37.5 m.

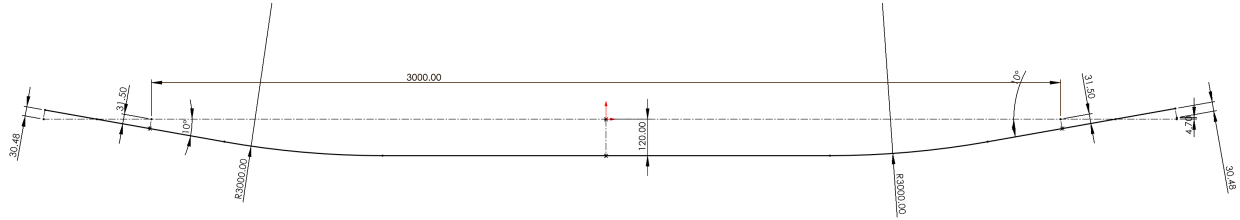


Fig. 5 Expected machine dig path

E. Full System Modelling

To figure out the dynamics of the system over the dig the above 2 models are combined to form a single cohesive model. As mentioned in the teeth penetration section, the speed of the TBM can be calculated through the following equation where L is the height of the cutting teeth.

$$V_{CuttingHead} = T * \omega * L \quad (22)$$

In addition, the speed can also be calculated via the actuators. The Relationship between the force and speed of the actuators is linear and is given by the follow equation.

$$V_{Hexapod} = V_{Actuator_{max}} + \frac{F_{Thrust}}{6} * \frac{(V_{Actuator_{min}} - V_{Actuator_{Max}})}{F_{Actuator_{max}}} \quad (23)$$

As mentioned earlier, F_{Thrust} is a function of teeth penetration. One will notice that for an arbitrarily selected value of teeth penetration, the speed calculated via the hexapod and the cutting head will not align. Physical reality dictates that these two values be identical and indeed for a certain range of teeth penetrations this is true. By finding the maximum penetration value for which the velocities agree, the fastest possible state of the TBM is determined. This idea can be seen in the diagram below.

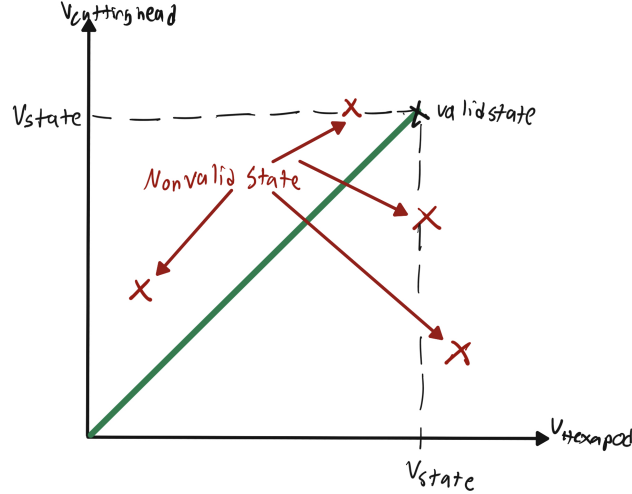


Fig. 6 Teeth Penetration States

The maximum value of T that satisfied the convergence was calculated across the dig path. This returned a vector of dig penetrations that were then used to calculate the torque and Net Thrust over the entire dig path. When combined with the friction analysis, the total required thrust force was calculated. An angular velocity of 30 RPM was decided on for the cutting head as angular velocity and torque had an inverse relationship and the gearbox being used has a maximum output speed of 30 RPM. By spinning the cutting head faster we significantly decrease the magnitude of the required thrust and torque which makes selecting components for and operating the system easier. The maximum value of thrust required is 21264 N. The maximum value of torque required is 2752 Nm. The results of these calculations over the entire dig path are seen in the graph below.

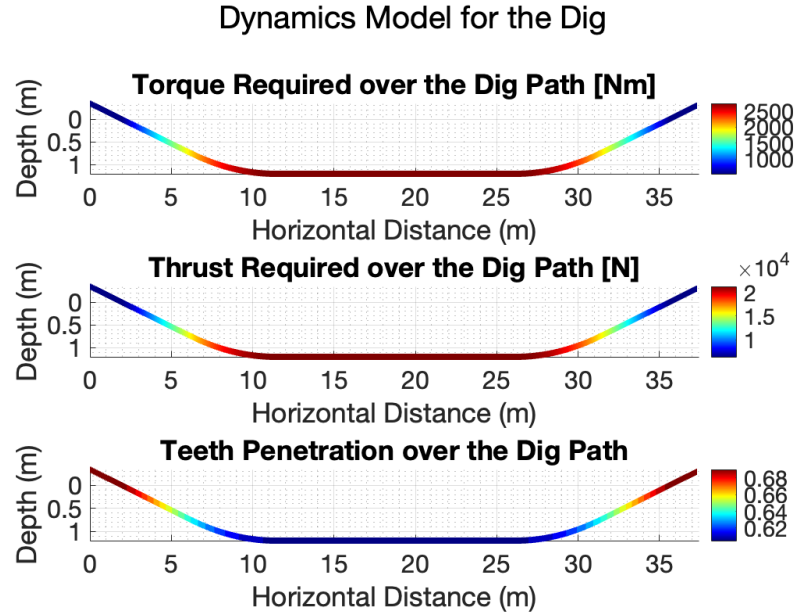


Fig. 7 System Dynamics Requirements

F. Dig Time Estimation

In addition to the requirements for the thrust and torque, the total dig time was also calculated. The active dig time was calculated by integrating equation 23 over the dig path. To find the time required to pull the TBM forward the same approach was used with the F_{Thrust} being substituted for the force required to overcome the friction forces on the back section. In addition to the time when the actuators are actively moving, the required time for the grippers to inflate and deflate is also incorporated into the calculation. The total dig time is 201 minutes. The breakdown of this time is seen in the table below.

Process	Time [min]
Active Dig Time	56
Pull Time	53
Gripper Inflation	92
Total Dig Time	201

Table 4 Dig Time By Sub-process

IV. Excavation System

A. System Overview

The excavation system actively digs the soil in front of the TBM through the use of a spinning cutting head. The cutting head excavates soil into the machine enabling forward movement. The system has 2 main parts, the cutting head and the drive system. The cutting head sits recessed in the front of the machine and is made up of a main plate and cutting teeth that are slotted into the plate. Driving the cutting head is a single gearbox and motor that serve to output the required 2750 Nm of torque. The multiple components of the excavation system are connected via a series of shafts, couplers and bearings that transfer the torque and thrust from the cutting head to the structure.

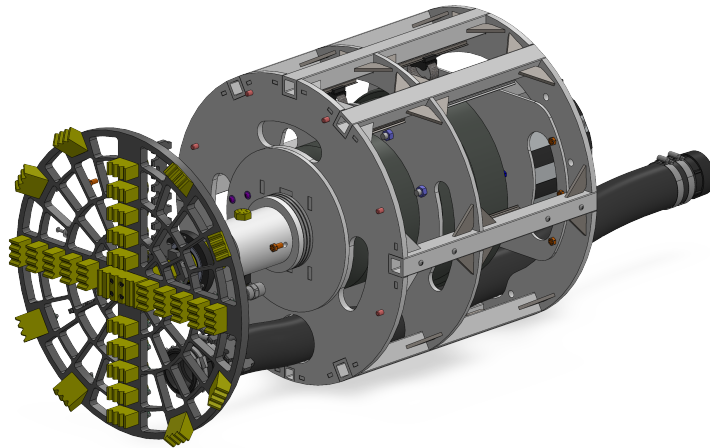


Fig. 8 Full Excavation System

B. Cutting Head

The cutting head was designed to maximize the opening ratio while maintaining structural integrity for the expected loading and abrasive digging process. The cutting head is made up of a main plate with teeth that get slotted in. This design was chosen due to its ability to easily manufacture and the ability to replace individual teeth in the case of wear. In addition, the main plate also has a hexagonal slot for the shaft. The teeth on the cutting head are arranged in a T pattern with each quadrant having slightly different radial with each tooth overlapping with 1/2 of the previous tooth.

This is key as it means that the entire front case of the cutting head is raked through on a single rotation. In addition, the cutting head is recessed into the shell of the machine. This reduces the torque experienced by 10-25% due to the outside of the plate not rubbing against soil. Due to this decision, a set of angled outer teeth are required to over-cut. With these outer teeth, the total excavated diameter is 63.5 cm. This gives the machine an over cut of 2.54 cm.

1. Cutting Head Plate

The cutting head plate is the base of the cutting head that serves to both secure all teeth in place while also transmitting all torques and thrust to the main hexagonal drive shaft. It has an opening ratio of 49.6%. In addition, all openings are less than 2.5" along the largest dimension to ensure that any particles that enter the soil chamber are able to be fully removed from the system without causing a clog. The plate is water-jet out of 0.75" thick AR 400 steel. AR400 was chosen due to its high hardness in combination with high yield strength enabling the plate to be thinner and withstand constant and soil abrasion.

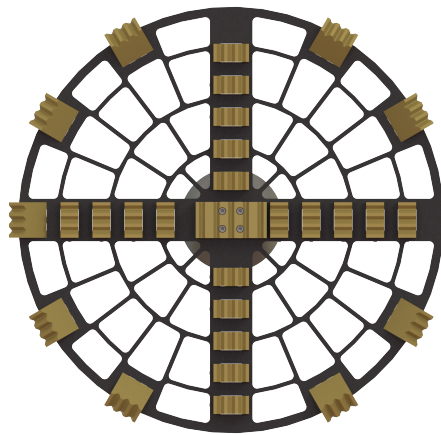


Fig. 9 Cutting Head Front View

2. Cutting Head Teeth

This year CU Hyperloop switched to a ripper style design for the cutting head teeth. Rippers were chosen due to the soil in Bastrop being silty clay with few if any rocks. In addition, due to the short span of the dig, it was decided that wear was not as much of an issue as thought last year. As mentioned above there are 2 types of teeth, inner and outer teeth. Both sets share a common design philosophy with the only difference being that the outer teeth are raked by 35 degrees.

Each tooth has a tooth penetration of 3.5 cm and has a rectangular cutting area of 2.54x5 cm. On the top face there are a total of 3 serrations. These serrations serve to grind up soil by increasing the area of the tooth that is contacting the soil. A tooth penetration of 3.5 cm was chosen as it allows for soil penetration without compromising the speed at which we can spin the cutting head.

Each tooth is secured by being slotted into the cutting tooth. The slot is 4 cm wide. The slot is slightly smaller so that the thrust for on each individual tooth is transferred to the cutting head. This interface is always in compression meaning that the load path for forces on the teeth transfer directly into the cutting head instead of going through an intermediary bolt or pin. To retain the tooth a bolt is used on the back side to pin the tooth. This bolt is under 0 nominal load and simply serves to keep the tooth in place when not actively mining.



(a) Inner Tooth



(b) Outer Tooth

C. Drive System

The cutting head is driven by a single electric motor and gearbox. As discussed in section III.E, the maximum torque experienced is 2752 Nm at 30 RPM. In an effort to save cost, the purchased drive system components from the 2023 competition are being reused. Both of these components meet the required specifications for this year and reusing them enabled the team to start manufacturing and integration sooner. The Drive system is center mounted in the machine with both the gearbox and the motor being flange mounted to the structure.

1. Motor

The ME1616 Brushless 20 KW motor is being used to drive the system. The motor has a maximum continuous torque of 78 Nm, and a maximum peak torque of 134 Nm, and can run at up to 6000 RPM. One nice feature of the Me1616 is that the available torque remains relatively constant with RPM. Additionally, the motor is small enough, with a diameter of 256 mm, that it can be mounted to the front face of the hexapod. Finally, the motor has 2 1/2" ports for water cooling.

For our expected maximum load, the motor will be running at a power of 9500 W while outputting a torque of 52 Nm at 1770 RPM. This gives us a torque overhead of 2.5x significantly reducing the likelihood of stall. In addition, at this power setting the motor has a thermal efficiency of 87%.

2. Gearbox

The gearbox being used is the gearkings THF-618-59. This cyclodial gearbox has a 59:1 reduction ratio, a maximum torque rating of 3079 Nm at 1770 RPM. In addition, due to it's cyclodial design, the gearbox also has a rated efficiency of 92%, reducing the overall power requirement for the system. To ensure that the gearbox ratings are never exceeded, the software system will artificially limit the motor torque so that the output from the gearbox never achieves 3080 Nm. The team decided to take the trade off of potentially having to mine slightly slower due to torque limitations in order to have a smaller physical package that was easier to route hosing around. The gearbox is flange mounted to a plate in the structure.

3. Load Path

The cutting head is the location of the primary forces for both propulsion and excavation. As such, the load path has been designed in a way to have the most streamlined reaction back into the soil. In pursuit of this goal, bearings were minimized with the only bearing in the system being a primary thrust bearing. A radial bearing is not required because the overhung load capacity of the gearbox is 3040 N. With the length of the shaft and the coupler, a load factor of 1.96 is calculated via the gearbox datasheet. As the cutting head is only 57 kg or 560 N, suspending the cutting head from the gearbox has a factor of safety of 2.7.

A thrust bearing is being used to transfer the load from the main shaft to the structure. Placed at the front of the gearbox structure this thrust bearing the SKF-51122 has a rated dynamics thrust of 83.2 KN. This gives a factor of safety of 3.91. This thrust bearing was selected due to it's internal diameter which was big enough to fit around a coupler for the gearbox shaft. Due to this, the bearing was able to be mounted by simply machining a flange into the gearbox to shaft coupler. The configuration of the thrust bearing is seen below.

Fig. 11 Thrust Bearing Location

To transfer the thrust from the cutting head to the main hex shaft, a restraint is used. This restraint is welded on the main hex shaft and sits right behind the cutting head plate. When the cutting head plate is compressed the force is transferred into the restraint which conversely transfers it to the main hexagonal shaft.

To transfer the force from the hex shaft into the coupler a 3/4" bolt is used. This bolt serves to both secure the shaft to the coupler while also transferring the load. With a 60 KN load, the maximum the hexapod can output, the bolt has a factor of safety of 4.43. the full calculation is seen below.

Bolt

$$F_{max} = 60 \text{ kN}$$

$$A_t = 0.33\pi \text{ in}^2 = 2.1548 \cdot 10^{-4} \text{ m}^2$$

$$d = 3/4 \text{ in}$$

$$\text{double shear } N=2$$

$$\sigma_y = 150 \text{ ksi} = 1030 \text{ MPa}$$

$$\text{shear factor} = 0.6$$

Solution:

$$\tau_{max} = \frac{F_{max}}{A_t N} = 139,22 \text{ MPa}$$

$$FS = \frac{\sigma_y}{\tau_{max}} = 4.43$$

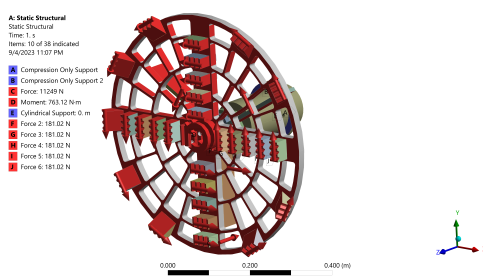
Sketch:

Fig. 12 Hand Calculation for stress in the coupler bolt

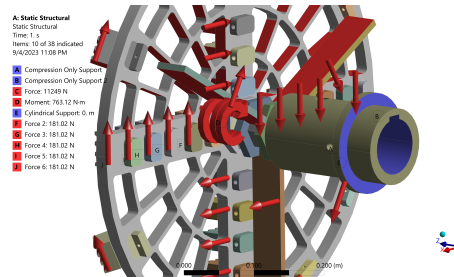
Overall the 2 load paths are as follows. For thrust a force applied on a cutting head tooth goes into the cutting head plate via the flange on the cutting teeth, then transfers into the hex shaft via the restraint, then transfers into the coupler via the main bolt, then transfers into the structure via the thrust bearing before finally being reacted by the hexapod and grippers in the back of the machine. For torque, a tangential force applied to a cutting tooth transfers into the cutting head plate via the slot, then transfers into the hex shaft via the hexagonal slot in the cutting head, which then transfers into the gearbox coupler via a female shaft insert. Finally, torque is transferred into the gearbox which is transferred into the structure via the 8 flange mounting holes and ultimately transferred into the soil at the back grippers.

D. Excavation Analysis

Substantial structural analysis was performed on the excavation system to ensure that all components would survive. For the setup of the system, the back of the drive shaft was held fixed while individual forces were applied to each of the cutting head and cutting head plate base on the methods discussed in section III.C.3. Images of the FEA setup is seen below.

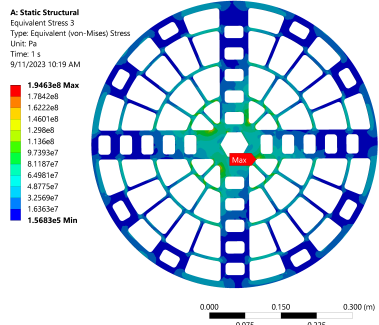


(a) FEA Setup for Cutting Head Simulation, Front View

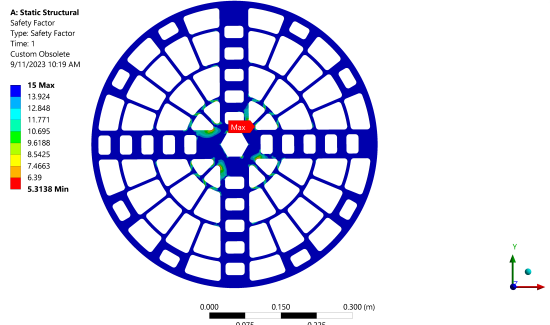


(b) FEA Setup for Cutting Head Simulation, Back View

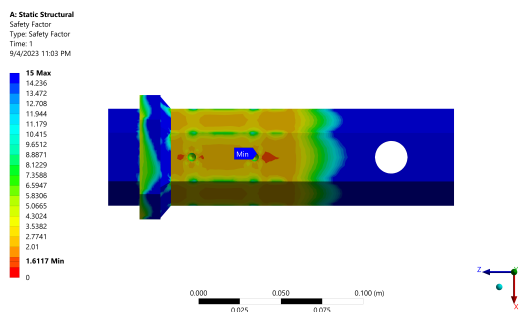
From the analysis the following results were found. Images of the full factor of safety distributions for critical parts are seen in the images below. The overall system has a minimum factor of safety of 1.61 which occurs at individual nodes on the drive shaft. The main plate has a minimum factor of safety of 5.31 and the minimum factor of safety in the coupler is 3.13.



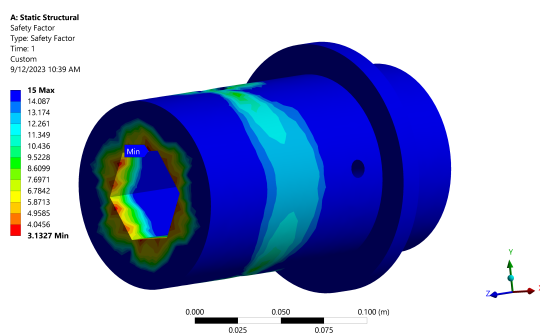
(a) FEA Stress in Cutting Head Plate



(b) FEA Factor of Safety in Cutting Head Plate



(a) FEA Factor of Safety in Cutting Head Drive Shaft



(b) FEA Factor of Safety in Drive Shaft Coupler

V. Propulsion System

The propulsion system governs movement of the TBM through three interconnected systems spaced throughout the structure. These systems include the hexapod (or Stewart Platform) and the front and rear grippers. The hexapod has 6 actuators, each with an 8-inch stroke length, and is placed in the middle of the TBM connecting the front and back sections. It provides all of the thrust and steering control for the TBM. The front and rear grippers inflate to provide frictional forces as appropriate. They have three inner tubes each, which are all individually covered by a chain “webbing” and a fabric shroud, to transfer reaction forces into the steel structure and to provide abrasion resistance, respectively. The grippers expand into the soil around the TBM, holding a section in place.

The propulsion process begins with the rear grippers activated to contact the tunnel wall. The friction between the gripper and the tunnel wall will hold the back of the TBM in place while the hexapod pushes the cutting head along the desired path to dig the tunnel. After the hexapod propels our system forward, the rear grippers retract and the front grippers activate to contact the tunnel wall. The front grippers will hold the front of the TBM in place while the hexapod pulls the rest of our system forward, back to its original orientation. Finally, the front grippers will retract and the process will begin all over again and the propulsion system will run in this cycle until we dig a 100ft tunnel at speeds \geq Mach Snail.

A. New Features

Compared to our machine last year, there are many improvements made to the propulsion system. Below are some of the highlights:

- 3 inner tubes per gripper instead of 2.
- Gripper shroud has been broken up into 2 materials: a chain to transfer reaction forces, and Kevlar to protect inner tubes.
- Kevlar shroud is not fastened to the structure, and instead wraps completely around the inner tube, held together by Velcro for easy tube replacement and more complete protection.

- Hexapod actuator orientation is no longer 3-way symmetric – this allows for easier routing of the soil hose through the bottom of the machine.

B. Grippers

Inflatable grippers are being used to lock the machine into the soil. Inflatable grippers have three main advantages over mechanically actuated grippers. The first is soil ingress; unlike most mechanical designs, an inflatable gripper does not allow soil into the machine during activation. The second is the load distribution. Inflatable grippers push normal to the soil, 360 degrees around the TBM. This reduces the shear force on the soil, reducing the possibility of collapse. Another advantage is the packaging. Unlike mechanical grippers, inflatable grippers only take up the outer 6 cm radially of the TBM. This leaves room inside to package components, reducing the overall length of the TBM.

The grippers are made of three bicycle inner tubes, each of which is completely wrapped in a Kevlar 49 sleeve and secured in the sleeve with Velcro. They live in a recessed area in the machine and are enclosed by a chain, which is welded to the structure on one side and fastened with a quick link on the other.

To find the necessary inflation pressures of grippers, we assume a worst-case scenario: only one tube is working and it must react against the full force of the hexapod, ignoring frictional forces that would aid grippers (f_s in Figure ?? below).

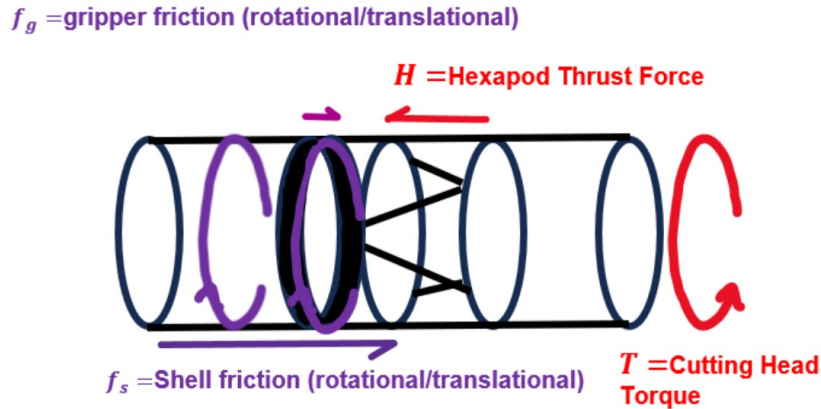


Fig. 16 Overall FBD of Gripper and Hexapod System

This FBD reveals the relationship in the following.

$$P_{fg} = \frac{P_g A_b \mu_s}{A_{fg} \mu_g} = \frac{(1.9)(4606)(0.55)}{(249)(0.5)} = 38.66 \text{ psi.} \quad (24)$$

where P_{fg} is the pressure required in the front grippers, P_g is the geostatic pressure at max depth, A_b is the area of the back section, μ_s is the coefficient of friction between soil and the steel shells, A_{fg} is the area of the front gripper contacting soil, and μ_g is the coefficient of friction between grippers and soil. A similar analysis was done to find the inflation pressure of the rear grippers, $P_{rg} = 34.2 \text{ psi}$. This results in a pressure vessel with stored energy on the TBM of 7.2 kilojoules in the form of pressure energy.

C. Chains

Our setup includes a chain rated for 9341 N and quick links rated for 6227 N. Given the lateral forces acting on the chain, estimated to be around 2620 N, the chain should provide a safety factor of 3.5 under dynamic loading conditions. In addition to that, given the same force on the quick links at max load, the quick links should also provide an adequate safety factor of 2.4. These safety ratings are compounded by the fact that there is already a large factor of safety on the capacity ratings of the chains and quick links.

To determine the optimal chain mounting angle, we analyzed the two loads applied on the chains: the axial load of 48 kN and a torque of 2750 Nm. Because chains only resist loads along their axis, we calculate the equivalent axial load applied on the edge of the machine at a radius of 30.5 cm. We obtain an effective load of 61 kN applied at an angle of 8 degrees; thus, the chain is mounted into plates at an angle of 8 degrees from the digging axis.

D. Fabric and Velcro

The Kevlar fabric, covering the inner tube, is selected for its high tensile strength and high abrasion resistance, which is needed as the Kevlar will be subject to many forces from the soil. Using six sheets of Kevlar, each measuring 0.4064 m by 1.905 m, allows us to cover all 6 inner tubes. Given the operational stress, the fabric is expected to handle a maximum of 32.91 MPa, which is well within Kevlar's rated tensile strength of 3600 MPa.

The Velcro we are using to secure the Kevlar material around the inner tube needs to cover around 1.755 m. With a 0.1524 m Velcro strip, the total contact area is 0.2675 m². Given the Velcro's shear strength of 23 psi, this configuration allows it to withstand a maximum force of

$$F = \sigma \cdot A = 158.58 \text{ kPa} \times 0.267 \text{ m}^2 = 42.42 \text{ kN.}$$

The maximum expected operational force of 17.75 kN results in a Factor of Safety (FOS) of 2.4, indicating that the Velcro attachment provides adequate strength under expected loading conditions.

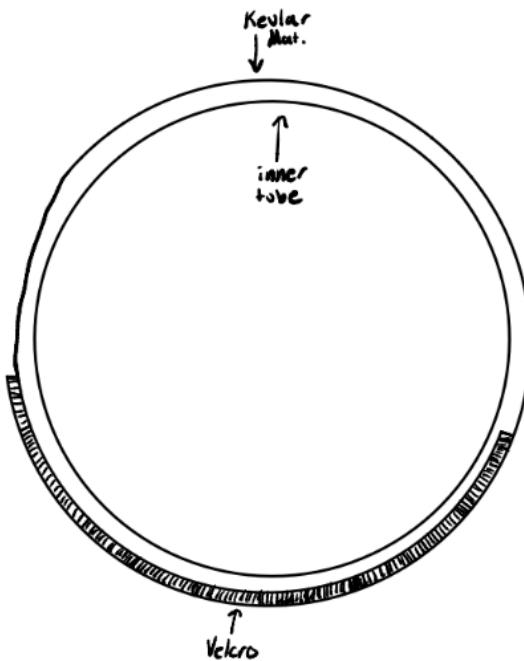


Fig. 17 Kevlar Material Fixed With Velcro

E. Fixtures to Structure

The chains will be welded to the plates that house the inner tubes. The weldment analysis is based on a 2620 N applied force and on A572 grade 50 steel with a yield strength of 345 MPa. We also apply the force at an angle of 60 degrees from the plate. After welding three sides of the chain, we obtain a safety factor of 190 for a perfect weld. This allows us to have some leeway in the manufacturing process while maintaining the integrity of the weld.

F. Plate Tearout

The quick link tearout analysis is based on a theoretical applied force of 2620 N. Tearout shear stress (τ_y) is calculated using:

$$\tau_y = \frac{F}{2et} \rightarrow t = \frac{F\sqrt{3}}{2e\sigma_y}$$

Where:

- F is the applied load (2620 N)
- e is the edge distance from the hole to the material boundary
- σ_y is the yield strength of A572 Grade 50 steel (345 MPa)

With this force and material properties, the minimum required thickness to prevent tearout is calculated as 1.03 mm. Since we selected the actual thickness to be 5.08 mm, there is a safety factor of roughly 5, which not only prevents tearout failure but also accounts for manufacturing tolerances and unexpected load variations.

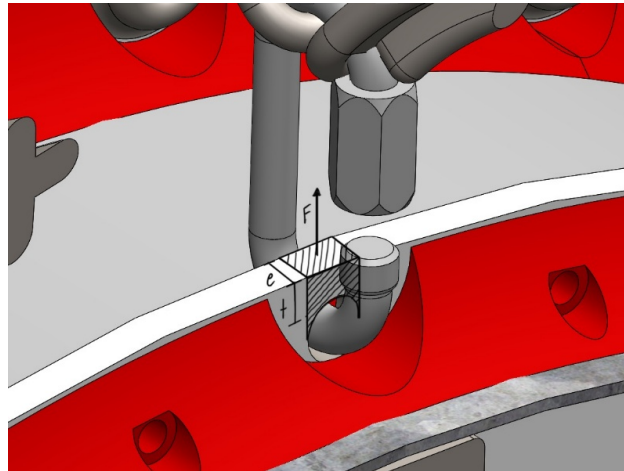


Fig. 18 Plate tearout diagram

G. Pneumatics

Each gripper is fully redundant, which requires each gripper to have its own pneumatic valve and hose. Figure (4) shows the pneumatic circuit controlling airflow to grippers. The compressor, regulators, and valves sit on the surface, while the pressure transducers and air pistons (inner tubes) sit onboard the machine.

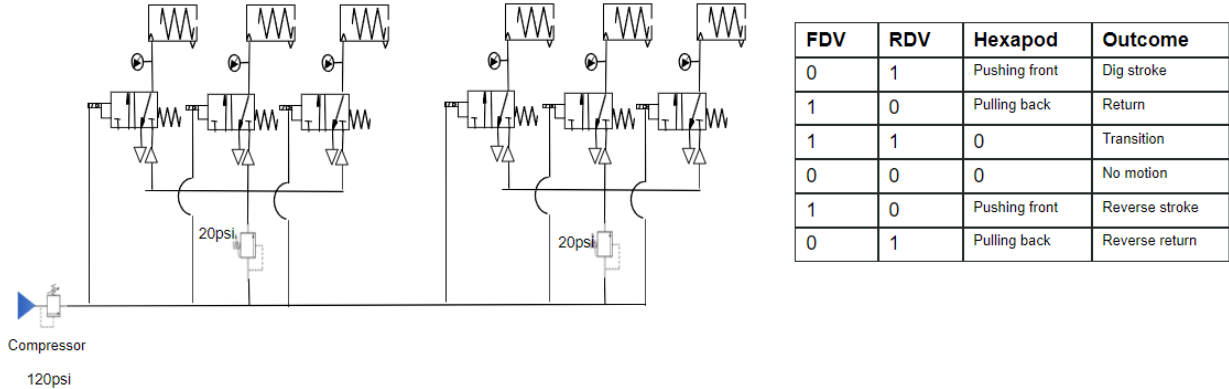


Fig. 19 Pneumatic Circuit Controller

H. Pneumatic Circuit

To calculate expected soil deformation due to grippers expanding, we look to the stress-strain relationship, solved for deformation in the following equation.

$$\Delta L = \sigma L_0 E \quad (25)$$

where σ is the stress experienced by the soil (gripper inflation pressure), E is Young's Modulus, L_0 is the initial length of soil to be affected, and ΔL is how much L_0 changes after deformation. Young's Modulus for soil can be approximated from stress-strain curves given in the Geotechnical Report provided by TBC and was found to be 16,650 psi. Assuming that the affected soil length is one tunnel diameter, or 24 in., and using 40 psi for gripper pressure, we get an expected soil deformation of 0.0048 ft, or 0.14 cm.

I. Hexapod

Geometry->expected loads + thrust/torque output:

The hexapod is made of 6 electric 10kN actuators connecting two plates by ball joints. Each actuator is able to be individually controlled by the machine's software. When the desired digging path is determined, each actuator extends to a maximum of eight inches, with a maximum force of 10kN. This motion produces an angle within the hexapod that determines the nominal path of the TBM. This output is recorded into the built-in Hall effect sensors, which provide insight into extension length and angles the actuators create. Having six of these actuators allows for full pitch and yaw to be leveraged by the control system. This radial motion allows for different angles of digging to occur at a given time. This movement can produce a turning radius of 20 m undergoing a maximum stress of 7GPa from the surrounding soil pressure.

This year, actuators are not spaced with 3-way symmetry on the back plate as is conventional. The front plate has ball joint pairs spaced at 15deg with 3-way symmetry, while the back plate has 2 pairs spaced at 18deg, and the third (bottom) pair spaced at 22.5deg. This decision was made to accommodate the soil hose running straight along the bottom of the hexapod, avoiding a hose with a 45deg bend and a simultaneous extension as the hexapod extends. While this change is subtle, it changes the inverse kinematics solver. (This is, however, a software issue. As such, they will fix it in software.)

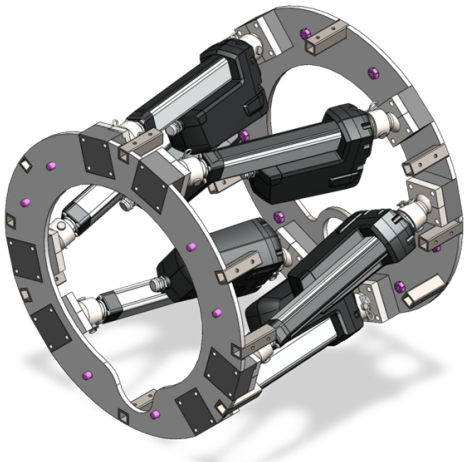


Fig. 20 Hexapod

This geometry results in 2 classes of actuators: 14.1deg from the dig axis, and 11.8deg from the dig axis. To find the net forwards thrust, we take into account the angle of the actuators, and the torque that must be transferred through the hexapod, and arrive at the figure below.

J. Hexapod Angles FBD

Half of the actuators will see the torque reaction force going in the direction pictured, and the other half will see the torque reaction force facing opposite as pictured. This analysis assumes that the actuators seeing extra force will be a limiting factor. Using $F_{actuators} = 10\text{kN}$, $F_\tau = 1.93\text{kN}$, we get 2.0 kN of thrust for the 14.1deg actuators and 0.55kN for the 11.8deg actuators. Because both numbers are greater than 0, there should be no issues transferring torque through the hexapod.

K. Actuator and Ball/Socket loads

The hexapod was designed to use ball and socket joints at the ends of each actuator. To achieve the full range of motion from the hexapod, each joint in the system had to be capable of rotating 360 degrees. Initially, universal joints were planned to be used. However, through prototyping we found that the pins within the joints were not holding up to the stresses that the actuators were imparting on them. Ball and socket joints evenly distribute the forces through them across the hemispherical surface area, while also providing the required range of motion.

Six degrees of freedom are typical of a machine like this, since the ball and socket joints are oriented at each end of each actuator. However, side movement is constrained due to soil pressure, so the ball and socket joints allow the hexapod to achieve three degrees of freedom.

The ball and socket joints which the actuators are mounted onto were manufactured from 1018 Steel and machined using a CNC lathe out of 2" stock, which allows for a 10-degree range of motion to achieve the desired trajectory of the TBM.

The ball and socket joints were analyzed using FEA. For the ball joints 2 FEA simulations were performed, one for compression and one for tension. For the compression simulation a compression-only support was placed on the lower half of the ball, imitating the bottom half of the socket. Then a 10 kN force was applied to the holes for the bolts. It was assumed that all of the force from the actuators would be transferred through the bolts. Running this simulation resulted in a 6.21 FS for compression. The images of this analysis are seen below.

A similar setup was used for the ball joints in tension with the only differences being that the compression-only support was placed on the top half of the ball and the direction of the applied force was reversed. This analysis resulted in a 3.38 Factor of safety. The setup and results of this simulation are seen below.

The socket caps were only simulated in tension as when in compression this part takes no load. The load was applied on the dome cutout as that is where the ball joint will impact. The bolt holes were set as fixed supports as it is assumed

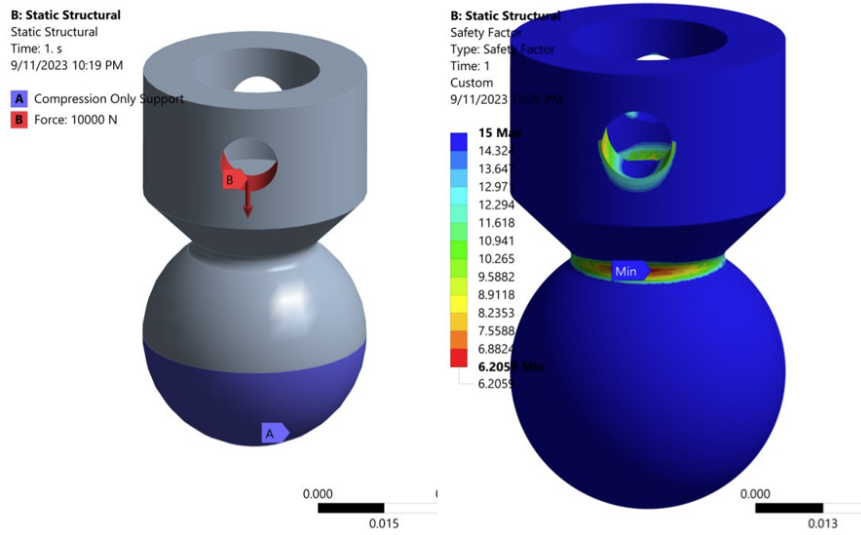


Fig. 21 FEA Safety Factor plot of Hexapod ball joints in compression

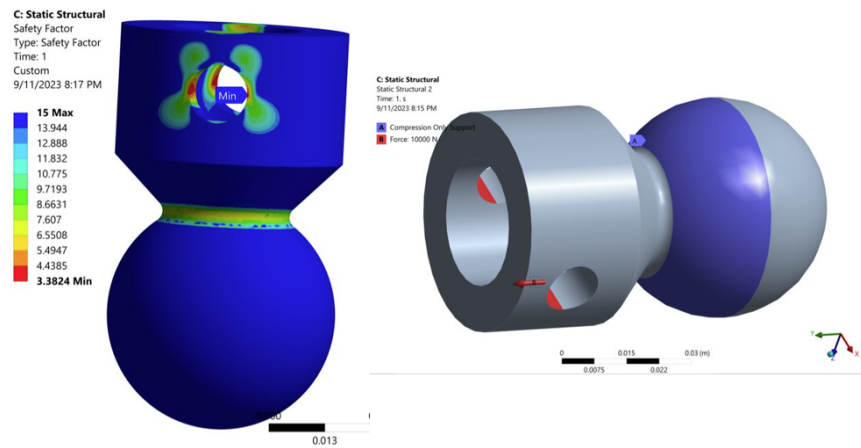


Fig. 22 FEA Safety Factor plot of Hexapod ball joints in tension

that the bolts will not move during motion. The result of this analysis was a factor of safety of 4.02. This occurred on the inner side of the bolt holes, which makes sense due to the force being spread out over a smaller area. Images of the setup and result are seen below.

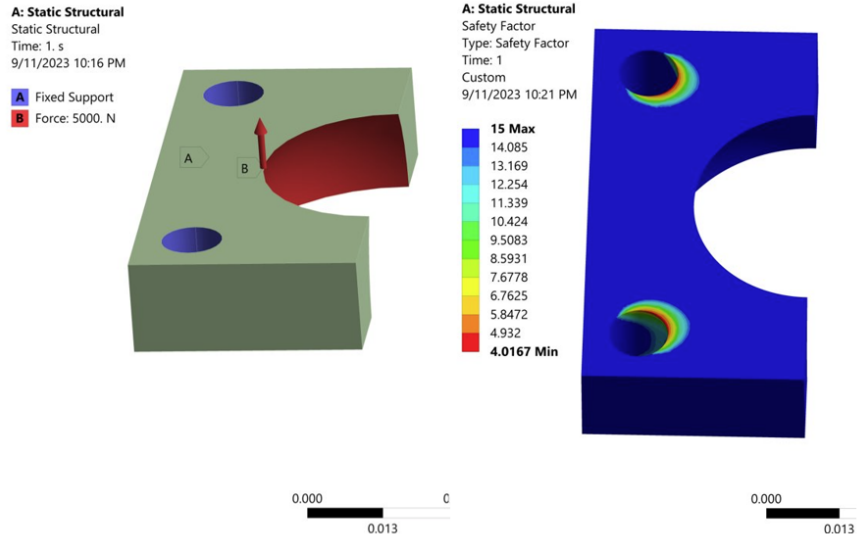


Fig. 23 FEA Safety Factor plot of Hexapod socket caps in tension

VI. Cooling System

A. System Overview

To ensure that none of the components are going to overheat a cooling system needs to be implemented. Our cooling system will consist of multiple heat exchangers attached to the components that are expected to overheat. The components that are in focus in maintaining their operating temperatures are motor, hexapod actuators, motor controller, hexapod box, tunnel support box, and the tunnel support printing surface. With a 3D printer in the back of the machine extruding PLA at 160 C, the delta T is going to be too low to cool down the coolant. Taking that into account we decided to have our main heat exchanger to be on the surface. One of the main changes we have this year to the cooling system is that we added a reservoir on the surface that will be attached to a water chiller. The water chiller is a refrigeration cycle that takes in the water from the reservoir, cools it down through the components of a refrigeration cycle, and then pumps it back to the reservoir. In case, the water chiller did not have enough power to cool down the water in time we will resort to adding bags of ice into the reservoir.

B. P&ID

Fig. ?? shows the P&ID of the cooling system. The system starts at the cold reservoir, it's then split into two lines. The first line goes to the manifolds inside the machine that directs the water to the heat exchanger attached to their respective components. The second line goes to our printing surface heat exchanger. Both lines go back to the cold reservoir that is attached to a water chiller that keeps cooling the hot water that comes back from the machine. Due to the high-pressure drop in the tunnel support printing surface heat exchanger, another pump has been attached to the hotline to act as a pressure booster.

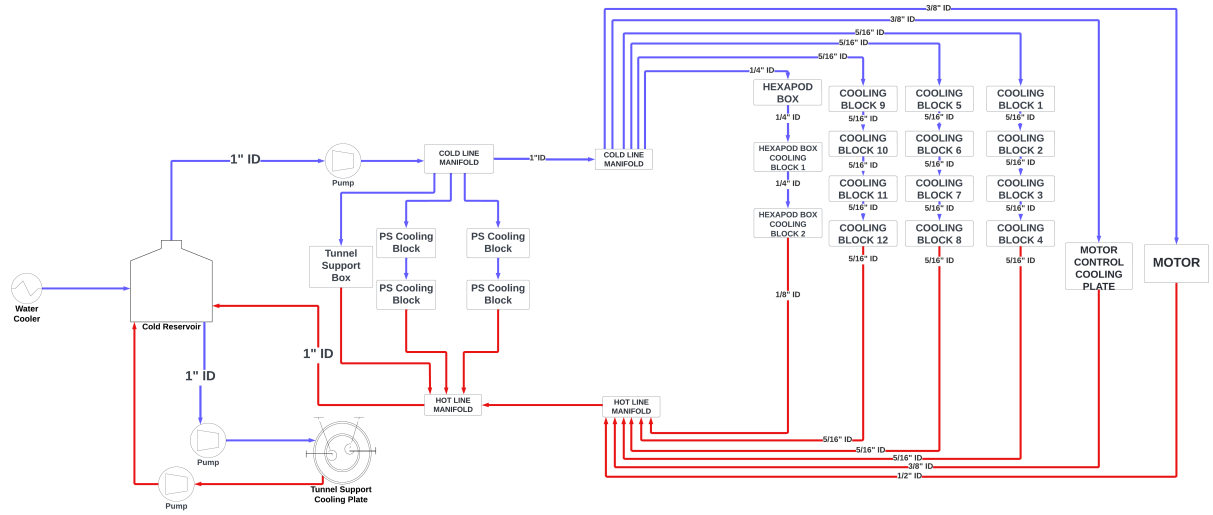


Fig. 24 Cooling System P&ID

1. Cooling Plate and Cooling Blocks

The actuators and power supplies are going to be using aluminum cooling blocks that will be contacting them. On the other hand, the motor controller will have a cooling plate attached to it also made out of aluminum. Water of 7°C will be flowing through them cooling down the cooling blocks and absorbing the heat produced from these components.



(a) Motor Controller Cooling Plate



(b) Actuator and Power Supply Cooling Block

2. Motor Cooling System

The motor has its own cooling system integrated into it, however, for the cooling system to activate it we need to supply it with the appropriate flow.



Fig. 26 ME 1616 Motor

3. PCB Chips Cooling

This year we have two PCB boards that are going to be cooled down. The hexapod board and the tunnel support board. The hexapod board will have 6 H-bridge chips that will overheat if it was not cooled. The tunnel support board is still under design however cooling down the chips will follow the same procedure.



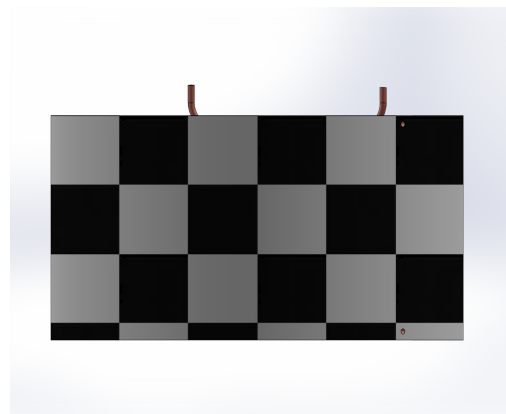
Fig. 27 PCB Cooling Block

4. Cooling Shell

To cool down the printed segments after being extruded from the 3D Printer nozzles we ave designed our own custom heat exchanger. Our cooling shell will be made out of a copper helical tube submerged in aluminum. The cooling shell will be talk about more below.



(a) Cooling Shell without Aluminum Cast



(b) Cooling Shell with Aluminum Cast

5. Heat Exchanger (Water Chiller)

A 1 HP water chiller would be attached to the reservoir. It would transfer the water through a refrigeration cycle that would cool down the water to a desired temperature.



Fig. 29 1 HP Water Chiller

6. Pumps

The system would have 3 pumps, 1 to feed the main cooling system and 2 to support the pressure drops in the tunnel support printing surface heat exchanger. The main cooling system pump would have a flow rate of 5 gpm with 20 psi. While the tunnel support printing surface heat exchanger pumps would have a flow rate of 2 gpm at 50 psi.

C. Analysis

Having a high delta T optimizes the performance of cooling systems. A temperature of 7 C has been chosen to provide the optimization of the cooling system. The method of figuring out the heat being produced is rather simple.

$$Q = (1 - \eta) * P \quad (26)$$

Below is a table showing the operating temperatures and watts of heat being produced by each component in the main cooling system. Knowing that these components are not going to be operating at their maximum capacity constantly, the numbers below are what they produce during their peak performance; the cooling system has been designed accordingly.

Name of component	Max Operating Temperature [C]	Heat being produced [W]
Hexapod Actuator	60	192 total of 6
Motor	100	1200
Hexapod H-Bridge Chip	150	18 total of 6
Power Supply	60	660 total of 2
Motor Controller	70	N/A
Tunnel Support Board	N/A	N/A

Table 5 Cooling Analysis

1. Cooling Shell Heat Analysis

The tunnel support will have two nozzles producing 2481.1 W each we have reached to that conclusion by the calculations below:

We have split the analysis into three phases, melting the PLA and waiting for the PLA to solidify, and decreasing the temperature from 160 C to 150 C

$$Q_{Fusion} = m_{dot} * L_f \quad (27)$$

$$Q_{160-25} = m_{dot} * C_p * \delta T \quad (28)$$

$$Q_{160-150} = m_{dot} * C_p * \delta T \quad (29)$$

In Eq.27, the m_{dot} is equal to $0.01405 \frac{kg}{s}$ and the L_f is equal to $93600 \frac{J}{kg}$ which makes Q_{Fusion} equal to $1315.09 W$. In Eq.28 and Eq.29 both m_{dot} and C_p are equal to $0.01405 \frac{kg}{s}$ and $1800 \frac{J}{Kg*K}$ respect respectively. However, for Eq. 28 δT is equal to $135^{\circ}C$ and for Eq. 29 δT is equal to $10^{\circ}C$ making the heat produced $3414.19 W$ and $252.9 W$ respectively. Concluding the total heat produced to be $4982.19 W$.

2. Cooling Shell Geometry Analysis

To make sure that we do not have any tubings intercepting the route of the printing nozzles we designed a heat exchanger made out of two copper coils that have an OD of $\frac{3}{8}''$. These two copper helixes are attached by a U-fitting joining them to become one helix. The helix is then submerged in casting Aluminium, Al 356 to be exact. Submerging the helix in the aluminum provides a smooth surface compared to the helix that would optimize heat transfer.

$$Length = N * \sqrt{C^2 + p^2} \quad (30)$$

In Eq. 30 C, circumference, is equal to 72.75 in, p, pitch, is equal to 0.6 in, and the N, number of revolutions, is equal to 19.111 making the length of the helix equal to 1390.37 in or 115.86 feet. We have designed this heat exchanger with geometric restrictions put by our structures. The restrictions were: $12''$ in height and $2''$ of pure aluminum to enable the attachment of the cooling shell to the machine.

3. Cooling Shell Fluid Analysis

The analysis of the cooling performance of the heat exchanger is below:

$$Q_{Cooling} = h * A_s * \delta T \quad (31)$$

Eq.31 uses conductive cooling calculations to figure out how much heat the water running through the helix can absorb. The heat transfer coefficient was found using the flow rate of the water, $7108.239 \frac{W}{m^2*k}$. While the wetted surface area was found using Π multiplied by the ID and length which results in $0.877 m^2$. δT is the temperature difference between the temperature of water and the temperature of the copper helix. Assuming that the copper helix will be around 159° , the water will be able to cool around $947556.69 W$. The reason why the number of the absorbed heat is high is because the calculation is taking into consideration the 115 feet of copper piping.

Another concern the design needs to accommodate is the pressure loss in the helix. Below is a graph showing the pressure loss and temperature change in the water with respect to the flow.

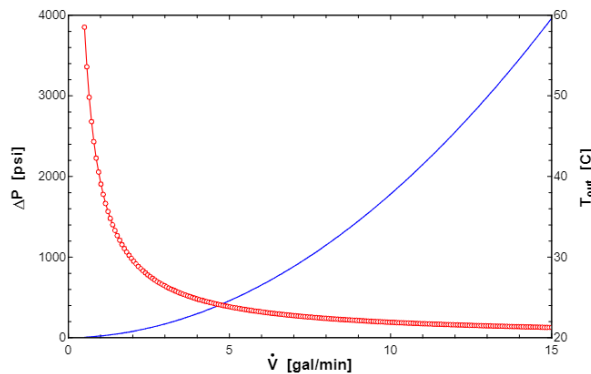


Fig. 30 Water temperature Change/ Pressure loss in helix with respect to flow rate

From Fig. we can find that a flow rate with 2 gpm is the most optimal flow rate for our system. The pressure loss at 2 gpm is around 80 psi and the temperature change is around $9^{\circ}C$.

4. Steady Heat Temperature Analysis

To find the final temperatures of the components producing heat we followed Eq.32. Below is a table of the components before and after the cooling system.

$$Q = \frac{k * A_s * \delta T}{d} \quad (32)$$

Component	Final Temperature Before Cooling System [C]	Final Temperature After Cooling System [C]
Motor	100	Under Testing
Hexapod Actuators	60	Under Testing
H-Bridge Chips	150	Under Testing
Printing Surface	160	Under Testing
Tunnel Support PCB Chips	N/A	N/A
Motor Controller	70	Under Testing
Power Supply	70	7.87

Table 6 Steady Heat Final Temperatures Before and After Cooling System

VII. Soil Removal

A. System Overview

The excavated soil will be transferred using an industrial vacuum at the surface. The vacuum will be connected to the front end of the machine using a 100 ft 4" hose that decreases to the 3" inside the machine. The vacuum hose will end at the soil chamber a section of the machine that collects the excavated soil that helps us in transferring it to the surface. Another main component of the soil removal system is the soil agitators. The agitator will consist of 3 set bars connected to the gearbox that will rotate these bars with the cutting head, offering to mix the mixture and agitate the soil. They will be used to mix the GCS mixture with the soil in the soil chamber.

B. Vacuum Chamber

Our soil transport system is going to be the Terravac Xpose 800 construction-grade vacuum excavator. This vacuum excavator is rated for both dry and wet transport. A vacuum hose will be connected to the vacuum excavator and run through length of our tbm and our designated boring length. The Xpose 800 is rated for 4.5 gpm at 4000 psi however we determined through testing that a 35 gpm was possible. Tests were conducted on unconditioned soil meaning that during the actual dig the particle sizes will be smaller after passing through the cutting head, agitator, and being mixed with our anti clay polymer. The test also determined the choice of a 4" diameter vacuum hose, this decision helps with both minimizing the pressure drop and assisting in mitigating clogs. Considering that the vacuum excavator can only house 800 gallons a designated soil dumping area on site will be used to empty the machine accordingly.



Fig. 31 TerraVac Xpose 800

C. Clog Detection

Detecting clogs is one of the critical parts of the success of the soil removal system. The way we are mitigating that is by attaching pressure transducers on the soil removal hose. These sensors are going to be connected to the GUI that will help us identify any abnormal fluctuations in the soil removal hose.



Fig. 32 PTNN4G100PV05M12

The PTNN4G100PV05M12 from IMI Norgen is a pressure transducer that is able to detect pressure from 0 psi - 100 psi. Considering that our suction pressure would be from 5 psi - 10 psi the PTNN4G100PV05M12 fits in our needs of detecting clogs.

D. Material Path

The system starts with a 4" hose that is connected from the Xpose 800 to the back of the machine. It is then connected to a camlock connection that connects the umbilical hose to the hose inside of the machine. The camlock connector provides the ability to fully assemble the machine before shipping it off. Furthermore, the camlock changes the size of the hose from 4" to 3". Previous analysis showed that a 3" diameter hose that is less than 5 meters long is not significantly effective against the pressure drop. A 3" diameter helps with the spacing of the inside of the machine. A key component in the machine path is the PVC extension fitting that will be talked about more later in this document. The soil path also has two removal disconnects points. These disconnect points are threaded joints that help facilitate the integration of the machine. The soil path then ends at the soil chamber where it will be mixed using the agitator.

1. Agitators

Made out of 3 steel bars attached to the cutting head shaft the agitator will help in directing the excavated soil to the chamber and be able to mix the GCS mixture with the soil. The agitators are normal mining direction so that the cutting head can rotate in both directions with the agitators behaving the same.

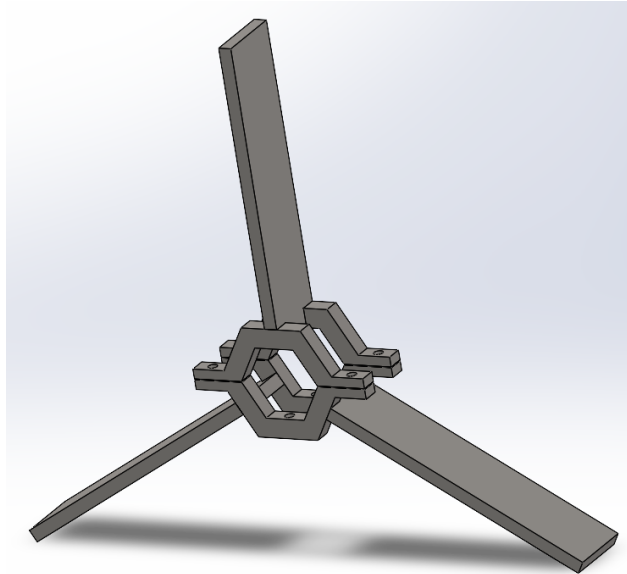


Fig. 33 Soil Agitators

2. PVC Extension Fitting

To avoid having a slack of 6" of 3" ID hose we have designed an extension fitting that enables the soil removal hose to expand and contract during our pushes. The fitting is made out of PVC pipes that slide inside each other and is mounted to the back of the hexapod plate using a flange mount.

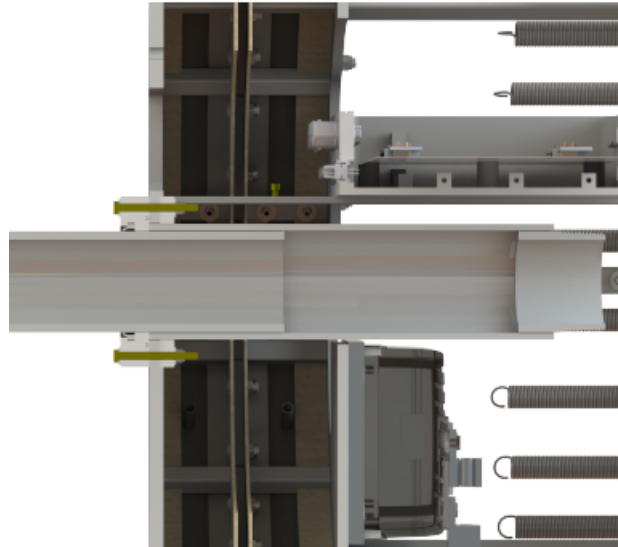


Fig. 34 Extension Fitting

Previous testing has proven the functionality and durability of the extension fitting. The test consisted of moving the extension fitting by hand 1000 times while connected to the shop's vacuum providing 5-10 psi of suction. The 5-10 psi is similar to the Xterra 800 will provide. The PVC pipe is naturally smooth enough to keep the force that starts moving the inner tube minimal even with after being covered in dirt and extensive wear. The tests have also shown that the pipe would be able to hold a vacuum as a hand was put to cover the end. Moreover, the extension fitting held suction.

E. Soil Lab

Following the Geotechnical Report submitted by TBC, Boring log B-1 was the closest soil composition where the dig is going to happen. Following the boring log we find the soil is made out of 8.6% Sand, 45.7% Silt, 45.7% Clay, and 26% - 35% water content. The increase of water content is to test the soil in the worst case scenario. According to tests conducted last year we have concluded that the best ratio to the soil and GCS mixture is 15% water 5% additive. It took us 53 seconds to remove 3.6 kg of soil making the soil significantly less viscous after adding the mixture. However, we will conduct more tests this year to solidify the ratio chosen.

Boring Log No. B-1

	Project: Bastrop Data Report Bastrop County, Texas	Sampling Date: 4/20/21																																																																				
	Location: See Boring Location Plan																																																																					
	Coordinates: N30°9'10.77" W97°24'12.59" Backfill: Cuttings/bentonite																																																																					
	<table border="1"> <thead> <tr> <th>Soil Description</th> <th>Depth (ft)</th> <th>SN</th> <th>WC</th> <th>PL</th> <th>LL</th> <th>PI</th> <th>PP</th> <th>N</th> <th>-200</th> <th>DD</th> <th>Uc</th> </tr> </thead> <tbody> <tr> <td>FAT CLAY (CH), firm, brown</td> <td>SS</td> <td>21</td> <td></td> <td></td> <td></td> <td></td> <td></td> <td>5</td> <td></td> <td></td> <td></td> </tr> <tr> <td>FAT CLAY (CH), stiff, dark brown</td> <td>SS</td> <td>26</td> <td>22</td> <td>59</td> <td>37</td> <td></td> <td></td> <td>10</td> <td>91</td> <td></td> <td></td> </tr> <tr> <td></td> <td>SS</td> <td>19</td> <td></td> <td></td> <td></td> <td></td> <td></td> <td>22</td> <td></td> <td></td> <td></td> </tr> <tr> <td></td> <td>5</td> <td></td> </tr> </tbody> </table>										Soil Description	Depth (ft)	SN	WC	PL	LL	PI	PP	N	-200	DD	Uc	FAT CLAY (CH), firm, brown	SS	21						5				FAT CLAY (CH), stiff, dark brown	SS	26	22	59	37			10	91				SS	19						22					5										
Soil Description	Depth (ft)	SN	WC	PL	LL	PI	PP	N	-200	DD	Uc																																																											
FAT CLAY (CH), firm, brown	SS	21						5																																																														
FAT CLAY (CH), stiff, dark brown	SS	26	22	59	37			10	91																																																													
	SS	19						22																																																														
	5																																																																					

Fig. 35 Boring log provided by The Boring Company

Boring	Depth	D100	D60	D30	D10	%Gravel	%Sand	%Silt	%Clay
● B-1	2.0	4.75				0.0	8.6	91.4	
☒ B-1	18.0	4.75				0.0	18.0	82.0	
▲ B-1	23.0	75	1.064	0.261	0.088	5.8	87.2	7.0	
★ B-1	33.0	75	3.883	0.338		37.4	44.7	17.9	

Fig. 36 Boring log provided by The Boring Company

F. Soil Settlement

Firstly its important to note that as we are not using an EPB machine, we don't need to worry about heave calculations. We are concerned with settlement which follows well to a gaussian curve. Because of this we know that right over the tunnel's center point the maximum settlement (S_{max}) will occur. However, this is still an open field of research, and a worst case scenario can be determined by taking the maximum depth lost from excavation. Between the overcut of the TBM, tunnel lining printed on the interior of the machine, and expected squishification of the tunnel lining we expect to see an S_{max} of no more than 10cm.

VIII. Ground Condition System

A. System Overview

Considering our soil removal system will be a slurry machine type, we have refrained from using a foamy GCS system that clumps up the soil. The goal of our system is to liquify the soil to ease the excavation of the soil. The main component of the GCS system is the ACP 214 an anti clay polymer supplied by Master Roc. Since the flow is going to be turbulent the ACP 214 will be mixed with water in the 100 ft of tubing that mixture will go through.

B. P&ID

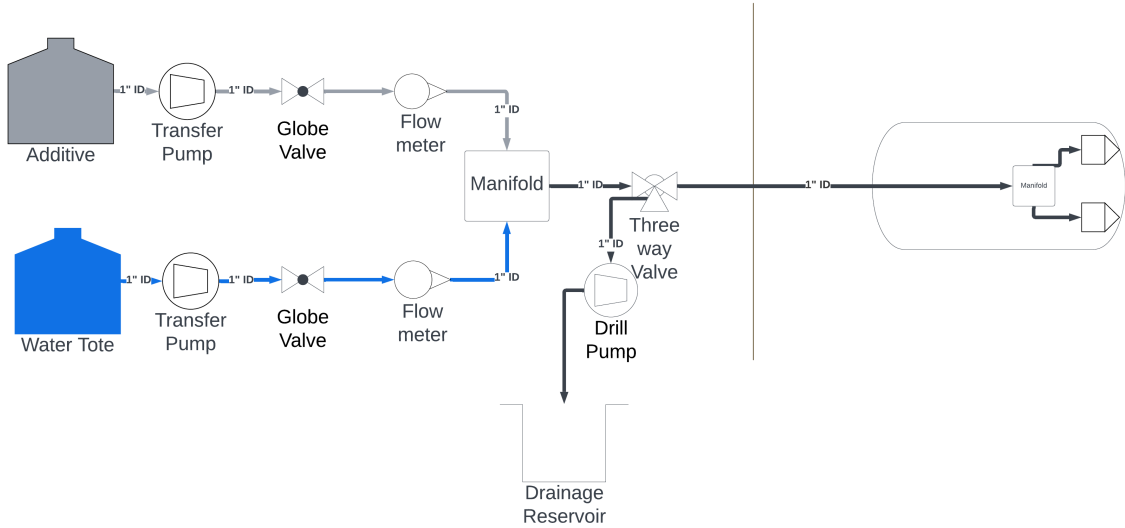


Fig. 37 GCS P&ID

The system will consist of 4 main parts. The additive line, water line, main line, and drainage line. The additive line will be made out the ACP-214 (additive), a diaphragm pump, a globe valve and a flow meter. The water line will be consisting with the same components however changing the ACP 214 to water. The drainage line will be consisting of a three way valve, a drill pump, and a drainage reservoir. Finally, the main line will consist of a manifold connecting the water and additive line and another manifold in the machine splitting the mixture into two lines going into a cone spray nozzle.

1. ACP 214

As mentioned above our main component is the ACP 214. ACP 214 is an additive with a density of $69.7 \frac{lb}{ft^3}$ and a viscosity of 60 cP. The additive is non-toxic. The ratio of the water and additive is still under testing, however, we are anticipating a ratio of 85:15 for a joint flow rate of 3.91 gpm which results in a flow rate of water ranging from according to some tests previously done.

2. Pump

Both pumps in the system are diaphragm pumps from Aquatec. The additive line pump is the 5510-1F12-B596 a diaphragm pump able to produce 0.75 gpm - 1.15 gpm at 30- 50 psi. The flow rate will be controlled with amps and global valves incase of any mechanical interference is needed. The water line pump is the 5512-1F12-B736 is rated at 3.45 gpm - 4 gpm at 20 psi to 40 psi. The water line will also have a global valve in case any mechanical interference is needed.



Fig. 38 GCS Pump

3. Flowmeter

The system will have two oval-gear flow meters one on each line. The additive line will have the 6120P-15-Y-N-T flow meter that is offered from Kytola. This flow meter is rated from 0.5 gpm - 4 gpm and can handle the viscosity of the ACP 214.



Fig. 39 Additive Line Flowmeter

The water line will have the MX12P-2SE flowmeter offered by MacNaught. This flow meter is rated from 0.79 gpm - 5.28 gpm.



Fig. 40 Water Line Flowmeter

4. Drainage Line

The drainage line will be attached to the system during testing and post dig to easily drain the system. The drainage line ends at a 50 gallon barrel that will be disposed appropriately after tests and after the dig. To avoid any more complexity the force that will be transferring the fluid is a drill pump.



Fig. 41 Drill Pump for Drainage Line

C. Analysis

Last year's GCS system had $\frac{1}{2}$ " ID tubing. This produced a huge amount of pressure loss especially since the mixture had to go through 100 feet of tubing. To avoid a high number of pressure loss especially in the main line which is 100 ft we have changed the size of the hoses from $\frac{1}{2}$ " to 1" ID. Since there are not a lot of vertical fluctuations we decided on using the Darcy-Weisbach equation to calculate the pressure drop in each line. Moreover, we used the pressure loss for the components within each respective line.

$$\Delta P = f \frac{L}{D} \frac{\rho v^2}{2}$$

(a) Pressure Loss due to friction

$$\Delta P_{total} = \left(\sum K \right) \frac{\rho v^2}{2}$$

(b) Pressure Loss during 85:15 ratio

85:15	Water Line	ACP Line	Main Line
Flow Rate [gpm]	3.329	0.584	3.9167
Reyonds Number	10528.68	34.558	6808.584
Pressure Drop [Psi]	0.01	0.006	3.488

Table 7 Pressure Loss with respect to ratio

75:25	Water Line	ACP Line	Main Line
Flow Rate [gpm]	2.9375	0.9792	3.9167
Reyonds Number	9290	57.59	4569.322
Pressure Drop [Psi]	0.009	0.09	3.525

Table 8 Pressure Loss during 75:25 ratio

These ratios are dependent on last year's tests. However, we will conduct more tests to get a more accurate set of ratios that are restricted by the components picked for the system.

IX. Tunnel Support

A. Tunnel Support Overview

1) System Overview

The tunnel support system has been completely redesigned, from a steel ring ejection system, to a PLA segment printing system. The driving factor behind this design change is scalability for price and machine length. Our previous system would have required an extension of the machine for any increases in tunnel length in order to store the steel segments to be ejected. The price is significantly cheaper for longer digs to use PLA instead of sewn steel rings. Our method of tunnel support consists of a three axes mechatronics system, an RZT mechanism that prints an 8 inch cylindrical PLA support with a thickness of 2.5 mm and an outer diameter of 0.584 m onto the inner shells of our machine, the PLA is fed from spools on the surface. Each of these segments are then ejected out by a segment ejection system, which have to account for shear forces required to remove the cooled PLA. The system has a total of 8 in-machine motors and actuators and high flow rates, which has significantly increased the power consumption of the machine.

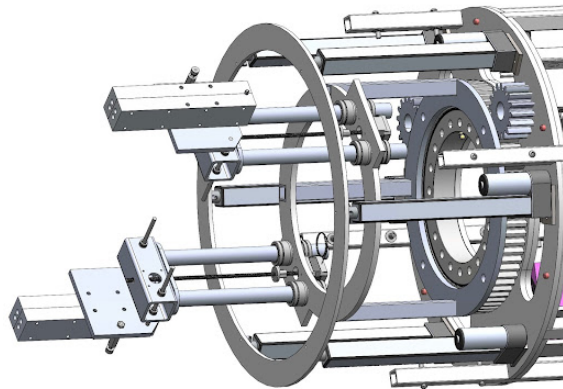


Fig. 43 Tunnel Support System Overview

The printing process will begin during launch of the TBM, where the nozzles will heat up to the required temperatures to begin melting PLA, and the extruders and 3 axes will begin their processes governed by the Tunnel Support controls system.

B. Support Segments

1) Support Segments Overview

Our segment is made of PLA, which is generally regarded as a poor material for high strength applications, however, due to our power budget and cooling capabilities, PLA was the optimal selection in terms of melting point and printability. In order to verify that the PLA support structure can hold the required soil pressures at dig depth, hand calcs, FEA, and multiple scaled tests were performed. We had conflicting data with ansys and our hand calcs, which we attribute to the nonuniform loading that the segment experiences, as opposed to pure hoop stress, so the most valuable data was obtained from the 77% scale segment tests (2.5 mm thickness).

	Support Material
Material	Polylactic acid
density at STP ($\frac{g}{cm^3}$)	1.25
Flexural Modulus (MPa)	3600

Table 9 Material Properties for PLA

2) Hoop stress test analysis

In order to come to a conclusive thickness of the printed PLA tunnel, a factor of safety needs to be accurately determined, which we hoped to achieve with this test. Due to the nonuniform stress on the printed tunnel, it is comparably harder to determine an accurate amount of stress at any given point in the structure than with uniform hoop stress. The differences between an ANSYS FEA simulation between uniform and nonuniform stresses are drastic, with the uniform simulation giving a FoS of 30 for a 5 mm thickness, confirming hoop stress hand calculations, while the nonuniform simulation gave a concerning FoS <1 along the horizontal, which is a failure of the tunnel support.

Our leading theory on the difference is that we may have had erroneous results from ANSYS, however an alternative theory is that due to the nonuniform loading, deformation occurs, and the circular support tends to “pancake” under the higher vertical stresses. Due to the brittle nature of solid PLA, such a deformation may potentially lead to fracture, which is what we suspect may be the cause of the difference in uniform vs nonuniform loading.

To confirm or disprove our ANSYS simulation we will perform a scaled soil test on a printed segment at a scale of 77% and model it in an FEA simulation, we hope to disprove our FEA simulation against data that we gather from this test and revisit methods of modelling the support.



(a) 29.6 kPa of equivalent soil pressure (FoS 1.57)



(b) Brittle Catastrophic Failure 41.7 kPa (FoS 2.2)

Our testing shows us that we are able to support 2x the required soil pressures for a support thickness of 2.5 mm, which we deem viable for the scope of our tunnel.

C. Filament Extrusion

1) Design Considerations and Evolution of Design

The original design of PLA extrusion consisted of a pellet feeding system that was fed into an Archimedes style extrusion screw, which would print backwards (opposite the direction of the TBM’s forward motion) onto the floating print, which would start the dig from a back plate on launch.



(a) Original Extrusion Screw Assembly

(b) Original Extrusion Screw

To find the geometry of the Archimedes screw, flow rate, torque, and power relation equations were used, derived from the carley et al simplified flow theory for screw extruders publications:

$$Q = \frac{A \cot(\phi) \left(\frac{L_1}{h_1 h_2} + \frac{L_2}{h_2^2} \right)}{\frac{\psi}{k} + \csc(\phi)^2 \left(\frac{L_1(h_1+h_2)}{2h_1^2 h_2^2} + \frac{L_2}{h_2^3} \right)}$$

$$\tau = \frac{600D(L_1+L_2)}{(2h_2)^2 \tan(\phi)} \frac{2\pi^2 D^2 h_2 N \sin(2\phi) - \pi d^2 v}{4}$$

$$P = N\tau$$

	Variable	Variable value (All units SI unless otherwise stated)
L_1	length of linear diameter change segment	0.1016
L_2	length of constant diameter segment	0.1524
h_1	average height of linear diameter change segment	0.00381
h_2	height of constant diameter segment	0.00254
ϕ	helix angle	0.52360
ψ	geometric constant, dependent on average diameter	0.00333
A	constant, dependent on average diameter and rotational speed	0.00575
k	die constant	1
Q	flow rate	6663.6 $\frac{mm^3}{s}$
v	fluid velocity at exit	1.3575
d	nozzle diameter	0.0025
N	angular velocity of screw	7.222
τ	torque	0.777
P	power	5.61

Table 10 Extrusion Screw Variables

Note the higher flow rate, as we were using different nozzle distances at this point in the design process.

We 3D printed a full scale model of the screw to test, and remarkably, room temperature peanut butter had a very similar shear thinning viscosity profile as 180°C PLA (derived in next section), which we used to test the flow theory.



Fig. 46 Extrusion Screw Test

The test confirmed torque and rotation numbers from the mathematical model we used. Despite this we were forced to change the design.

The first reason of the design change came in the form of a printing failure mid dig, which is inevitable and is seen commonly on commercial and industry low volumetric FDM printers to this day. In order to restart a print, we would have to line the nozzle up exactly to the point of failure and restart the print, the controls problems for this proved to be extremely challenging and was beyond the scope of what this projects intent was.

The second big issue with this method was pellet feeding, in order to consistently feed pellets at the desired mass flow rate, we needed to pump the pellets underground with compressed air. Evacuating the compressed air out of the feed tube before the extrusion screw was neccesary in order to prevent air bubbles from forming inside the the extruder. The solutions to air ingress either took up to much space, or did not bode well with rapidly rotating axes.

The current design is a filament fed nozzle with filament spools on the surface. This is fed directly into a heating element and printed onto the insides of the TBM's shells, this eliminates the air bubble problem from pellet feeding, and the controls problems associated with restarting a failed print.

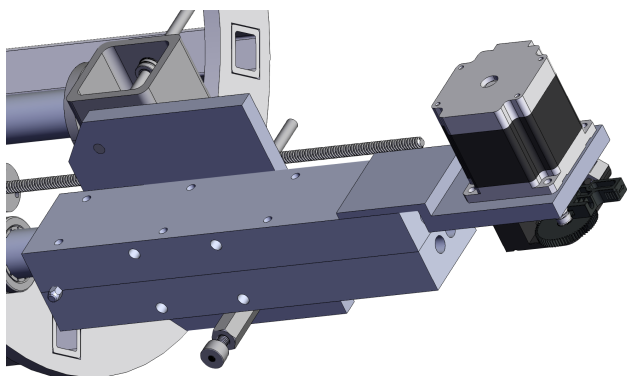


Fig. 47 New Extrusion Design

2) Volumetric Flow Rate

The nozzle assembly that we are extruding filament through has to be completely custom made because of the unique requirements that is unseen in other industries. We are using 2 nozzle assemblies that are mounted on

opposite sides of our θ axis in order to reduce rotational period of θ , and flow rate of extrusion. Using our tunnel length and dig time the flow rate was determined:

$$V = \frac{2\pi r t v}{n}$$

	Variable	Variable value
r	radius between nozzles	0.584 [m]
t	segment thickness	2.5 [mm]
v	average dig speed	0.0025 [m/s]
n	number of nozzles	2
V	Volumetric Flow Rate	5733.41 $\frac{\text{mm}^3}{\text{s}}$

Table 11 Volumetric Flow Rate Variables

3) Feeding Force

In order to maintain a pressure differential for extrusion, a force from the feeding motor is required. To determine this force, the fluid properties of molten PLA is required. Tabulated data for PLA at 180°C is used to determine the shear force vs the shear rate

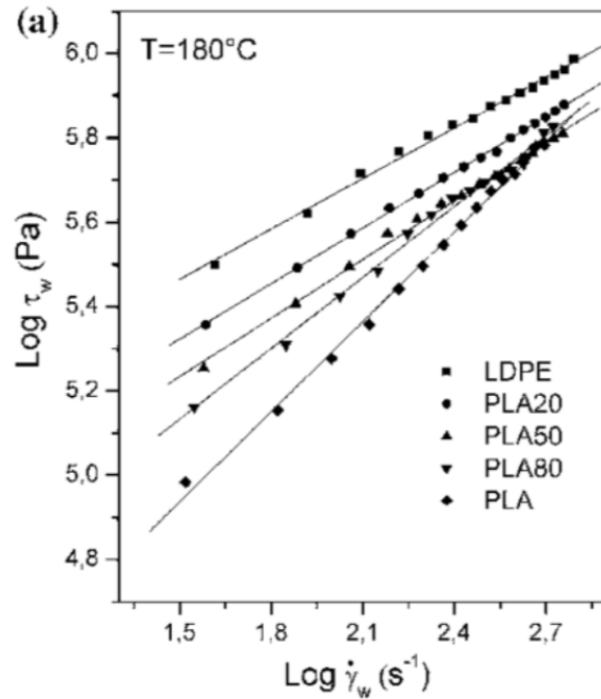


Fig. 48 Logarithmic graph of Shear stress vs Shear Rate at 180°C. "Viscosity and viscoelasticity measurements of low density polyethylene/poly(lactic acid) blends" A.Bergeret

Molten PLA is clearly shear thinning from this diagram, and its dynamic viscosity can be found by differentiating $\tau(\dot{\gamma})$ and interpolating the data. Using the relation for non-Newtonian fluids

$$\mu(\dot{\gamma}) = m * \dot{\gamma}^{(n-1)}$$

From interpolation we find $m = 30.957$ and $n = 0.775$

Using the relation for pressure differential

$$\Delta P = \left(\frac{2*m*L}{R}\right) * \left(\left(\frac{Q}{\pi*R^3}\right) * \left(\frac{1}{n} + 3\right)\right)^n$$

	Variable	Variable value
m	interpolated m value	30.957
n	interpolated n value	0.775
L	length of extrusion channel	0.254 [m]
R	radius of extrusion channel	0.0015 [m]
Q	Volumetric Flow Rate	5733.41 $\frac{mm^3}{s}$
A	Cross Sectional Area of channel	$7.06 * 10^{-6} m^2$

Table 12 Extrusion Pressure Differential Variables

Because we are using gauge pressures, ΔP is just $P = 4.254[\text{MPa}]$. So the force that the extruder motor must provide is $F = PA = 30N$. Using a 10 mm extruder gear, a required torque of $T = 0.165 \text{ Nm}$ is required

4) Linear Feed Rate

2.5 mm thick support means that we need to use a slightly larger filament size of 2.85 mm in order to prevent build up of air pockets and low pressures in the nozzle, thereby leading to inconsistent printing. With a 2.85 mm filament and a volumetric flow rate of $5733.41 \left[\frac{mm^3}{s}\right]$ the linear feed rate is

$$u = \frac{Q}{A} = \frac{5733.41 \left[\frac{mm^3}{s}\right]}{\pi * \left(\frac{2.85 \left[mm\right]}{2}\right)^2} = 898.7 \left[\frac{mm}{s}\right]$$

So our required angular velocity with a 10 mm diameter gear is 163 rad/s

The extruder mounts to our hot end in a direct drive (pulling) configuration that pulls filament from the surface. The universal extruder has enough torque to pull from the surface and still keep up with the required feed rates and the extruder is mounted to the hotend to prevent twisting and breaking of the filament.

D. R axis

1) Mechanism and Rationale

Our R-axis was designed to keep the nozzle 0.3 mm from the print bed which was determined using the ratio of a consumer FDM 3D printer layer height/distance from the build plate. With our layer height of 2.5mm this was 0.3mm from the build plate.

To achieve the 0.3 mm requirement at an acceptable tolerance, we rigidly connected a nylon ball transfer bearing to the nozzle that rolls against the print bed and is a fixed offset from the nozzle. Opposing the transfer bearing are two springs keeping the bearing pressed against the wall. Due to the segment ejection mechanism, a linear actuator is attached to the spring and will compress it to bring the entire assembly to allow clearance for the ejector to pass through.

2) Design Considerations

Our R axis is mounted to a 2x2 inch square metal tube for manufacturability and mounting versatility. It slides along steel rods to keep the distance between the bed and nozzle to 0.3mm. Four linear bearings are press fit into our square metal tube and two steel rods go through the linear bearings to mount the hot end plate. Linear bearings allow the steel rods to reliably and accurately slide on the r-axis. Having two bearings for each rod gives a small angular tolerance. Our hotend mount plate is permanently welded to the steel rods. In order to eject the printed segment there are linear actuators on the R-axis to retract the print heads allowing a plate to push the segment of the print bed. The hotend mounts to the plate with 4 1/4" - 20 screws to keep the nozzle at the same location on both sides. The hotend plate also has mounting for the R probe.

The R probe needs to be adjustable and must glide/roll against the cylindrical print bed. It is built from a screw to keep the probe fixed to the plate then a female-female thread adapter to attach the nylon transfer bearing. Using a fine thread screw and a threaded foot gives us the necessary adjustment to achieve an offset of 0.3mm from the print bed.

E. Z axis

1) Z axis overview

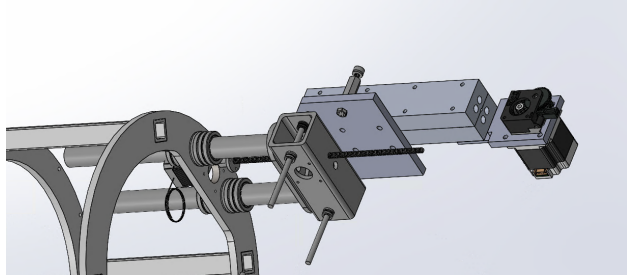


Fig. 49 ZR axis

In order to properly create our print independently of the TBM's propulsion system, we needed to create a mechanism to move the extruder in the axial direction - the Z-axis. When creating the Z-axis, we needed to ensure that there were no disturbances along the R-axis caused by the Z-axis which meant we needed a minimal deflection and clean motion. In order to achieve this, we decided to look at polished steel rods; these would offer a smooth and straight surface - reducing any chances at the device catching any imperfections or getting completely stuck. The choice of steel was due to its high specific strength properties meaning we could achieve the desired maximum deflection while taking up less space than if we used weaker/cheaper materials. With this in mind we initially aimed for a maximum deflection of 0.1 mm with a factor of safety of 20 using

$$\delta = \frac{P*L^3}{3*E*I}$$

to calculate deflection. The length was determined to be 15 inches to match the caterpillar drive's extension length, the end load was assumed to never go above 40 lbs, thus we used that and rearranged the above equation to solve for a desired diameter which ended up being roughly 1 inch. Even though we had a large FoS, we wanted to ensure there was some redundancy in the mechanism as well as additional stability which led us to increasing the number of steel rods to 2.

With rigidity taken care of, we needed to make sure the mechanism had a high enough precision to accurately keep the R mechanism aligned with the printing surface, this led to stepper motors being the only viable option. These would offer sufficient precision and to help with the speed, it was decided to have a second Z mechanism running in tandem together to keep the R mechanism unaffected by the linear motion of the rest of the drill.

F. Theta Axis

1) Theta Axis Overview

In order to print our desired cylindrical shell tunnel support segments, we required control in the theta direction. To make the tunnel support system work within our system, we needed our umbilicals to run through the middle of the machine while still being able to print our shell around it. We decided to use an outer toothed slewing bearing that was big enough to allow our umbilicals to go straight through the middle. This bearing would mount to both the (relatively) static structure of the machine and the rotating tunnel support assembly.

The total volume of PLA per layer is $3 * 2\pi * \int_{289.5}^{292} r dr = 11417.73 [mm^3]$

Each layer will take $\frac{V}{Q} = \frac{11417.73}{5733.406} = 1.99$ seconds

The mass moment of inertia of the entire tunnel support assembly is $I = 2.38 [kg * m^2]$ and given our oscillatory motion, our angular motion can be modeled as

$$\theta(t) = \frac{\pi}{2}(1 - \cos(\frac{\pi t}{2}))$$

$$\tau = I\ddot{\theta}(t) = \frac{I\pi^3}{2T^2} \cos(\frac{\pi t}{2})$$

Our peak torque is ± 5.52 [Nm] and a peak angular velocity of ± 23.68 RPM

2) Bearing

To find the required bearing spec we use tabulated data and the load relation

$$P = XVF_r + YF_a$$

Where P is the equivalent load, F_r is a radial load, and F_a is an axial load, Y, V, and X are tabulated values.

From our assembly geometry, we have $F_a = 441$ [N] and $F_r = 220.5$ [N]

We are also limited by geometry, both inner and outer diameter. The maximum inner diameter must be at least 8.23 in.

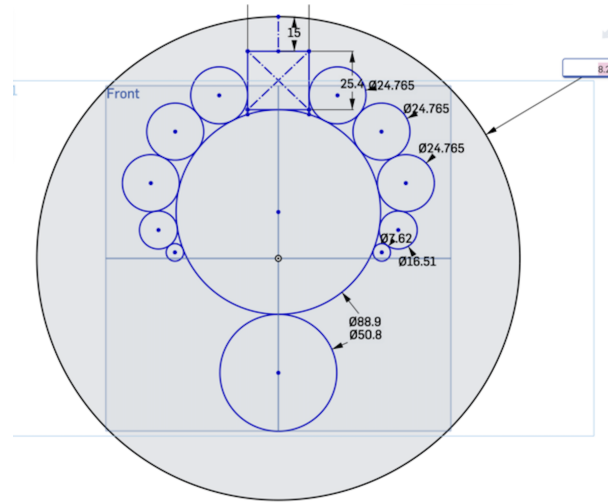


Fig. 50 inner diameter clearance

The maximum diameter is bounded by the pinion and bearing total diameter, that is: $2d+D$, where d is the pinion diameter and D is the bearing diameter.

Based on these requirements, we worked backwards from the bearing to meet our loads and found an appropriate spur geared bearing.

To drive our theta rotation, we will be using two smaller pinions that mesh with our slewing bearing, which has a pressure angle of 20° and a metric module of 1. On each pinion we will have a motor with gearbox that mount to the TBM's structure, the total gear ratio across the bearing to pinion, and pinion to gearbox is 45, so our motor must have a torque of

$$\tau = \frac{5.52}{45} = 0.123 [Nm] \text{ at a rate of } \omega = 1065.6 \text{ RPM}$$

Because we have two motors, one will be idle and one driving at all times, we had to ensure that the speced motor ($\tau @ 1065.6 \text{ RPM} = 1.4 \text{ Nm}$) could also back drive the other idle motor. Using the provided holding torque of $\tau_h = 4.5 [Nm]$, the idle motor cannot be on for the driving motor to supply enough torque to drive the bearing, so the idle motor must be deenergized(detent torque, $\tau_d = 0.2\tau_h = 0.9$).

$$\tau_h + \tau_b = 1.023 < 1.4$$

The pinions are positioned 90 degrees apart from one another on the top half of the machine for the sake of space in the back section of the machine. Because of our dual nozzle design, it is only required that we rotate 180 degrees at a time with each nozzle printing half of the shell.

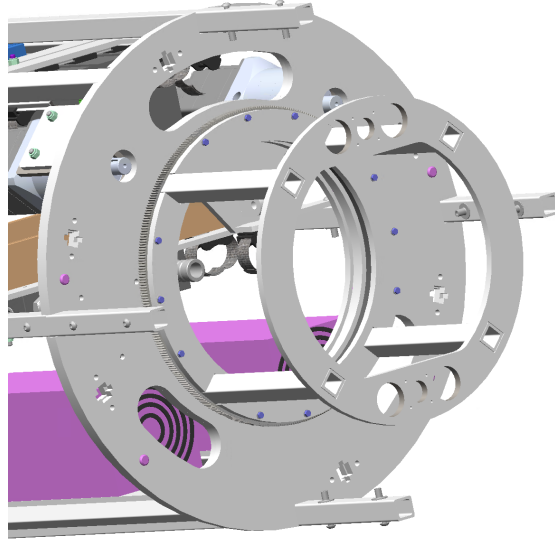


Fig. 51 Theta Overview (pinions removed)

G. Segment Ejection

1) Segment Ejection Overview

In order to eject each 8 inch segment of our tunnel when it is done printing, we need a segment ejection system. We decided on using linear actuators to push the segment out of the back of the machine. In order to be able to push the tunnel segment out, we designed a circular plate that shears the print off of the inside of the build plate. Typically, normal industrial and consumer FDM printers allow for a user to remove the print from the

print surface by using a normal force to remove the print, however we do not have the space to achieve a similar removal method, so we must remove the PLA using shear.

2) shear forces for removal

To determine the amount of shear force required for segment removal, we used the surface area of the printed hoop and compared it to results from scaled testing

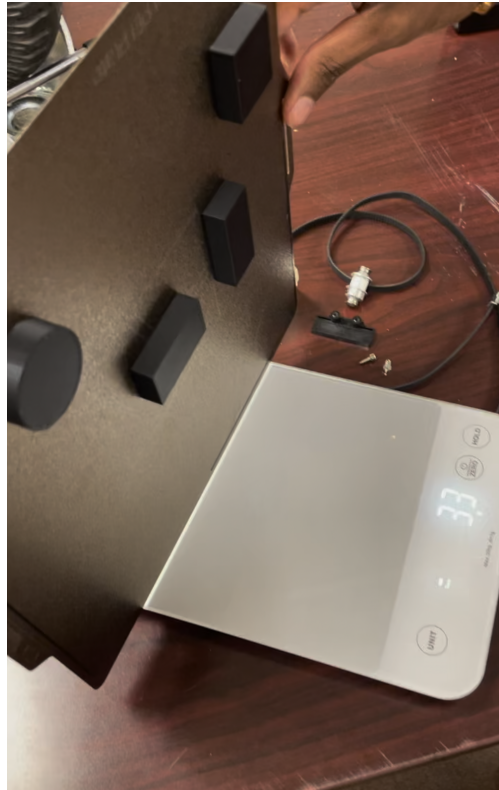


Fig. 52 Shear Ejection Scaled Test

Shape	Area[cm ²]	Shear Stress[g/cm ²]
Square	4	107.5
Square	9	107.5
Rect	9	107.5
Rect	9	107.5
Circle	9	107.5

Table 13 Shear Ejection Results, 47°C

We interpolated this to the full scale surface area:

$$A = 2\pi r z = 2 * \pi * 0.584 * 0.2032 = 7456[\text{cm}^2]$$

So we need a required force (normalized to g) of $7456 * \frac{107.5}{1000} = 801[\text{kg}]$

3) design considerations

The linear actuators are mounted in a circular pattern to a static structural plate in the machine. We selected six linear actuators with a 10-inch stroke to distribute the stresses across the entire perimeter of the printed segment. We required a stroke greater than 8 inches because each tunnel segment is 8 inches long, and the segment must be fully removed from the back of the machine before printing the next one.

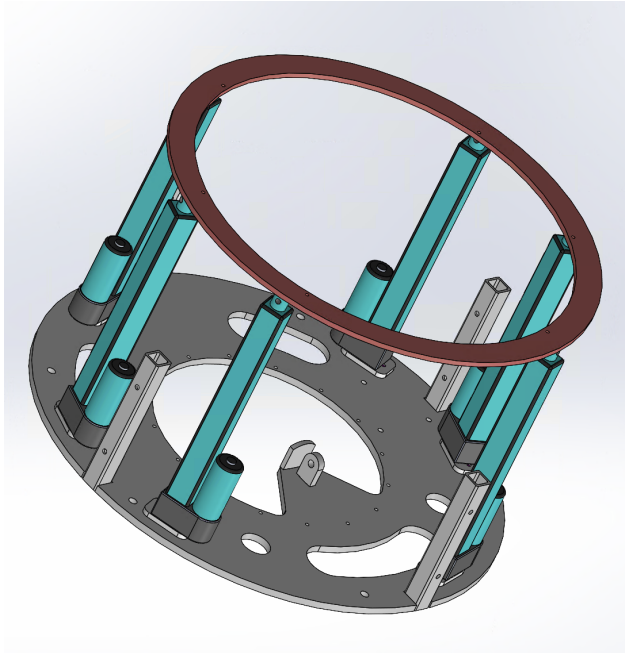


Fig. 53 Segment Ejectors

X. Structural Design and Analysis

A. System Overview

The TBM structure was designed for manufacturing, being integration-ready and accessible for internal repair. The main body of the machine is a cylinder with a diameter of 0.6096 m and a total length of 3.33m from the front tooth to the end of the last shell. Supporting this shape is a cylindrical internal skeleton created using 19 laser cut plates as our backbone. The shell enclosing the structure is 0.071" thick steel sheet metal rolled to the structure's circumference. The module structure has 7 separable sections [Soil Chamber, Front Gripper, Gearbox, Hexapod, Rear Gripper, Tunnel Support Storage, and Tunnel Support Extrusion] that all join the interface of their respective plates. The modularity is incorporated to allow for ease of repair and integration.

B. Front Structure

1) Overview

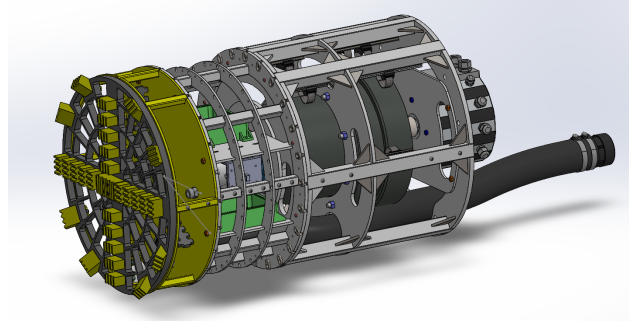


Fig. 54 Front Section

The front structure sought to increase machine mobility by minimizing its length, allowing maneuvering during mining. The front structure contains three modular sections: Soil Chamber, Front Gripper, and Gearbox reaching a length of 95.25 cm. These three sections are mounted together with -16 Grade 8 bolts, allowing each section to be detachable. There are 9 A572 steel plates and a series of welded 1.5”x1.5”x0.25”, 1”x1”x0.125” and 3/4”x3/4”x0.125” HSS A513 steel tubes. The HSS tubing was decided on due to the experience the team has with manufacturing HSS square tubing. In addition, using standard materials across the structure enables the team to buy materials from a wholesale distributor here in Denver for less than the cost of a retail solution. The 0.250”, 0.375”, and 0.500” thick plates allow the structure to be easily manufactured as the plates have notches cut on the circumference of each plate for an orthogonal fitment of square tubing. The plates also allow the gearbox to have a perfect axial alignment with the TBM. The plates are also designed to accommodate mounting surfaces for electronics and wire routing cutouts for an organized power system.

2) Design Considerations

The front section endures the thrust forces of the machine, requiring our thrust plate to withstand forces of 50 kN and requiring further design and analysis to properly react to the expected forces. In addition, the front section also contains the largest component on the machine, the gearbox. Special care was taken to ensure that the hole in the plate at the back of the gearbox section was big enough to install the gearbox through the back and then simply lined up with the mounting holes. In addition, the separation point between the gearbox structure and the forward structure was set so the grippers could be installed with the pieces separately and then combined afterward.

3) Front Section Shell

There are 10 shell pieces for the front structure, 2 soil chamber, 6 gripper, and 2 gearbox section shells. These shells are formed from galvanized steel sheet metal cut and then rolled to the machine's circumference, forming a semicircle. To attach the shells, we cut square notches alternating the top and bottom shells to meet cohesively. They are bolted to the structure using 1/4” screws with weld nuts mounted on the structure. The requirement of a fixed thread on the receiving side when attaching the shell is prominent for attaching shells quickly. When working on the internals, it's designed so that only the top shell needs to be removed, along with the design of a singular shell per section.

4) Load Case

The propulsion force is transferred into the cutting head via the cutting head shaft and then to a thrust bearing mounted to the gearbox structure. The thrust bearing is mounted to a double stack of ½” thick A572 steel plates with rib reinforcement on the back side. The torque gets translated into the gearbox, which has 9 bolts anchoring it into a plate in the gearbox section. The section is built to withstand 48,000 N of force. The gearbox can handle up to 5,400 Nm of torque, the maximum gearbox rating, this rating includes a 1.77 safety factor. Notably both of these values are much higher than we expect to see. From soil dynamics modeling we determined the maximum

push force under Basic Operationally Ordinary Mining (BOOM) to be 21.3 kN and the maximum torque to be 2759 Nm.

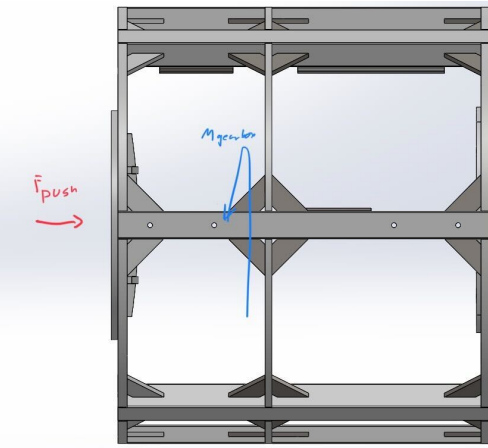


Fig. 55 Gearbox Loading

5) Analysis

Here we will focus on the analysis of the gearbox, seeing as the gripper and excavation systems have been written about in other sections. Given its complex geometry the gearbox was broken down into the weak points (front plate, welds, and bars) which then had hand calcs run on them. Through this we found the factor of safety on the bars and welds to be $FS > 10$. FEA was then run over the section as a whole to determine a comprehensive factor of safety. No weld geometries were included in the FEA, so the areas covered by the welds were ignored. This led to a minimum FS of 2.2. These results were validated through the plate deflection hand calculations where the hand calc and FEA results were well within the same order of magnitude.

Hand calcs for buckling on the gearbox members show a minimum factor of safety of 12.6 under the Johnson beam regime, and weld shear calculations show a minimum factor of safety of 12.375.

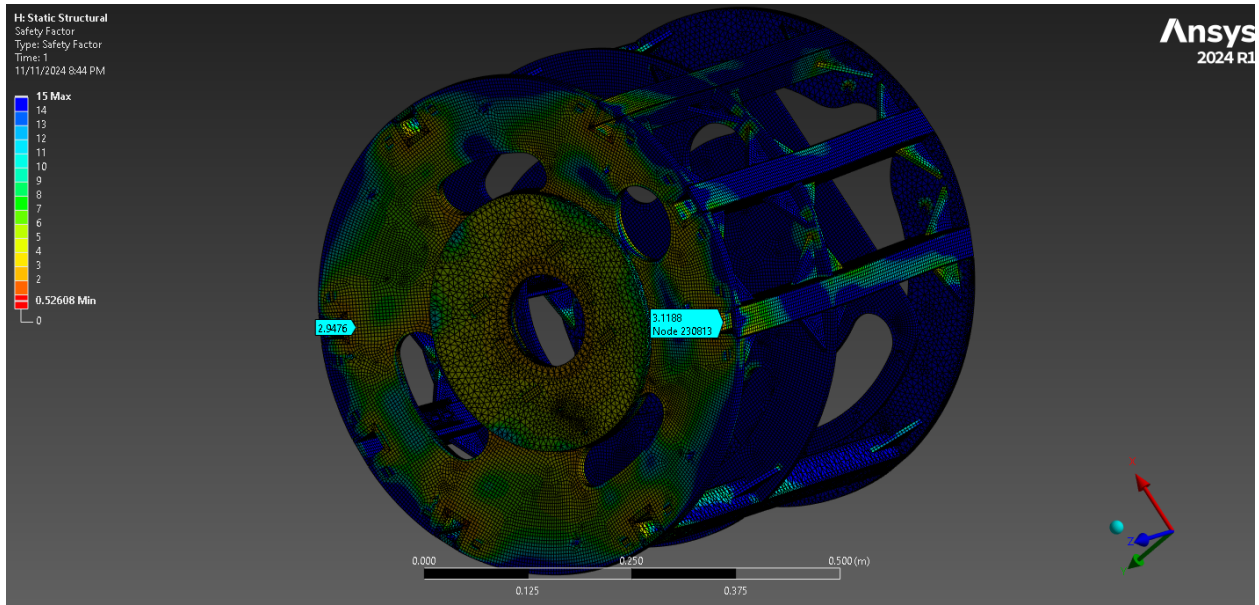


Fig. 56 Gearbox Ansys Results

6) Failure Mode

In the event of a failure, we expect to see a non-catastrophic yielding of the plate and consequently, the HHS square tube. If the ultimate tensile strength is passed, we expect a catastrophic failure in the bars.

C. Hexapod Shell

1) Overview

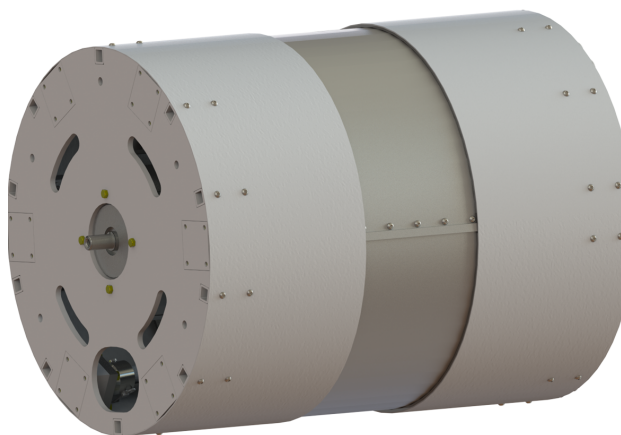


Fig. 57 Hexapod Section Shell

The hexapod shell seals the hexapod actuators and internals from the surrounding dirt during operation. Due to the movement range of the hexapod, the shell cannot simply be a single stationary piece but has to move with 5

degrees of freedom around the hexapod. The design is inspired by 3 independent articulating cylinders. The two cylindrical shells on the outside are secured to the hexapod plates. This gives a rigid structure when the hexapod is collapsed to ensure it keeps its shape. The inner cylinder is slightly smaller than the outer ones enabling it to sit inside the outer shells and keep the hexapod sealed as it extends. The geometry of the inner shell is designed so that it is physically impossible for it to become dislodged from in between the two outer shells. In addition, to ensure that the inner shell is always pulled forward, the inner and outer shells have 1/8"x1" steel bars bent and welded to the radius to prevent slippage or drag while also creating a mechanical seal. Each outer shell is bolted to the shell mounts on the hexapod plates.

2) Design Considerations

This design needed to be flexible and withstand soil pressures while minimizing the amount of soil particles accessing the internals. Our design is made of steel specifically for its welding capabilities and waterjet to minimize manufacturing error. Each outer shell is mounted using 20 screws bolted to the hexapod plates. The two inner shells are bolted together to reduce dirt particles from entering and to keep structural integrity.

3) Small Scale Prototyping

Recognizing the challenges of modeling a dynamic system with large sliding contacts, the team built a 1/4 scale physical model of the shell to test the ability of the system to turn. In that test, the prototype successfully turned at a greater than 10-degree angle. A photo from the test is shown below. This test showed the range of motion an order of magnitude higher than what was needed to complete the targeted 20m radius turn.

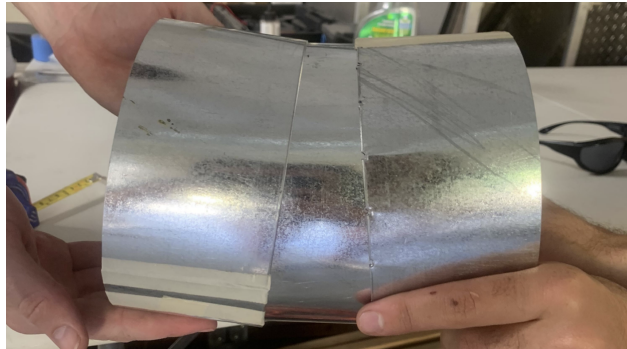


Fig. 58 Shell Scale Test

4) Expected Soil Loads

Pressures are expected to be the only force on the hexapod shell during operation. The maximum expected loading for the hexapod shell occurs at a max depth of 1.2 m measured from the center line of the TBM. In addition, for maximum loading, the hexapod is fully extended. At this depth, a vertical pressure of 14001 Pa is expected with a horizontal pressure of 5673 Pa on the upper half and 6879 Pa on the bottom half. The reasoning behind the discretization of the pressures can be found in the section on friction analysis. Since the Hexapod and its components are fully suspended and only supported at the plates, the shell is not anticipated to have a large normal force in the soil. A diagram of the expected loads and their direction is seen below.

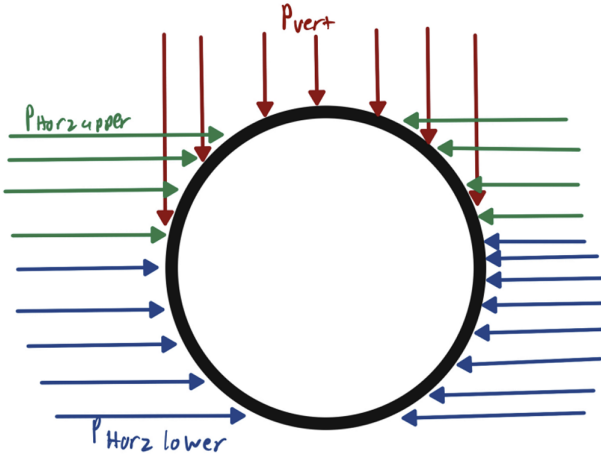
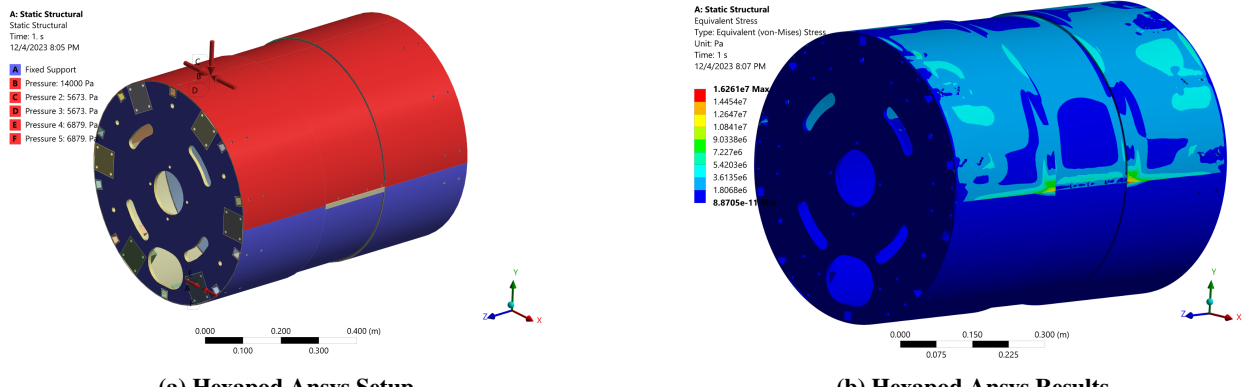


Fig. 59 Hexapod Shell Soil Loading

5) Hexapod Shell FEA Analysis

The Hexapod shell was run through FEA using the expected loads mentioned above. The 2 faces of the hexapod were held fixed while pressures were applied directly to the shells with the middle shell constrained only by the interfaces between it and the outer shells. An image of the setup is seen below. This analysis yielded a maximum stress of 16.26 MPa. The material for the hexapod shell has a yield strength of 317 MPa as quoted from osh cut. This results in a minimum safety factor of 19.5.



6) Hand Calculations

Considering that the hexapod shell is a large tube with outer radius of 12" and a shell thickness of 0.07", there are a few simplified models that can be applied to this structure. One simplification is the thin-walled pressure vessel model, which can be applied to any open-ended tube experiencing pressure normal to the surface with a shell thickness that is less than 1/20th the length of the radius. A baseline simplification can be made by assuming that the soil pressure is at its highest value of 25472 Pa and is normal to the outside of the surface directed to the center of the shell. Unlike a normal pressure vessel, this model involves an inward pressure applied from the outside of the vessel. The equations used to calculate the stress along the circumference of the cross-section of the shell are as follows:

$$\sigma_\theta = \frac{Pr}{t}$$

In this equation, σ_θ represents the plate stress along the circumference of the vessel, P represents the applied

pressure on the vessel, r is the outer radius of the shell, and t is the thickness of the steel shell. Using this model and assuming the worst possible scenario of the soil pressure being at its maximum value around the shell, the result is an in-plane stress of 10.027 MPa. This further supports the FEA analysis done in the previous section, which was able to take into account the deformation that caused additional stress at the edges of the tube.

7) Failure Mode Description

In the event of failure, the hexapod shell will buckle and cave in on the internal components of the hexapod. The top arc of the cylinders will invert.

D. Rear Structure

1) Overview

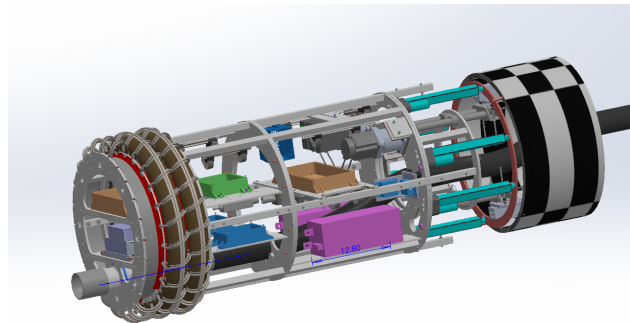


Fig. 61 Back Section

The rear section of the structure merges three modular sections: Rear Gripper, Tunnel Support Storage, and Tunnel Support, with a total length of 191 cm bolted together using -16 Grade-8 bolts. There are a total of eight A572 steel plates and a series of welded 1.5" x 1.5" x 0.25", 1" x 1" x 0.125" and 3/4" x 3/4" x 0.125" HSS A513 steel tubes. The tunnel support section includes 1 waterjet plate with the segment ejection actuators, slewing bearing, and other required system components (further information found in the tunnel support section). The design of the rear section has more waterjet shelving than previous iterations to increase the space efficiency and allow for slight design changes after manufacturing. The plates are designed with optimal mounting surfaces, including tapped holes and cutouts. This year, we are welding a series of 2", 4", 8", and 10" sections of DIN rail in places where shelving will not allow. Adding DIN rail will also allow us to attach various components without modifying the structure after manufacturing.

2) Rear Gripper

The back rear gripper structure comprises five structural laser cut plates focused around the propulsion grippers, motor controller, electrical boxes, and the expanding soil removal hose. The plates are then welded to 3/4" and 1" HHS square tube to generate the cylindrical shape. The grippers are placed at the front instead of the center so the grippers can be replaceable when separating the hexapod and first rear gripper plate. The rear gripper structure has a top and bottom main body steel shell that is bolted on with 12 1/4-20 screws. The grippers lay on top of six miniature shells that are each bolted on with two screws. There only needs to be two screws per gripper shell because they are bounded by the plates, which keep them in line, and no frictional force is applied to them.

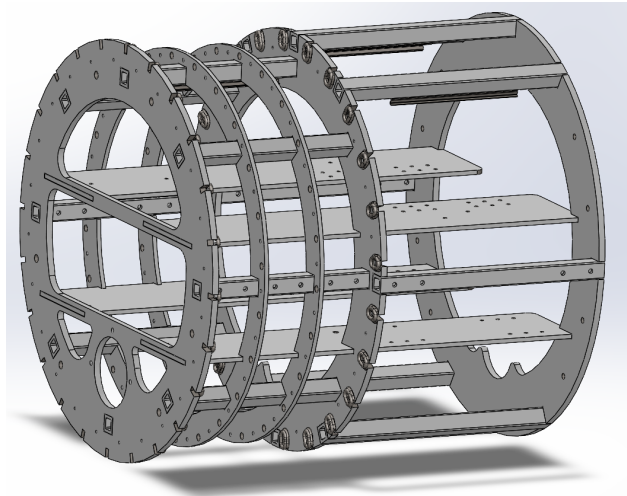


Fig. 62 Rear Gripper Section

3) Rear Gripper Loading

The rear gripper is uniquely loaded as the section is a composite of a storage section sitting behind the grippers. Under a pull scenario, the force due to the frictional load is sent through the bars, putting them under tension. The push scenario is a little more tricky. Here, the rear storage section sees little to no compressive force as the grippers activate in front of this. The load then is transferred from the front plate and distributed through the radial bars into the gripper attachment plates, then into the gripper.

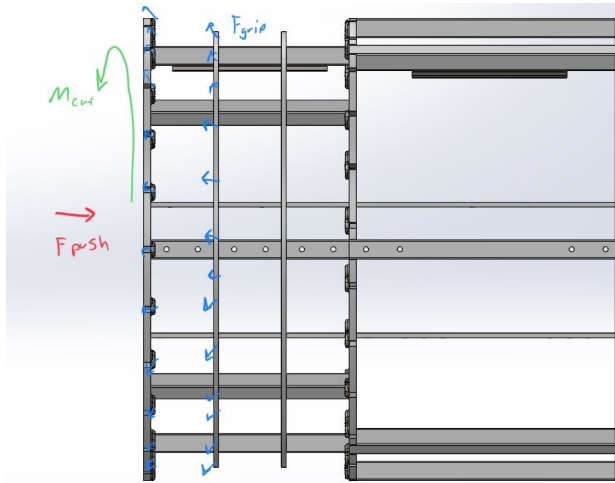
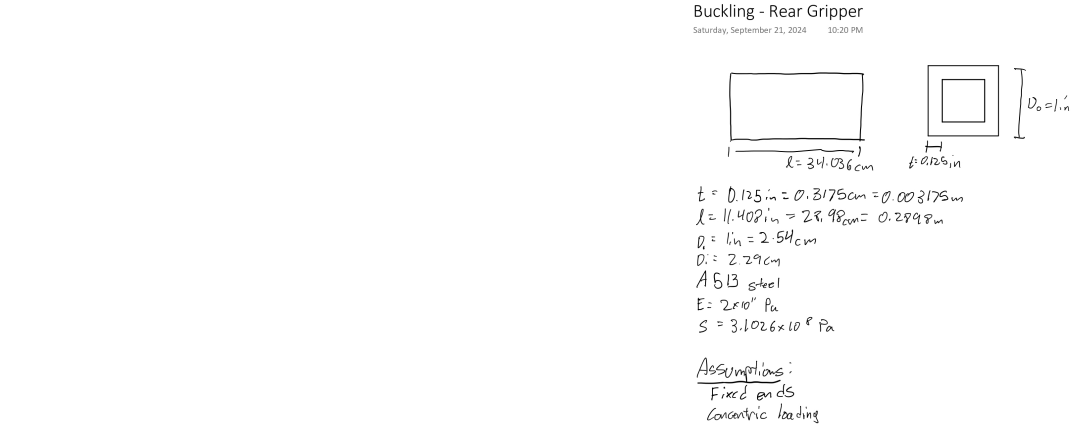


Fig. 63 Rear Gripper Load Path

4) Rear Gripper Analysis

Due to the complexity of the geometry, the rear gripper was analyzed using some hand calculations, but primarily FEA. Hand calculations were done on bars and it was determined $FS > 10$. The chain links that the grippers are attached to were also determined to have a high FS. The FEA setup consisted of a 48 kN force and a 5400 Nm moment acting on the face, and fixed supports acting as the reaction forces on the chain links. After running

FEA, the min FS was determined to be 0.44. However this was on the chain links/welds and can be ignored as an erroneous solution due to a number of reasons: 1) The high FS on hand calc values, 2) The weld geometry is not perfect and is being analyzed in areas we don't care about, 3) Some of these areas are also non-converging solutions meaning the FEA is wrong there. Outside of these specific areas, FS > 2. Furthermore we only expect to see 21300 kN of force and 2759 nM torque based on our soil model, so the results we have are around a nominal FS > 4, under BOOM. The failure mode we expect to see in the structure is bending in the plate. Under pull, we see a minimum FS of 1.5, however the areas of abnormally low FS are at right angle corners... known to be a problem in FEA. Furthermore, the physical machine will have the sharp corners filled in with weld beads. We also expect to see a failure mode of plate bending in this scenario.



Weld Shear Calculations - Gripper

Saturday, September 21, 2024 1:12 PM

Transverse weld loading

$$D = 0.75 \text{ in}$$

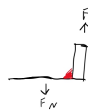
$$k_e = 0.25 \text{ in}$$

$$t = 0.176 \text{ in}$$

$$\Sigma L = 7 \text{ bars} \cdot 3 \text{ in}$$

$$\Sigma L = 21 \text{ in}$$

$$F_{ew} = 70 \text{ ksi}$$



$$\text{Weld strength/unit length} = 0.6(F_{ew})(t)$$

$$S = 0.75(0.6 \cdot 70)(0.176 \text{ in})$$

$$S = 5.57 \text{ kip/in}$$

$$\Sigma S = 5.57 \cdot 21 = 116.9 \text{ kip} = 520 \text{ kN}$$

$$FOS = \frac{520 \text{ kN}}{48 \text{ kN}}$$

$$FOS = 10.8$$

$$\text{Solve: } I = \int_0^a \int_{A_2}^{A_1} y^2 dy dx - \int_0^b \int_{A_2}^{A_1} y^2 dy dx \\ I = 2.37 \times 10^{-3} \text{ m}^4$$

$$A = D_o^2 - D_i^2 \\ A = 0.00028 \text{ m}^2$$

$$k = \sqrt{\frac{E}{A}} \\ k = 0.00916 \text{ m}$$

$$S = \frac{F}{k} = 20.55 \Rightarrow \text{intermediate col} \Rightarrow \text{Johnson eq.}$$

$$P_{cr} = A(S - \frac{1}{E}(\frac{\pi k}{2})^2)$$

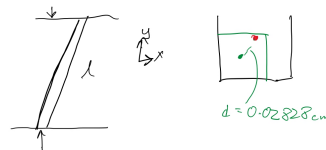
$$P_{cr} = 85.6 \text{ kN}$$

$$\text{Load/bar} = 48 \text{ kN} = 6.85$$

$$FOS = \frac{85.6}{6.85}$$

$$\boxed{FOS = 12.5}$$

Assuming Some Eccentricity



$$e = 0.0565 \text{ cm} \\ c = \frac{1}{2} \text{ in} = 1.27 \text{ cm}$$

$$E_r = \frac{ec}{K^2} = 0.085$$

$$E_r < 0.1 \Rightarrow \text{no issues}$$

(a) Rear Gripper Weld Shear Hand Calcs

(b) Rear Gripper Buckling Hand Calcs

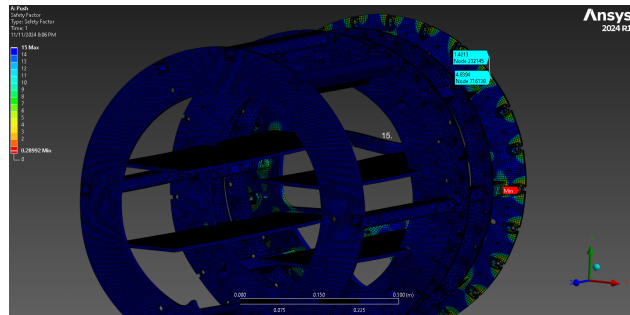


Fig. 65 Rear Gripper Load Path

5) Tunnel Support Storage Structure

The tunnel support storage structure is our simplest section, with only two waterjet plates welded with 1" square tube. This section is foundational in housing key electronics, including power supplies, inclinometers, network switches, tunnel support boxes, and tunnel support theta motors. This section is optimized for space efficiency and versatility to support future electrical and integration modifications. Furthermore, we have placed 8 sections of din rail to maximize versatility to help wire management and component integration.

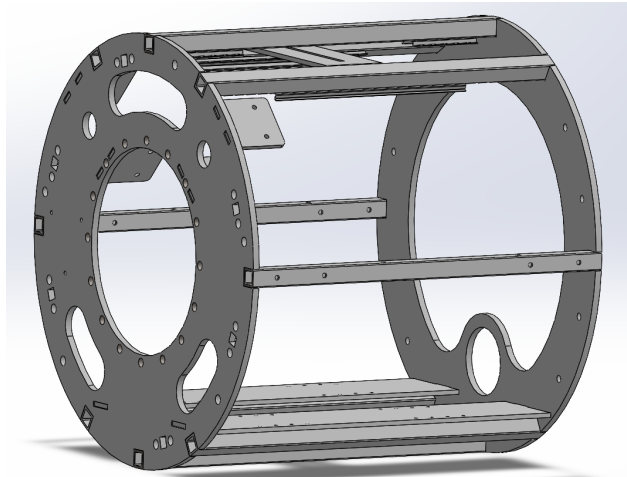


Fig. 66 Tunnel Support Storage Section

6) Tunnel Support Storage Analysis

There is not much that needs analyzing in this section. The only load this sees is the tension force caused by pulling the tunnel support section. No FEA was done, as hand calculations are sufficient under such a simple loading condition. Under these conditions, the section has a $FS > 10$. This section is not expected to fail before anything else.

7) Tunnel Support Structure

The tunnel support structure only includes one " A572 waterjet Plate and 1" HHS tubing welded around the plate. This Plate is bolted to the tunnel support storage section with five 1/2-13 bolts and supports the TS theta bearing, ejection actuators and TS cooling shell. Further information can be found in the tunnel support section.

E. DAWGS

1) Overview

The DAWG (Distance-saving Animal-shaped Water-resistant Gantry) will be towed behind the machine during operation and will house electrical connections, pneumatic lines and quick disconnects, cooling and ground conditioning system quick disconnects, and will support the soil hose. The bulkhead will be manufactured out of $\frac{1}{4}$ inch steel plate and have its features waterjetted. We will be using a sled-like design instead of wheels, so the bulkhead will slide behind the machine instead of roll, which will provide increased stability. The bulkhead will be towed via a towing bracket, which can move up and down but will keep the bulkhead aligned behind the machine.

2) Bulkhead

The bulkhead will house several connections for electrical, pneumatic lines, cooling connections, and the soil hose. The electrical connections consist of two ethernet ports, six camlock connectors, and one 24 volt emergency stop connection. There will also be six pneumatic lines going to the bulkhead, each with a NPT bulkhead fitting. Finally, cooling will require five quick disconnects and one camlock. Below is our current design idea for the bulkhead, which depicts the general shape that our final design will have.

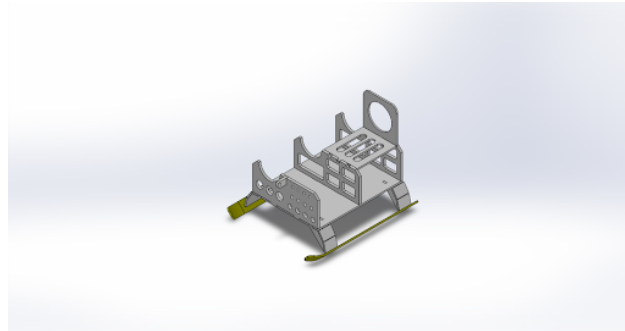


Fig. 67 DAWG

F. Manufacturing and Assembly

1) CAD Integration

The precision of our CAD model is integral to design, analysis, manufacturing, and integration. Using the previous years model as a reference, our new design includes key features in CAD assembly organization, allowing for ease in updating and maintaining the current iteration. As our manufacturing timeline is behind last year, we've ensured all components in the model have a mounting location, reducing the amount of integration and assembly issues encountered previously. The model includes all PCB's, wiring, manifolds, pneumatics, etc. The primary mounting method includes DIN rail and tapped holes in the plates, allowing bolt-on components.

2) Mechanical Workshop

Manufacturing of the structure has been in progress since October 2024. The team has 17 of 19 laser-cut plates and all other materials needed to complete the skeleton manufacturing. Manufacturing processes include flux core welding, grinding, and cutting square tube. The structure is designed so that the front and the back sections will be built independently and later joined via the hexapod. The modularity design of the structure means there is no particular order in which the structure has to be manufactured or assembled. A new manufacturing method this year includes 3D-printed jigs that align plates to be orthogonal and in the correct position before weldment.

The team plans to continue manufacturing and assembly of the structure in-house at our mechanical workshop.

3) Manufacturing Processes

Currently, the soil chamber and gearbox have been manufactured. We plan to start integrating components mid-November and complete manufacturing before December. Our delayed manufacturing has been replaced with an organized and planned component layout that expedites integration and assembly.

XI. Launch Structure

A. Launch Structure Overview

Our launch system utilizes the same structure, including the tilt rail and A-frame. We have deleted the car jack which previously tilted the TBM to its launch angle, because the A-frame was designed to place the machine at the correct launch angle (resting on the ground). We are using the tilt frame as both a build stand and launch stand, allowing a smooth transition from working on the machine to mining within 1 hour.

The overall concept for the system is to shield the TBM for launch, with the TBM pushing off a moving backstop instead of using grippers. While the TBM slides down a set of rails on the initial pushes, this backstop, rigidly attached to the back of the machine, will ratchet down a series of teeth. This idea was heavily inspired by roller coasters. This entire rail and teeth structure, referred to as the tilt rail, is set on the 3" pin located on the A-frame, a structure supporting the TBM weight and providing the tilt rail to pivot to the launch angle. As the tilt rail is set on the A-frame it is then further lowered pivoting the TBM to its launch angle.

This enables us to launch at any angle from flat to -13.5 degrees by adding or removing soil under the front of the tilt frame. The 3" pin also transmits both the propulsion force and cutting head torque into the ground. Finally, the entire structure sits on a 4x4 ft plate to distribute the machine's weight and launch stand into the soil. The plate ensures that a pressure of only 7 kPa is transmitted into the soil so that the launch structure does not sink into the ground. An image of the machine on the launch structure is seen below. On launch a maximum propulsion force of 12484 N is expected and a maximum torque of 1900 Nm of torque is expected. That said under BOOM assuming frictional forces we could see up to 21,300 N max propulsion.

B. Tilt Frame

1) Full Launch Structure Analysis

FEA analysis was run on the launch stand to ensure that it would survive the worst case loading scenario. This occurs when the TBM is starting launch and thrusting with the maximum expected forces for launch while also spinning the cutting head with the maximum rated torque. The Setup of the FEA simulation is seen in the figure below.

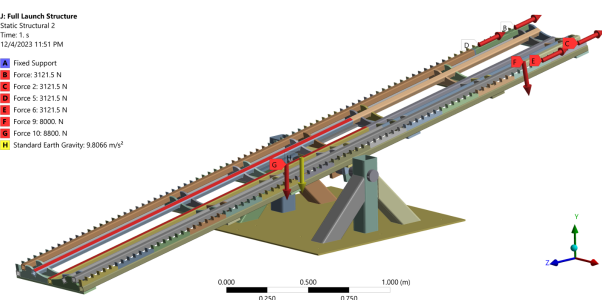


Fig. 68 FEA Setup for Launch Structure

The results of this analysis are a maximum stress of 380 MPa that results in a minimum factor of safety of 0.91. This minimum value however is localized to a single node at a right angle being characteristic of a node failure. Excluding this singular node failure the factor of safety is above 2 for the entire launch structure. The factor of safety distribution is seen in the figure below.

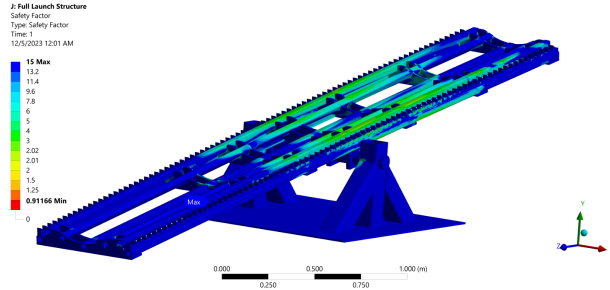
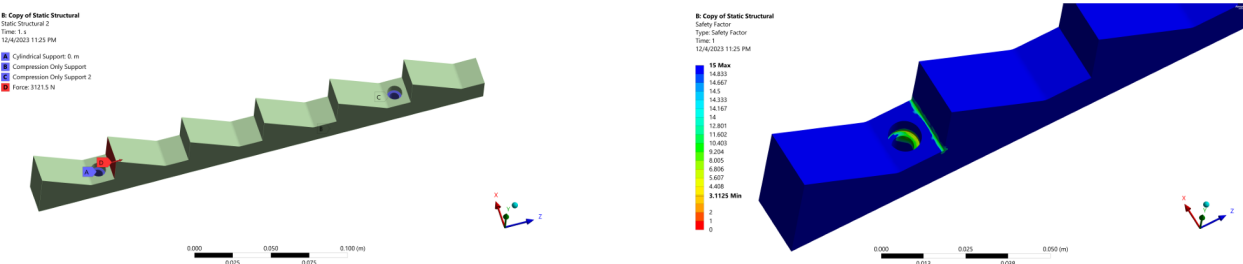


Fig. 69 FEA Results for Launch Structure

2) Launch Stand Teeth

The teeth on the tilt frame react the propulsive force of the TBM into the tilt frame. There is a set on each side and each tooth is 2 inches apart. 2 inches was decided since the stroke length of the actuators is 8 inches and the team wanted at least 1/4 stroke resolution in order to ensure that each push was making meaningful progress. Each tooth section is 12" long and a total of 28 sections are used. The teeth are manufactured out of Aluminum 6061 and bolted to the tilt frame using 2 1/4" bolts that are countersunk into the tooth. These bolts have a factor of safety of 9.01 for the maximum expected load of 3121 N. FEA analysis was performed on the teeth to ensure that they could withstand the maximum propulsion load on each tooth. The maximum stress occurred for the second tooth. The setup and results of the analysis are shown below. The minimum factor of safety is 3.11.



(a) Ansys FS Teeth Setup

(b) Ansys FS of Teeth

3) Push Plate

The push plate is rigidly attached to the back of the TBM via a force bracket that transmits the pushing force of the TBM to the push plate, which we anticipate to be 23 kN. The push plate has four roller arms that slide down the tilt frame's teeth that react against the launch force. Additionally, the push plate also has to support the bulkhead during launch, so a curved plate extends out of the rear of the push plate for that purpose. The TBM will also create around 3000 N-m of torque, so the push plate reacts against the launch stand to prevent the TBM from tipping off of the stand. Additionally, the push plate will carry the bulkhead during launch. We expect our push plate to effectively handle this loading, with the plate having a factor of safety of 2.0, the long arms a factor of safety of 2.7, the short arms a factor of safety of 14, and the pins in the arms a factor of safety of 6.9.

The push plate will be manufactured out of $\frac{1}{2}$ inch A572 steel plate using a waterjet. The ribs on the plate will also be waterjet from the same $\frac{1}{2}$ plate and will be installed using slots cut into the plate. Both the long and short

arms consist of two $\frac{3}{4}$ inch thick plates connected by a $\frac{3}{4}$ inch-diameter pin at either end. Additionally, $\frac{1}{2}$ inch support plates have been added around the mounts for the arms to reinforce those sections of the plate, where we have high stress concentrations. The bulkhead support plate will be made from a 0.07-inch plate so it can be easily bent to the desired curvature. The push plate will attach to the rest of the machine via a force bracket. This plate will be supported by three 1 by 1 inch 11 gauge square tubing. The force bracket will be bolted to the machine and plate via bolts so it can be easily and quickly attached and removed. Below are images of the push plate in CAD:



Fig. 71 Launch Plate

Fig. 72 Launch Plate with Mounting Brackets

The push plate's biggest failure concern is bending stress. Shear and moment diagrams for the plate have been plotted in the below figure.

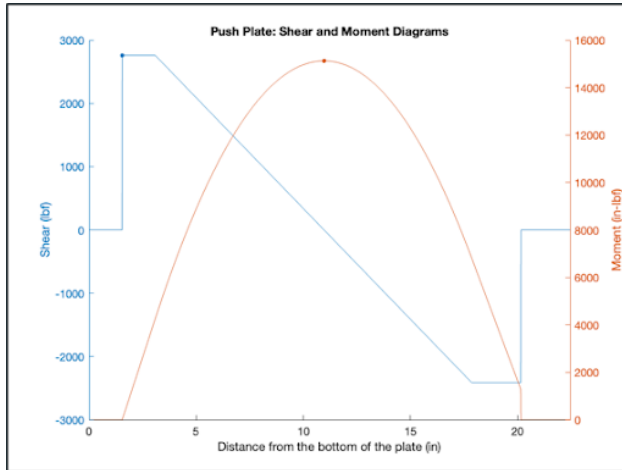


Fig. 73 Internal Shear and Moments for the Plane Plate

As expected, the maximum moment is in the center of the plate, coming in at around 15,000 in-lbf. The maximum shear force is near the bottom of the plate, which is because the short arms at the bottom of the plate experience more force than the long arms at the top of the plate. What we really care about, however, are the stresses throughout the plate, which are plotted below.

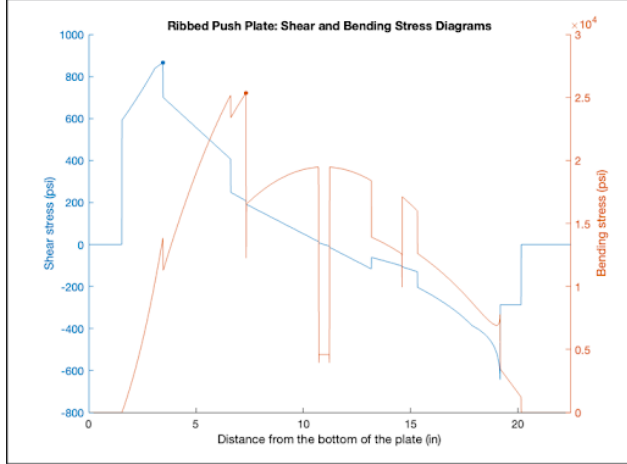
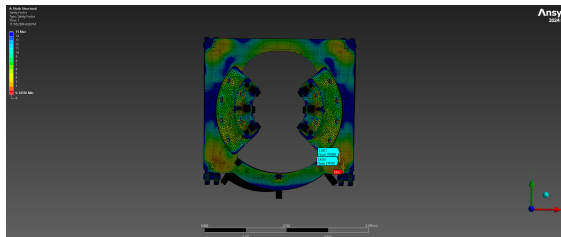


Fig. 74 Internal Shear and Moments for the Ribbed Plane Plate

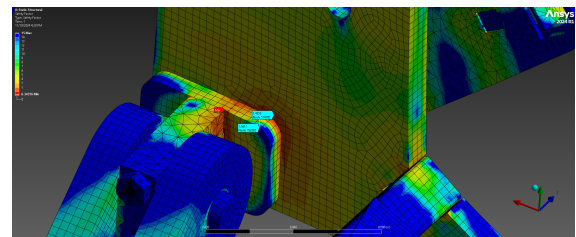
As seen above, the maximum shear stress that our plate experiences is only about 870 psi. Bending stress, however, maxes out at around 25,000 psi. The dip in the middle of the bending curve is due to the rib that we added at the center of the plate to reduce the bending stress.

4) Push Plate FEA

In the FEA, we see a factor of safety outside the welded area of 1.4. The FEA has two problems that can be safely ignored. Firstly, the weld geometry is not modeled. This isn't a massive deal though as we can ignore the area covered by this weld (1/4") weld. The second problem is the tubes are modeled as A572 instead of A513 steel. A513 has a yield strength of abt 88% of A572. This also isn't a massive deal considering we have a pretty good FS on those tubes, i.e. they are not the failure mode. All that said, the factor of safety at the two points is probably accurate. The other thing we have going for us is the frictional load should be much lower than was simulated, as it that assumes forces at max depth. We should only be hitting around half the load that was simulated.



(a) FEA on Launch Plate

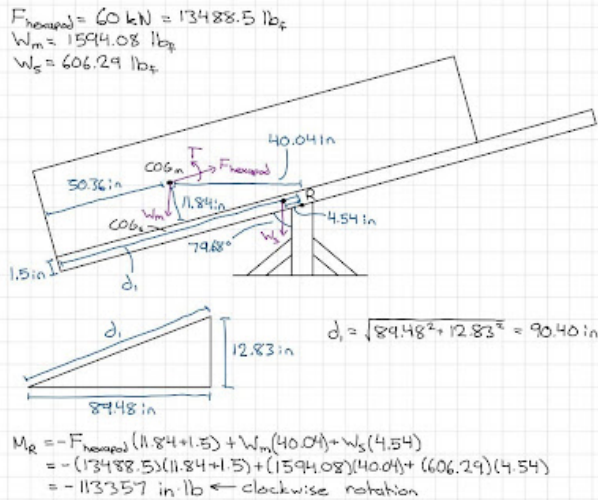


(b) FEA on Launch Plate Zoomed into Worst FS

C. Launch Structure Analysis

1) Stand Tipping

When the TBM is on the launch stand, the launch stand has to support both the weight of the machine and the pushing force from the hexapod. The stand tipping is a concern, mainly due to the force of the hexapod. The below free body diagram and hand calculations demonstrate the risk of tipping.



NOTE: This is a worst case scenario, but we will see the launch stand rotate in this situation. Whatever solution we come up with to keep the front end down (we've mentioned straps or bunker blocks thus far) will help counteract this rotation. Probably the best way to prevent this is to add supports at the far right, which could be supporting rods, bunker blocks, etc.

Fig. 76 Hand Calc of Launch Stand Tipping Likelihood

These calculations conclude that the launch stand will tip over during launch, and to prevent tipping, a force of 1260 lbf is needed to be applied at the front of the launch stand. This force will be supplied in one of two ways: 1) a bunker block will be mounted to the front of the launch stand, or 2) supports will be installed at the right end of the launch stand to provide compressive support to tipping.

2) Machine Tipping

The 300 N-m torque created by the TBM poses a threat to the machine rotating and tipping off of the stand completely. This will occur if the reaction force from the torque against the launch stand is greater than the weight of the machine. The below hand calculations show that this reaction force is less than the weight of the machine, so we do not have to worry about the machine tipping off of the launch stand.

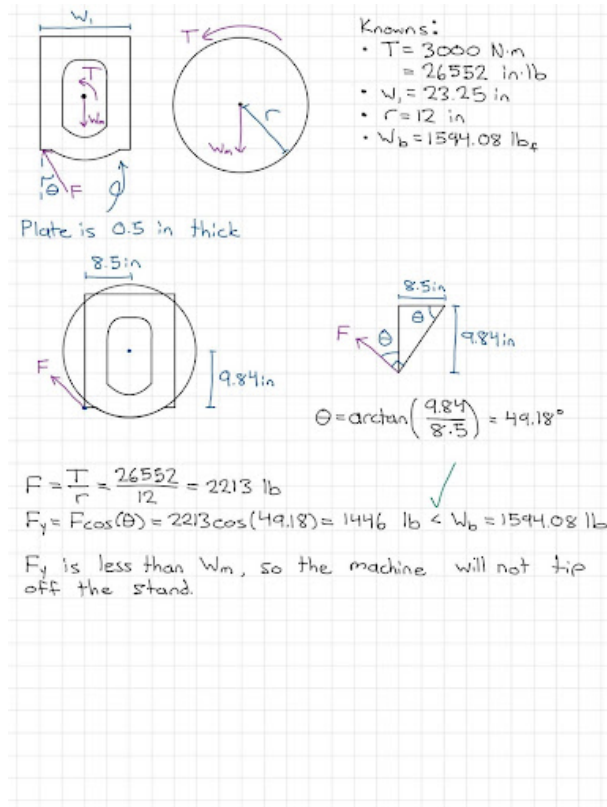


Fig. 77 Hand Calc of Possibility that Machine Rotates off Launch Stand

D. Equipment Lifting and Transport Structural Analysis

1) Predicted Loads

Our loads are expected to be around 2000 lbs. This is an estimation within about 10%, as the TBM will change through iteration during our test dig, and developing into the competition.

2) Failure Mode Description

Our failure mode would be the machine CG not being placed in between the forks, or too close to the forks. In the first scenario, the TBM won't be able to be picked up properly. The second scenario would result in a failure if the forklift were to accelerate too fast.

3) First Principles Calculation for Safety Factor/FEA

The launch stand consists of 6 A513 steel bars running underneath it. As seen in the FEA done in the tilt frame analysis our safety factor is at least 2.

4) Lifting, Transport Procedures

Our lifting and transport procedures plan is to use a forklift on our launch stand. The launch stand is built to withstand a forklift carrying it and the TBM. We plan to mark the center of gravity on the build stand and lift with the forks of the forklift evenly placed on either side. An alternative method if the proper equipment is available is to lift using eye rings placed on the four corners of the build/launch stand.

XII. Software System

A. Overall Overview and Architecture

1) *Overview* Our software system is built to handle all TBM operations. Using autonomous controls our system is

designed to launch the machine, and autonomously excavate a tunnel along a predefined parabolic path while also printing cylinders to support the tunnel along the way. To facilitate this process our system includes monitoring of all onboard sensors and manual override of all components in the event of system failure. Our design approach follows a distributed node architecture which allows our system to be broken down into several adaptable components that can be modified as our system evolves. This approach allows us to efficiently deploy unit tests, new components or subsystems, and new features, and isolate specific nodes for debugging. Additionally, as the software team grows, we are able to leverage the distributed architecture in development by parallelizing tasks which allows for a greater focus on testing and integration.

2) *Tech Stack*

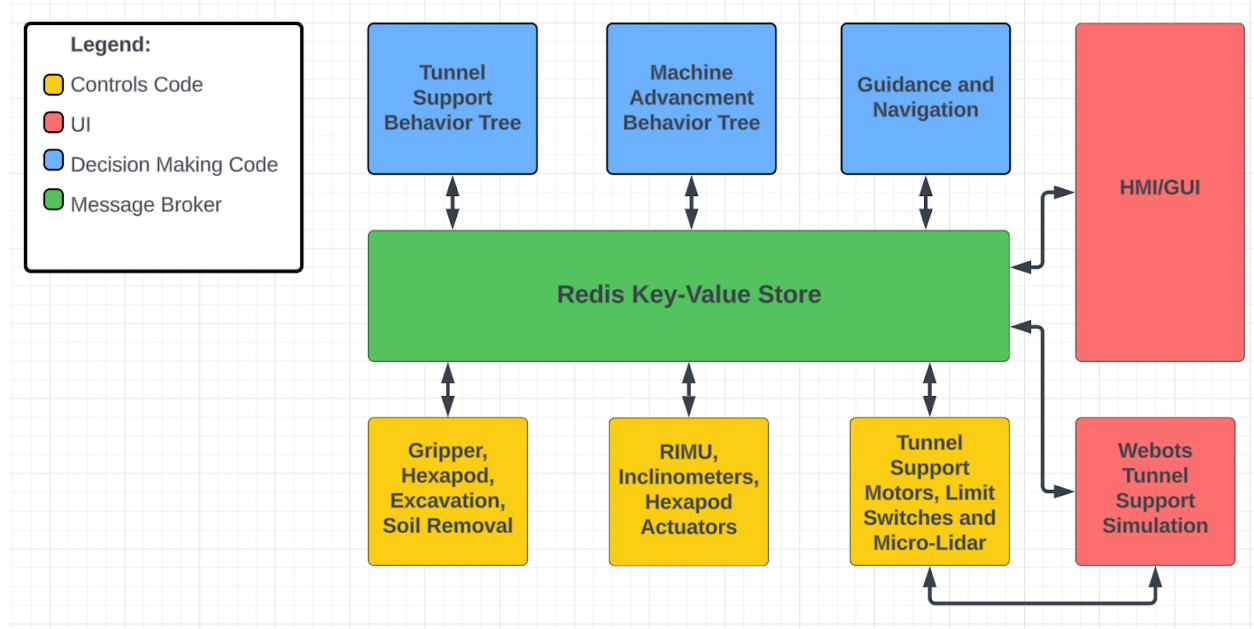


Fig. 78 High-Level Software Architecture

Our system's software is built on both low- and high-level components, using Arduino C and Python. For firmware, which handles microcontroller level control and sensor interfacing, we use Arduino C. All other software is written in Python.

While Python may lack the efficiency of other popular languages like C++, it remains our primary choice for high-level software due to its popularity and ease of use. This choice makes development more efficient and offers extensive support and documentation for the various packages used across the system. In addition, Python's relatively low barrier to entry significantly aids with onboarding and team retention.

Given the fact we use Teensy 4.1 microcontrollers, we develop all control code in Arduino C. C's efficiency, performance, and low memory footprint are integral aspects required by low-level control code making it the ideal choice for our system.

This year, we have chosen Redis for message passing and Protocol Buffers for defining message structures throughout our system. In past years we have chosen ROS1 because of its support for C++ and Python and

because of its considerable list of tools and features for robotic applications. However, ROS requires substantial boilerplate code and frequent environment configuration to adapt to system changes. Redis, by contrast, offers the critical features we value from ROS but requires virtually no setup or ongoing configuration. Additionally, Redis uses a broadcast communication model, which aligns better with our system's needs than the point-to-point communication ROS provides. On top of Redis, we also use Protocol Buffers to pass defined message structures among various processes occurring during the dig. The immutability of these structures allows for efficient program development, as it reduces the effort needed to validate message logic across systems. By using the built-in binary encoder that comes with Protobuf we can serialize message objects into raw binary. We then take this encoded object and further encode it with base64 so it can be more efficiently utilized in the control code.

The GUI is designed using QT Designer to visually design the GUI and then we converted the .ui file to a python file using Pyuic to write extra functionality and reference the objects in the backend. The QT framework is written in C++, so even when we are writing the backend in Python we are still using the C++ backend, the bridge utilizing C++ speed and reliability.

3) Behavior Tree

The structure of our boring machine behavior is modeled by a behavior tree, a hierarchical system used to execute modular actions. We chose the behavior tree system because of its modularity, readability, reactivity, and mode-specified behaviors.

- modularity: The whole behavior tree is composed of modules, from subtrees to leaf nodes, and can be implemented and tested as such. We break the reactivity into action modules. There are two main subtrees in our behavior tree, manual and autonomous. Depending on the mode that the machine is in, the respective subtree will be ticked. Within the tree, various subsystems have several nodes distributed across the tree including hexapod, grippers, ground conditioning, excavation, etc. As we develop we can leverage the behavior trees modularity and remove or add subsystem nodes as we please without consequence.
- reactivity: Due to the behavior tree structure and method of execution we can organize the tree node in such a way that reacts to the changing environment throughout the dig. As we receive sensor data over Redis we can interpret the data according to active nodes and subsequently react using preceding or previous nodes within the tree.
- Idle: when in idle the tree does not execute any actions. The tree will continue to tick to continue to check for an estop command but will otherwise do nothing. When in operation estop the tree will go into a similar state.
- Dynamic Manual: To improve the readability and complexity of the code we have opted for a single action node which will control all manual processes. By passing integer values, which we have defined with enums, we can control the dynamic node through the GUI. When active, the manual node will continually listen for a command sent over Redis. Using the received value we then search a dictionary of various available actions and add it to the tree. Once the subsequent node reaches a success state the node is removed and the manual node can then receive a new action. The available manual options consist of inflating and deflating the grippers, pushing and retracting the hexapod, spinning the cutting head, etc.
- Autonomous: When the autonomous subtree is active nodes will autonomously be called in sequence to execute push and retract actions. By reading sensor values through Redis the tree can determine when it is appropriate to continue to the next action. Each action checks its respective subsystem and can determine its progress by returning one of three states; running, success, or failure. This architecture allows us to ensure that all necessary actions are running properly before pushing the machine. Moreover, the ticking behavior of the tree allows us to continually check these prior conditions even after they have returned successfully. In the event of an error, the tree can backtrack, correct the said error, and return to its prior state when it is suitable to do so.

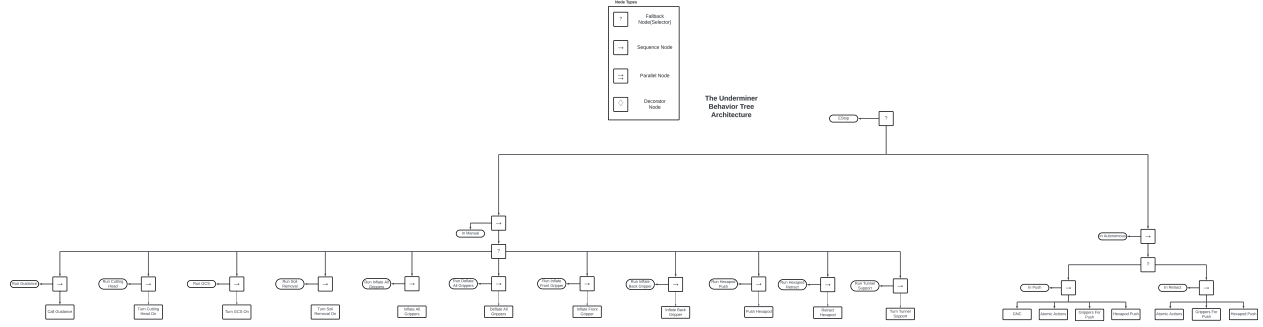


Fig. 79 Behavior Tree Architecture

B. Hexapod

1) Overview

The hexapod, consisting of 6 linear actuators, is the final step of our push and retract sequences. The Behavior Tree structure holds the sequences and conditions that the machine will follow in both the manual subtree and the autonomous subtree. There is built-in functionality that allows the machine to be controlled by either the manual controls, which can be called by buttons within the GUI, or the autonomous behavior tree which will check conditions and follow a sequence of commands, autonomously sensing the environment and adapting properly.

Using our current guidance point we can generate leg lengths to steer the TBM in the desired direction. Using a custom inverse kinematics function suited for the steward platform configuration of the hexapod we can create arrays of size 32 for each of the 6 actuators. Through this method, we can gradually turn the machine properly without stressing the structure of the machine. To retract we take the same array in reverse to properly pull the back section of the machine forward. Throughout both the retracting and pushing phases all encoder values will be verified to ensure proper functionality.

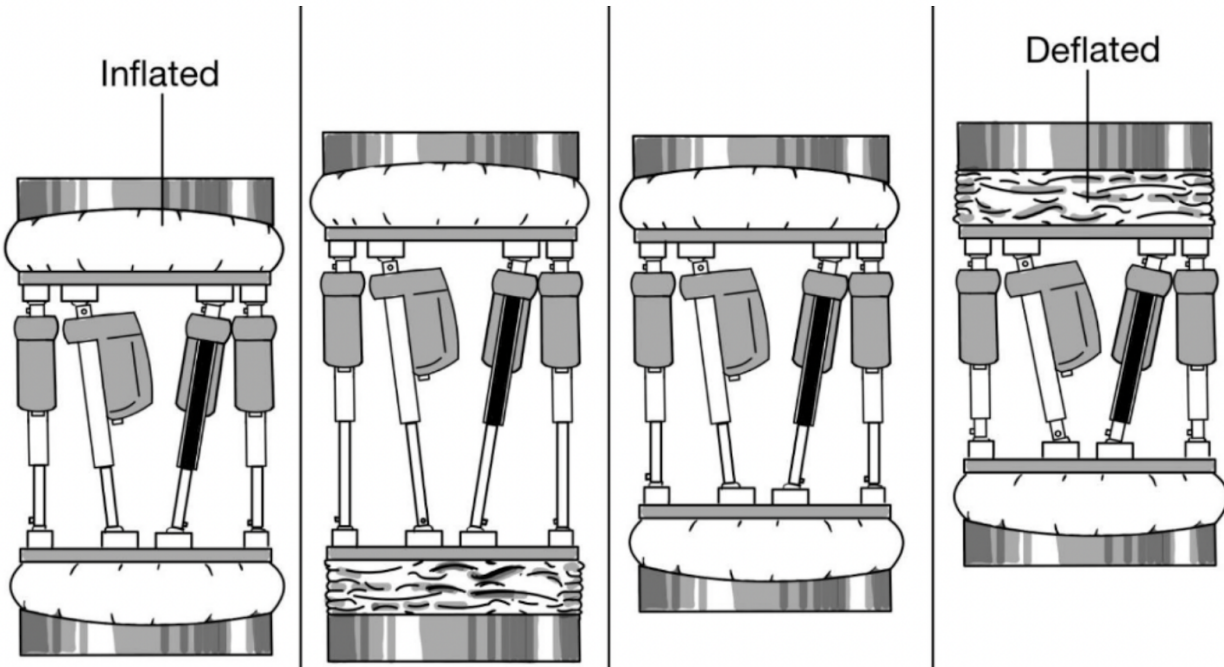


Fig. 80 Hexapod

2) *Controls*

The control software of the machine actuates each hexapod linear actuator individually, their control structures are identical but they are differentiated by pins and object definitions. Each actuator has hardware encoders that are used to read the current pose of each of the actuators in the hexapod. The software employs PID (Proportional-Integral-Derivative) controllers to reduce the position error in the software.

Control's sole concern is reaching a desired position acquired through Redis. Other data is indeed collected from the actuators which is critical information for calculating guidance points throughout the dig. Higher-level code will interpret these values and handle them as needed.

Despite the actuators requiring a velocity input for operation, the only available data is the current position. To address this, the system has three distinct structures for each actuator: an Encoder, a Position PID, and a Velocity PID. The Encoder is used to read the current extension of an actuator. The Position PID leverages this data, along with the desired actuator position, to calculate a target velocity. Subsequently, the Velocity PID takes this target velocity and the actuator's current velocity, computing the actual velocity at which the actuator should move. The controls then translate this calculated velocity into a tangible command for the motors, mapping the velocity to an analog value sent to the H-bridges. This process ensures that the actuators operate at a consistent rate, a critical feature for the digging process. Without the use of PIDs, actuators might lag, advance too quickly, or even stall, potentially leading to deformation of the Hexapod structure and consequent system failure. The PID controllers thus play a pivotal role in maintaining the integrity and functionality of the TBM's Hexapod system.

C. **Grippers**

1) Overview

The gripper system contains 6 bike inner tubes (3 front, 3 back) with 6 pneumatic valves and 6 pressure transducers for each to inflate and deflate the grippers. The behavior tree contains several nodes to have both manual and autonomous control over each gripper section. Autonomous nodes contain logic to deflate the front or back gripper only after the opposite gripper has inflated to prevent a fully deflated state. When in autonomous mode the grippers will alternate between front and back holds depending on the corresponding mode.

2) Controls

The gripper control consists of several Arduino C scripts that read and pressure transducer values which assist the behavior tree in progressing to different nodes. The above-ground pneumatic valves receive controls from the behavior tree and deflate or inflate based on the given directive. The desired PSI is sent to controls to allow for control of the degree to which the tires inflate or deflate.

D. **Excavation**

1) Overview

Control over the cutting head is necessary for safe and reliable machine operation. The motor controller link consists of a direct analog connection for write operations as well as a connection over the CAN bus for read operations. Using a PWM signal sent through an op-amp and low pass filter we can create an analog signal to adjust the voltage levels with a Teensy. Additionally, we will alternate the direction the cutting head spins to prevent a high degree of roll in either direction. Meanwhile, we will be utilizing the CAN bus on the excavation board to monitor all motor values to determine the status of the motor. All excavation operations will be verified autonomously before any push operations occur.

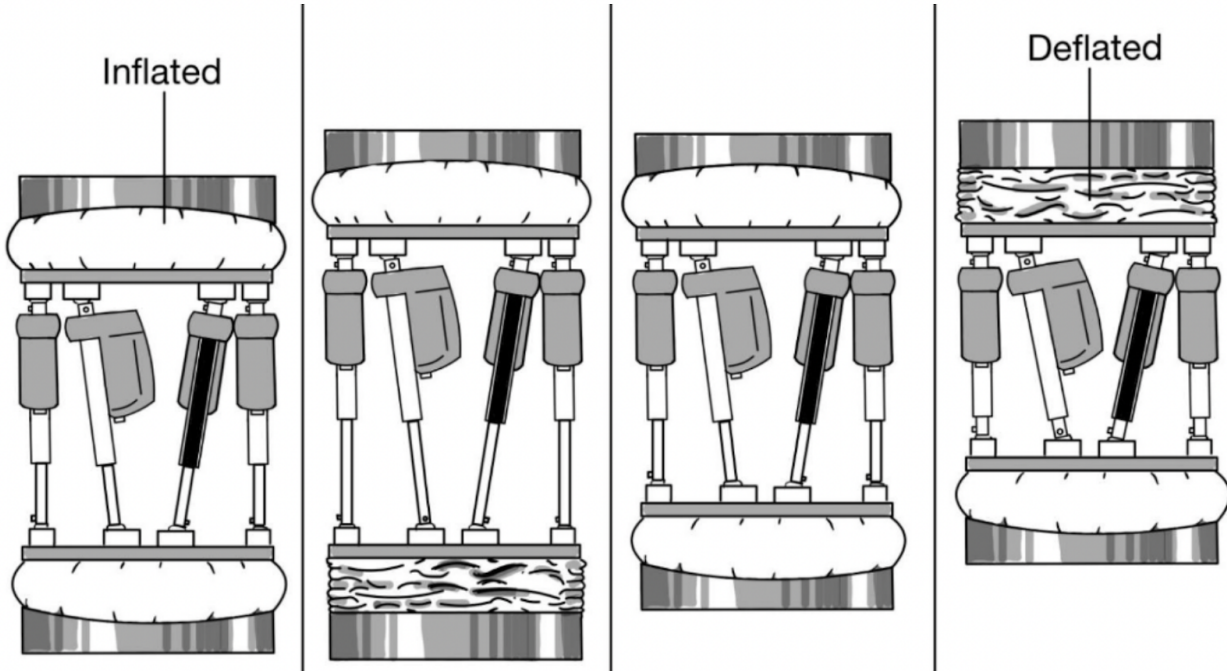


Fig. 81 Gripper Configuration

E. GUI

1) Overview

The purpose of the GUI is to provide a user-friendly interface that interacts with and displays the software system's status and performance. There are several features designed for usability and safety including buttons to change the mode between, idle, manual, or autonomous along with an operational estop button that is on every tab to ensure immediate access in case of emergency. The GUI includes a main page tab that displays all critical sensors, followed by tabs for each individual subsystem for a more focused view of that system. From the main page, users can quickly assess the overall health and status of the system. Another important feature is the interlocks tab which monitors all systems to ensure functionality within predefined error bounds. In the event of a component failure, the interlocks will send an estop command to halt the machine. In order to ensure the safety of the team, the GUI also includes indicators for quick feedback on whether or not the machine is safe to approach or if only designated persons should approach.

When we run the GUI, it will start up all the processes that we need to run separately. The GUI will open up the Main Tree, RIMU system, and our separate Tunnel Support tree. The GUI acts as a binding agent for all processes and presents each system's health.

2) Features / Tabs

- Tool Bar: The Toolbar is a stagnant feature of the GUI which holds the buttons controlling the mode of TBM, operational estop. It is always present at the bottom of the GUI no matter what tab you're on. It also includes frames for all data that will be commonly checked throughout the dig.
- Main Page: The GUI's main page is intended to provide a quick overview of the machine at a glance. By displaying all critical sensors which can quickly demarcate individual sensor statuses with colors.
- Grippers: The grippers page provides all necessary sensor values for the subsystem and states of the system, such as inflated or deflated. Additionally, users are provided with buttons to manually control the grippers



Fig. 82 GUI Toolbar

as well as set the desired pressure thresholds that are used to evaluate system success.

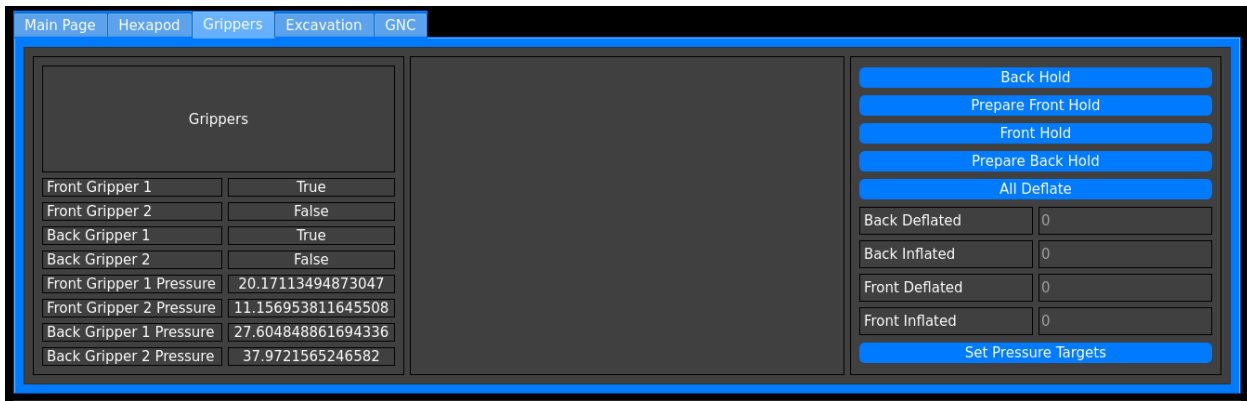


Fig. 83 GUI Grippers Tab

- Hexapod: The hexapod page displays all the sensors for the hexapod including the temperature, current, and actuator positions for each individual actuator. It also includes buttons to manually retract, push, test the actuators, and an input box to set the heave value in the event we need manual control.

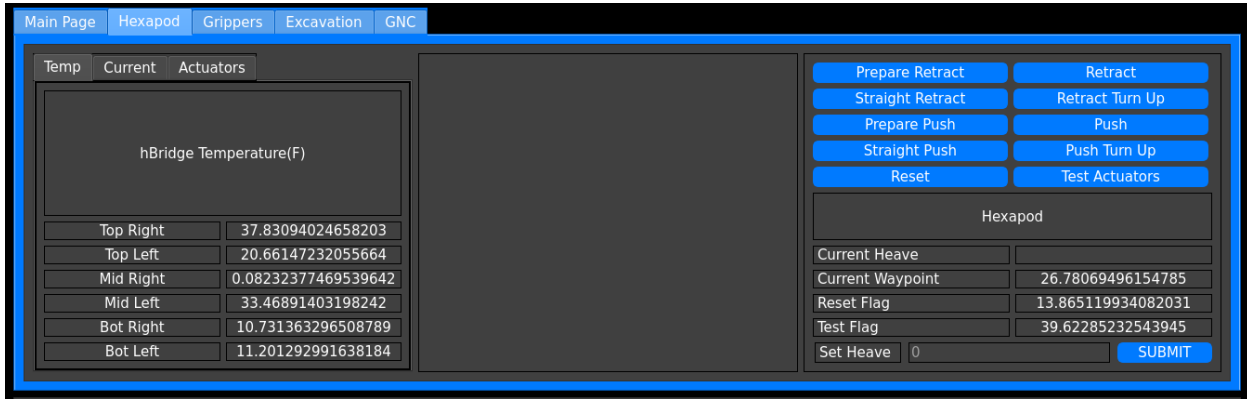


Fig. 84 GUI Hexapod Tab

- Excavation: The excavation page displays the RPM of the cutting head as well as buttons to turn the cutting head motor on or off. It also has input boxes for the target rotation, torque, min rotation, and max rotation to manually set RPM targets.
- GNC: The GNC tab displays all necessary values of the RIMU and other guidance measurements that are necessary to determine the health of the system. All sensor values from each IMU are also included in

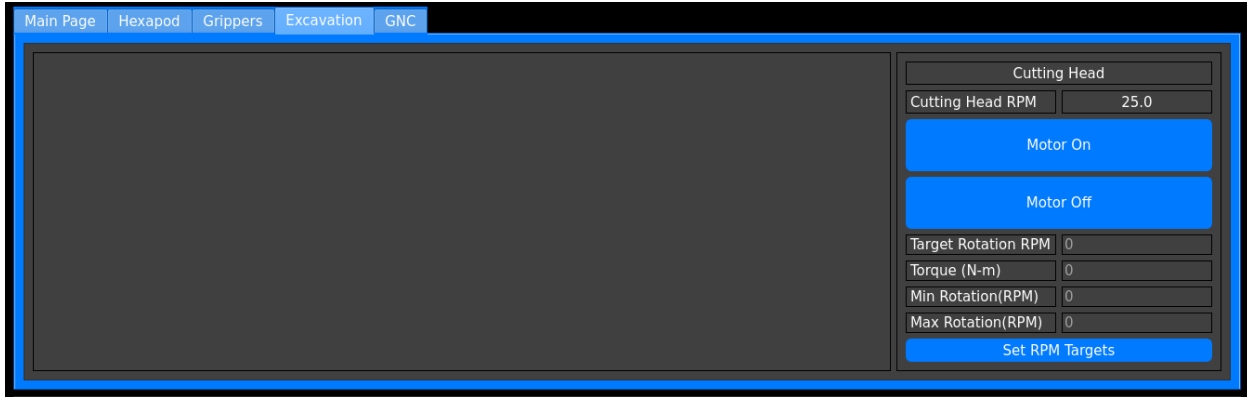


Fig. 85 GUI Excavation Tab

order to determine if the machine is moving in the desired direction.

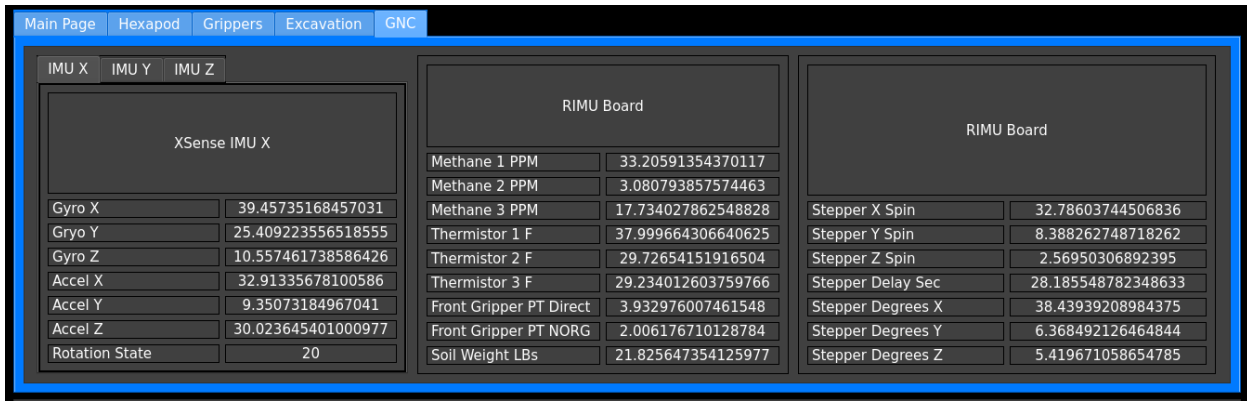


Fig. 86 GUI GNC Tab

- Separate Windows: Because of the many subsystems we also included the ability to separate all of the subsystem windows of the machine. This is especially helpful in allowing multiple subsystems access to their needed information without needing to switch back and forth between tabs.

3) GUI Backend

- Safe to Approach: It is not always clear whether the machine is safe to approach or not, so we take into consideration different sensor values. Considering the substantial power and speed of the cutting head we validate the cutting head is stagnant.. We also verify if the hexapod is moving, making sure that all the actuators are either at 0 or fully extended to the length at which they were set to extend. Another verification step is that Grippers are inflating at a steady pace, they do not have to be at 0, but we want to make sure they are not rapidly inflating or coming close to over-inflating. The final check is to make sure that the theta motor for tunnel support is not moving. All these together help us determine whether the machine is safe to approach or not.
- Manual: As mentioned previously, buttons are included in each subsystem tab for manual control. The manual control buttons allow us to take full control over the machine's processes, disregarding any checks that would occur in autonomous mode. When a button is pressed the corresponding variable is set to the desired value. This data can then be processed by the manual node which will execute any necessary actions that the GUI requests.

- Latency: Redis is known for its real-time speed, and we want to make sure that the GUI is keeping up with that speed and updating values as quickly as possible so that we are receiving the most accurate data without any delays. The most accurate and current data is very important for keeping up with things like safe to approach, interlocks, and whether or not the operational estop needs to be invoked. This also prevents any backlogging or buffer overflow that would occur when the data from Redis coming in is faster than the data shown.

4) Interlocks

The interlocks have a separate page for displaying once again the critical sensors list that helps us to see the health of the machine. One minor change is that when a critical sensor passes a low or high warning value that is outside of the bounds of safety, designated by either the mechanical or electrical team, the GUI will move that sensor into the interlock list and stop the machine. Additionally, communication loss with the machine causes the machine to estop, this is designated as a system being unresponsive for greater than 10 seconds. The interlock list will continue to monitor the values from the sensors and aid in quickly identifying the issue. On a case-to-case basis, these interlocks can be removed from the interlock list in order to continue operation.

F. Testing

1) *Grafana*

Telemetry GUI visualization of every sensor and control output for debugging purposes will be monitored through the usage of Prometheus in order to store metrics as a time series and Grafana to graph said times series. Information regarding the sensors, control output, minimum, maximum, warn, and units will be provided by the system's IO list which takes the form of a CSV file. Through a Prometheus server, each sensor and control output is assigned a gauge in which each metric will be stored and queried. Each gauge will be updated with its corresponding metric at a rate of 1 Hz. The gauges will be queried through Grafana at a rate of 1 Hz and will be visualized through value over-time graphs. Graphs are organized by system, allowing the user to easily compare metrics with other relevant metrics for debugging purposes. If a metric falls within the warning range, an alert will be displayed at the top of the dashboard for the specific metric and the time of the warning will be marked on the graph.

2) *Pytests*

All unit tests and basic system functionality will be performed using pytests. Because of the use of Behavior trees, we are easily able to generate testing harnesses for specific nodes of the tree by adding or removing other nodes as needed.

3) *Flat Set*

In addition to software testing, we will also be using a flat set to perform hardware-in-the-loop testing. We will continuously test all functionality of the entire software system to find any oversights in the system. By doing this we will greatly reduce integration time and allow for more time for full system tests.

G. Mqtt Broker

The requested navigation telemetry will be provided to The Boring Company through the MQTT broker provided during the competition. Said navigation telemetry will be calculated from the sensor values from the guidance, navigation, and control systems and will be stored in a JSON file formatted as specified by the rules and requirements document. The JSON will be updated with the relevant metrics and be published to our team's specific topic at a rate of 1 hz.

H. Tunnel Support

Most of the machine's control is managed through behavior tree processes, embedded systems programming, and simple PID controllers. However, the Tunnel Support system presents a more complex control challenge that requires a dedicated approach. In the following sections, we will explore the derivation and development process, present simulations, and analyze results to prepare for the system's integration onto the machine.

1. Overview

As discussed in the Tunnel Support (TS) section of this document, our printing method utilizes a three-axis RZT mechatronics system that will need accurate control capabilities to reliably carry out its necessary tasks. The TS section needs to be able to adapt and react to possible debris obstacles that breach the walled rear of the TBM. As such the tunnel support system will contain its own Behavior Tree to optimize reactivity with a few nodes in the main tree to coordinate segment ejection.

The relationship between the TBM's motion and TS control is also important in considering subsystem interaction. More specifically, our Hexapod push/retract cycles depend directly upon the states of our three axes of control.

Further, it is worth noting that although our primary axis of control (theta) is the only axis we've included with its state space derivation/analysis, a similar analysis would be applied to the other two axes, but with a simpler model as their motion is linear.

2. Hexapod Reliance

At a macroscopic scale, the accuracy of our TS commanding is of great importance as natural error accumulates throughout the TBM's dig and compounds with other subsystem discrepancies.

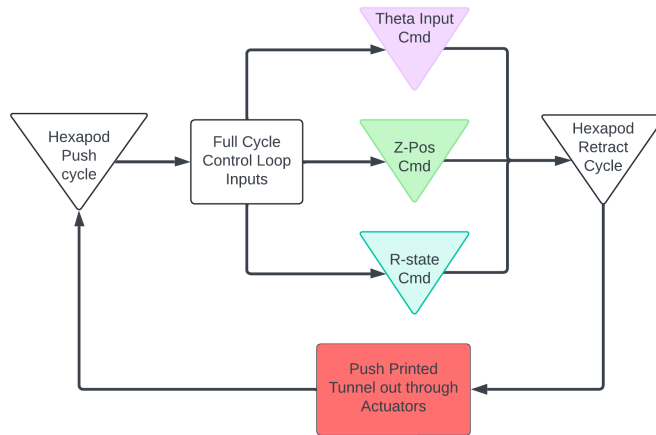


Fig. 87 TS-Hexapod Interface

Fig. 87 illustrates the inherited reliance of the TBM hexapod motion on each command sent to each axis of control. The colors and symbols used in this diagram represent different processes and where they are contributing to the system. Fig. 88 highlights the key differences in syntax and can be used for reference in the following sections.

3. Control Design Overview

Simplified for clarity, Fig. 89 depicts the entire system control architecture for tunnel support, with three distinct sections that all need separate commanding loops. The upper left section commands the TBM theta-axis, the lower left section commands the TBM z-axis and the rightmost section commands the TBM r-axis. The next three subsections of this section describe the feedback control loops for each axis in greater detail.

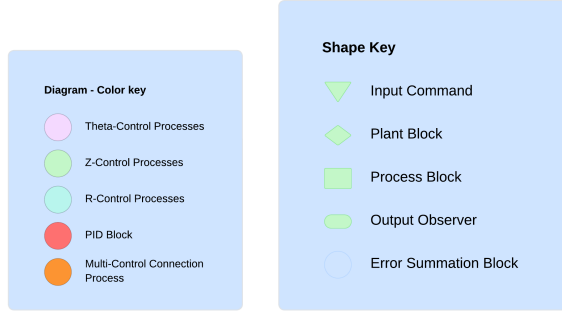


Fig. 88 FBD Legend

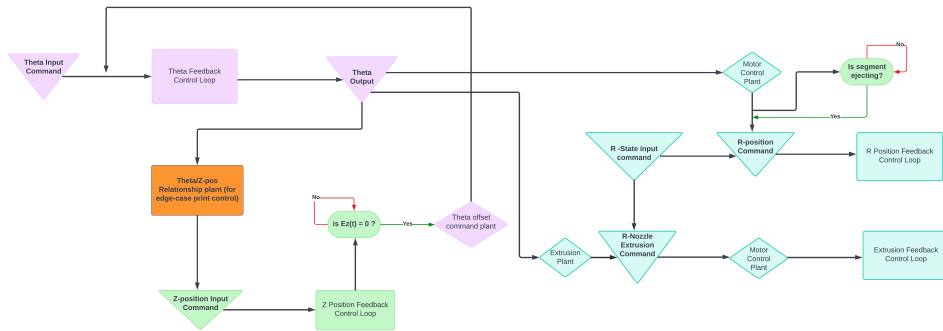


Fig. 89 Simplified Full FBD

Theta-Axis The theta-axis is directly related to the other subsequent sections, and thus, both z and r axes rely on outputs from theta-axis as inputs for their own loops. Referencing Fig. 90, the first signal is a theta input command that feeds into a summation block along with the theta output at the current timestep. The output of the summation block is therefore a theta error function that feeds into a position controller. This output is then sent to both the r-axis section (which is examined further in the following sections) and to an omega plant so that the data the theta velocity controller receives is converted from $\frac{\text{rad}}{\text{s}}$ to $\frac{\text{m}}{\text{s}}$.

Also, the omega plant contains the relation:

$$\omega_{stepper} = (22.225)\omega_{control} \quad (33)$$

where 22.225 represents the necessary gear ratio coefficient for adequate torque accommodations (as discussed in the TS section of this document).

Following this plant, the velocity controller output is sent to a nested feedback loop with motor encoder/limit switch data to be used for calculating real-time theta location. As previously mentioned, the output of this feedback loop is sent into the theta input summation block, as well as to a multi-control connection process block.

This process block relates theta and z position and outputs to a summation block as the z-position input command for the z-axis section. It is included to account for possible debris obstacles that breach the TBM internally and will allow for further design flexibility since we will be able to interrupt the nominal dig process and, once the debris is cleared, continue as desired.

Note that the position and velocity controller designs in Fig. 90 are more detailed in the following sections.

Z-Axis Similar to the theta section, the summation block for the z-axis section sums the inputs from the theta-z relationship plant, z-position input command, and z-position output at the current timestep in order to output a z-position error function (as seen in Fig. 91).

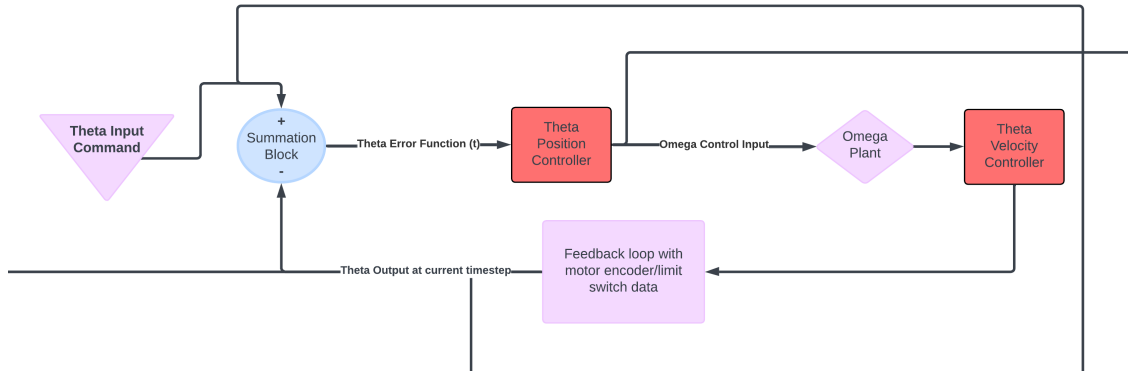


Fig. 90 Theta Axis Control Architecture

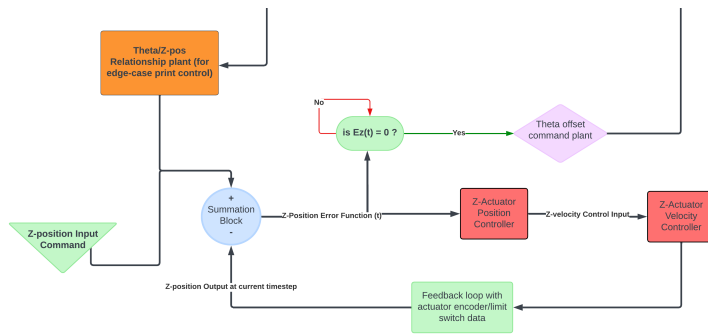


Fig. 91 Z-axis Control Architecture

Since our design is focused on printing shells without a linear closure seam, we need a means of offsetting our initial theta reference point every print cycle. The best design for our cylindrical print structure, in terms of structural integrity, is one that incorporates a random seam closure pattern. Thus, for our theta offset command plant, we will use a pseudo-random number generator to choose a theta value between the set bounds of 0° and 180° to be included back into the theta loop. In this case, "pseudo" implies the number generator will not repeat any theta values for consecutive print cycles.

If the z-position error function is not equal to zero, then nothing will be sent to theta offset command plant. If the error function is equal to zero, its output is received by the aforementioned command plant and subsequently added to the theta input command before summation in the theta-axis section.

Regardless, the z-position error function will also be sent through a position and velocity controller for the corresponding z-actuators. As in the theta section, the velocity controller output is then sent into a nested feedback loop with actuator data to estimate the position of the actuator at the current timestep.

R-Axis The control design for the r-axis is slightly more complex than the two previous sections, but the overall architecture is the same. For accuracy, the r section is split into two subsections labeled as position and nozzle extrusion.

Each subsection receives a corresponding external input from the theta loop: the omega control input as an input to an extrusion plant and the theta output at the current timestep as an input to a motor control plant for the actuator.

This actuator plant is responsible for determining the actuator position based on the current timestep of theta. An output observer is placed at this plant's output to check whether or not a printed PLA section is being ejected. If there's no segment ejection occurring the actuator will stay fixed at its nominal printing length. If segment ejection is occurring the actuator will need to retract in order to move the nylon ball transfer bearing (as discussed in the TS section of this document) free of the print section ejection path. In other words, control of the r-actuator is only necessary during segment ejection.

This FBD only shows the interactions within the TS system itself and does not include detailed external data

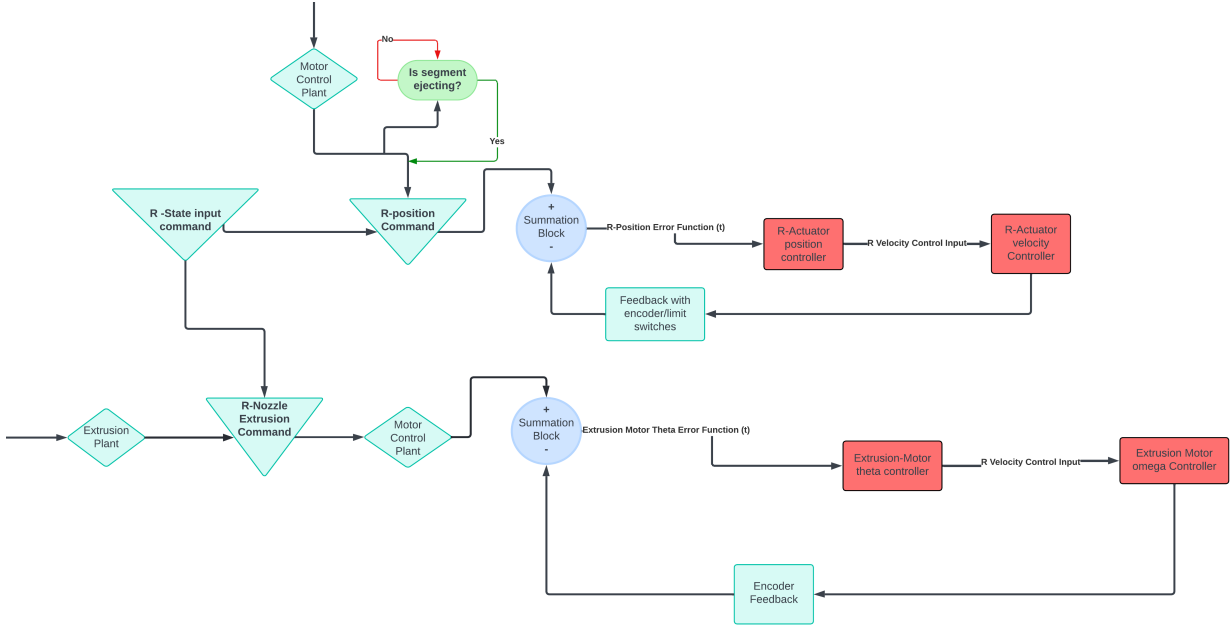


Fig. 92 R-axis Control Architecture

pathways connected to other subsystems like the Hexapod push/retract cycle discussed earlier. With that in mind, the output observer for this section represents more than a boolean observation cycle. It represents the connection between the Hexapod and r-actuator, where the Hexapod system will communicate when it's extended to its critical length (or 8in).

The design in Fig. 92 shows that the combination of these inputs from the theta section with an r-state input command is a necessary step before finding our error functions for each subsection loop.

For the actuator, the r-position value is sent to a summation block, which outputs a position error function. As in the main z loop, the position error function is passed to a position controller and a velocity controller for the r-actuator. These controllers will have a similar structure to the ones from the z-section actuator. Again, they output to a nested feedback loop containing encoder/limit switch data whose output is sent to the summation block.

A similar process for the extrusion rate is used only this loop is active throughout the entire dig duration, the nozzle extrusion command is fed through a motor control plant prior to being summed, and it receives a different external input from the theta section. This theta position input feeds directly to an extrusion plant that contains the following relationship

$$\dot{m}_{extrusion} [g/s] = \frac{(4.535[g/rad])(\omega_{control}[rad/s])}{1} \quad (34)$$

between the extrusion rate of the nozzle and the angular velocity control input for the motor. This plant's ω output is then summed in the corresponding summation block. The extrusion motor theta error function output from the summation block is sent to a theta controller that gives a velocity control input to an omega controller. After feeding through a similar feedback loop containing encoder data, the summation block then receives the extrusion output at the current timestep.

4. Theta Axis Simulation and Tuning

Our Theta-Axis is the primary axis of control, hence the need to delve deeply in the derivations of the control system. The control loop for the tunnel support system utilizes a dual PID control loop, as shown in Figure 93. This loop is a velocity control system, as the primary output from this system is the velocity ($\dot{\theta}$) which will be fed into the θ motor.

The transfer function for this loop is given in Equation 35:

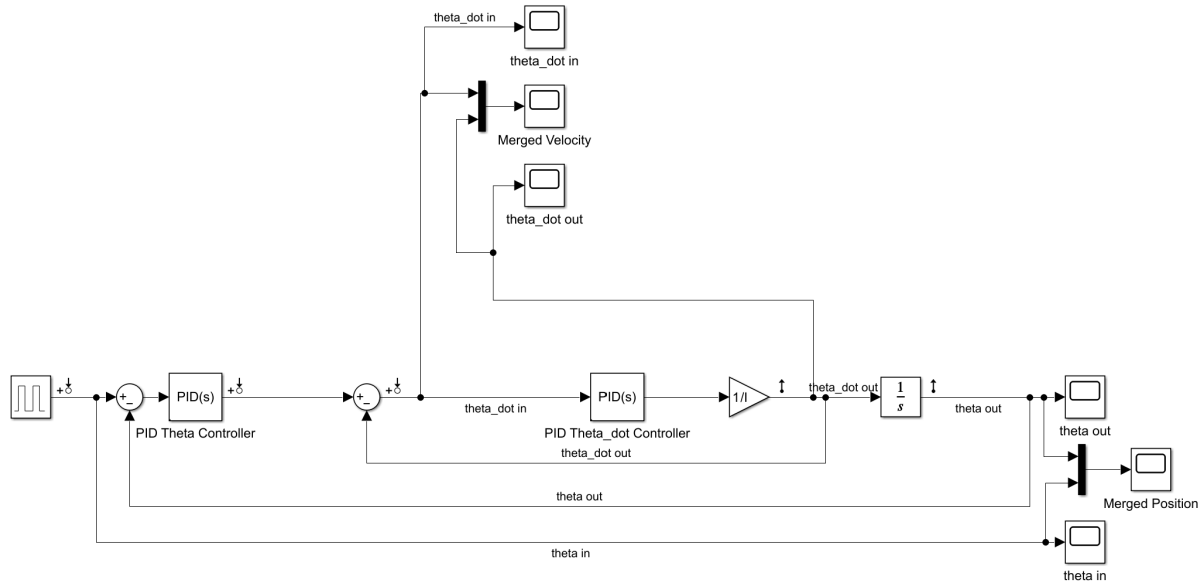


Fig. 93 The block diagram of the system. Note theta dot out and theta out, which are the velocity and position outputs.

$$G(s) = - \left(\frac{s^3 (k_{1D}k_{2I} + k_{2D}k_{1I} + k_{1P}k_{2P} + k_{1D}k_{2D}s^2)}{\Omega} \right) - \left(\frac{s^3 \left(\frac{k_{1I}k_{2I}}{s^2} + \frac{k_{1I}k_{2P}}{s} + \frac{k_{2I}k_{1P}}{s} + k_{1D}k_{2Ps} + k_{2D}k_{1Ps} \right)}{\Omega} \right) \quad (35)$$

where

$$\Omega = k_{1I}k_{2I} - Is^4 + k_{2D}s^4 + k_{2Is}^2 + k_{2Ps}^3 + k_{1D}k_{2Ds}^4 + k_{1D}k_{2Is}^2 + k_{2D}k_{1Is}^2 + k_{1D}k_{2Ps}^3 + k_{2D}k_{1Ps}^3 + k_{1P}k_{2Ps}^2 + k_{1I}k_{2Ps} + k_{2I}k_{1Ps} \quad (36)$$

This transfer function was derived from the state space model:

$$\begin{aligned} \dot{\mathbf{x}} &= \begin{bmatrix} 0 & 1 \\ \frac{-\eta}{I} & \frac{-\sigma}{I} \end{bmatrix} \mathbf{x} + \begin{bmatrix} 0 \\ \frac{\nu}{I} \end{bmatrix} \mathbf{u}, \\ \dot{\mathbf{y}} &= \begin{bmatrix} 0 \\ 1 \end{bmatrix} \mathbf{x} + \begin{bmatrix} 0 \\ 0 \end{bmatrix} \mathbf{u} \end{aligned}$$

where

$$\eta = - \left(k_{1D}k_{2I} + k_{2D}k_{1I} + k_{1P}k_{2P} + k_{1D}k_{2Ds}^2 + \frac{k_{1I}k_{2I}}{s^2} + \frac{k_{1I}k_{2P}}{s} + \frac{k_{2I}k_{1P}}{s} + k_{1D}k_{2Ps} + k_{2D}k_{1Ps} \right),$$

$$v = k_{1D}k_{2I} + k_{2D}k_{1I} + k_{1P}k_{2P} + k_{1D}k_{2Ds}^2 + \frac{k_{1I}k_{2I}}{s^2} + \frac{k_{1I}k_{2P}}{s} + \frac{k_{2I}k_{1P}}{s} + k_{1D}k_{2Ps} + k_{2D}k_{1Ps},$$

$$\sigma = - \left(k_{2P} + k_{2Ds} + \frac{k_{2I}}{s} \right)$$

and I is the system inertia. Note that while this specific loop has been developed for control of θ , by altering the inertia value, it can control any velocity-position style system with similar dynamics.

Using these equations, the transfer function can be found with the equation:

$$G(s) = \mathbf{C}(s\mathbf{I} - \mathbf{A})^{-1} \cdot \mathbf{B} + \mathbf{D}$$

where \mathbf{I} is a 2×2 identity matrix.

Control System Simulation To test the feasibility of this control system, we will first implement the simplified control solution as derived below. This approach focuses on attaching proportional constants to each element of our state, allowing us to evaluate system performance with reduced complexity. Should we observe errors or instabilities that cannot be mitigated with this simplified solution, we will transition back to the fully derived PID loop applied to each element of the state. This will enable us to handle a broader range of potential disturbances and modeling inaccuracies. Our simplified control law becomes

$$\begin{aligned} \tau &= I\ddot{\theta} = k_1(k_2(\theta_i - \theta) - \dot{\theta}) \\ \ddot{\theta} &= \frac{1}{I}(k_1(k_2(\theta_i - \theta) - \dot{\theta})) \end{aligned}$$

Thus our state-space representation of this simplified control system becomes

$$\begin{bmatrix} \dot{\theta} \\ \ddot{\theta} \end{bmatrix} = \begin{bmatrix} 0 & 1 \\ -\frac{k_1 k_2}{I} & -\frac{k_1}{I} \end{bmatrix} \begin{bmatrix} \theta \\ \dot{\theta} \end{bmatrix} + \begin{bmatrix} 0 \\ \frac{k_1 k_2}{I} \end{bmatrix} \begin{bmatrix} \theta_i \end{bmatrix}$$

Where θ_i is the control input into this system, and $\dot{\theta}$ is the signal input that we will be sending to our motors.

To determine the appropriate values for the constants k_1 and k_2 in our simplified control system, we use root-locus analysis. The root-locus plot is a graphical method that helps us visualize how the poles of the closed-loop system change with variations in the gain constants, allowing us to assess system stability and responsiveness.

In this simplified system, the root-locus plot provides insight into how different values of k_1 and k_2 impact the system's natural frequency and damping ratio, which are key parameters for achieving the desired transient response and also determine the stability of a solution space. By plotting the system's poles in the complex plane as we vary these constants, we can identify values for k_1 and k_2 that portray characteristics necessary for our system.

We first derive the initial estimate for k_1 and k_2 by expanding our control law to match the standard form

$$\begin{aligned} \ddot{\theta}(t) + 2\zeta\omega_n\dot{\theta}(t) + \omega_n^2\theta(t) &= \omega_n^2\theta_i n(t) \\ \ddot{\theta}(t) - \frac{k_1}{I}\dot{\theta}(t) - \frac{k_1 k_2}{I}\theta(t) & \end{aligned}$$

To determine k_1 and k_2 , we first define the desired initial estimate of damping coefficient, ζ , as 2, setting the system to be over-damped. Next, we calculate the natural frequency, ω_n , based on the desired period of oscillations between prints, T , of the system, with $\omega_n = \frac{2\pi}{T}$. With these values established, k_1 is then calculated as $k_1 = 2\zeta\omega_n I$, while k_2 is determined by $k_2 = \omega_n^2 I$. This approach aligns the system's dynamics with the desired second-order behavior, approaching a good starting point for the root-locus analysis. By choosing $\zeta = 2$ and selecting ω_n according to the target response characteristics, we ensure efficient stabilization within the designed time frame. This gives us initial gains of

$$k_1 = 31.6152$$

$$k_2 = 56.2254$$

To simulate our θ axis, we have selected a custom input signal for our theta axis, as seen in Fig 94a, to test along with the normal square-wave pictured in Fig 94b. This *Sine-Stop* wave is a sinusoidal function that pauses for 0.2 seconds to simulate the rotation signal we would be sending into our motors. The pause is designed to exist to give our motors time to stabilize before continuing to the reverse-direction printing phase.

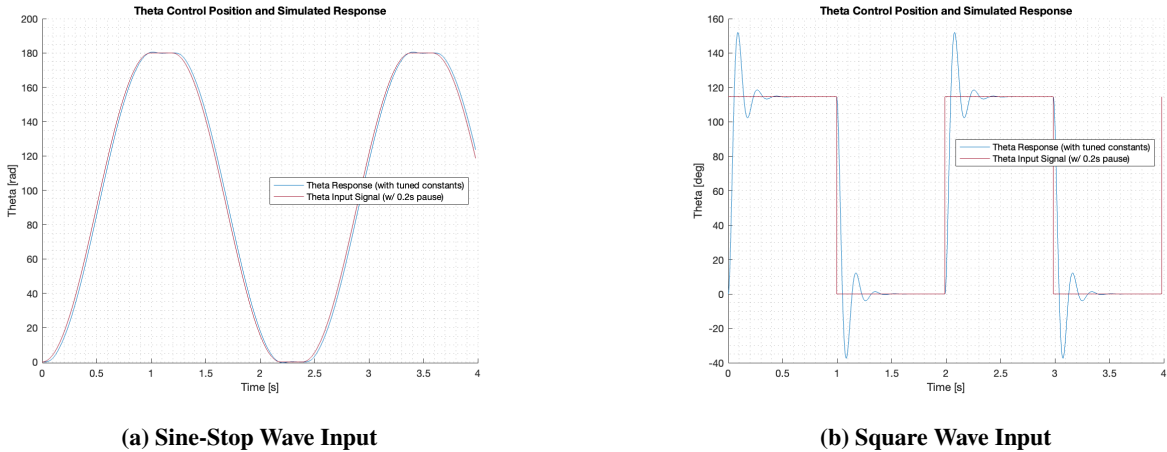
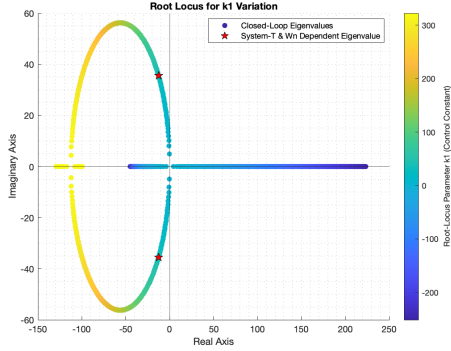


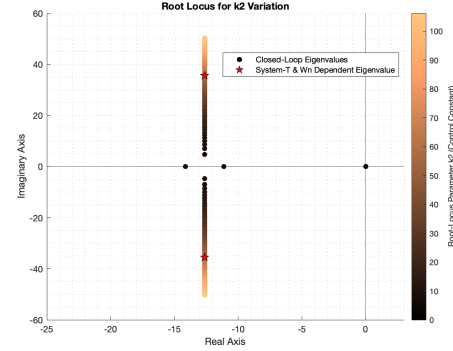
Fig. 94 Untuned Input Vs. Response

Responses for both an expected input into our theta-control axis and a square wave are shown in Fig 94. The initial response already seems very accurate. However, the precise control constraints on the θ axis make this initial estimate not good enough as there is a consistent 3° error with the k_1 and k_2 we have derived earlier.

From here, we can perform a root-locus analysis to fine-tune each gain by parameterizing one constant while keeping the other fixed. A range of values around the initial estimates of k_1 and k_2 is tested to observe how the poles of the closed-loop system move across the complex plane as each gain is varied. For each gain, a vector of values is constructed symmetrically around the initial gain estimate. By examining these variations, we assess system stability and response characteristics.



(a) Parameter: k_1 , Constraint: k_2



(b) Parameter: k_2 , Constraint: k_1

Fig. 95 Root-Locus Eigenvalue Analysis

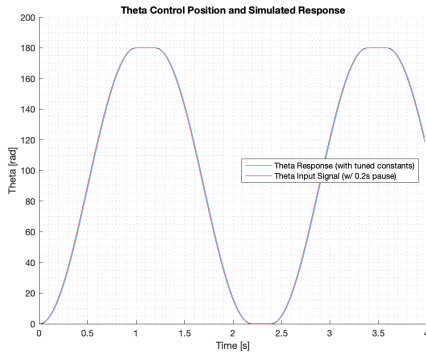
For k_1 , we generate a series of values centered on the initial estimate and increment or decrement by a fixed step. For each of these values, we compute the system's state matrix with k_2 held constant. The eigenvalues of this matrix reveal the locations of the poles, which we track as k_1 is varied. The resulting root-locus plot as can be referenced in Fig 95a for k_1 shows how the system's damping and natural frequency change, giving insight into the effect of k_1 on system stability and transient response. We can see that the system becomes more damped as we increase k_1 , and surprisingly, that the amplitude of oscillations decreases as $k_1 > \sim 150$ or when $\sigma < \sim -55$. However, these eigenvalues start to approach instability when $k_1 > \sim 316$.

Similarly, we create a range of values for k_2 , centered on its initial estimate. With k_1 fixed, we compute the state matrix for each value in this range and find the corresponding eigenvalues, which represent the system poles. Tracking these poles on the root-locus plot tells us that lower k_2 gains lead to instability while higher gains lead to lower damping coefficients. While initially, it might seem more reasonable to approach the lowest possible gain on the vertical line, this would increase the inherent damping coefficient in our system which will slow our system down. The oscillations have already been damped through tuning k_1 , and as such, we should focus on increasing the value of k_2 as much as possible to lower the damping of our system and increase the responsiveness to control. Through multiple simulations and verification via Monte Carlo, we can approximate our gains to be:

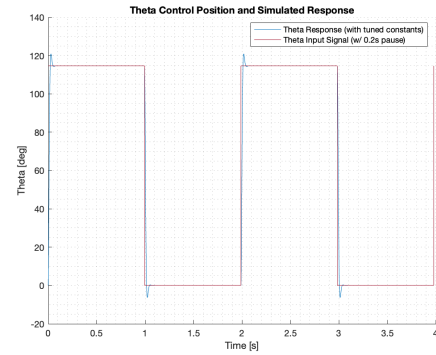
$$k_1 = 300$$

$$k_2 = 110$$

With these newly derived gains, we can rerun the simulation and see the effects of our root-locus tuning method



(a) Sine-Stop Input vs. Response



(b) Square Wave Input: θ

Fig. 96 Simulation with Tuned Gains

As shown through the root-locus analysis, in Fig 96 we have reduced the error between our simulated θ response and θ input to less than approximately 1° . The simulated response also shows an overshoot of 0.012° , which is within the accuracy requirements of the tunnel support system. Observing the Fig 96b, we can see that we have drastically damped the oscillations while also decreasing the settling time for the system.

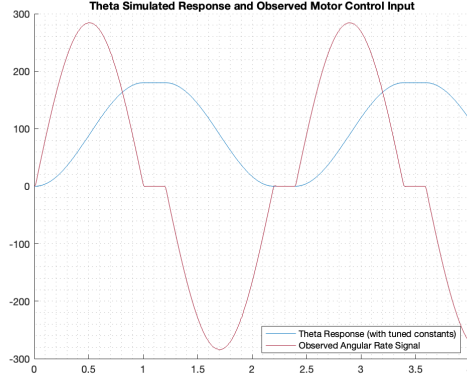


Fig. 97 Observed $\dot{\theta}$ Motor Input

Observing the *angular rate signal* in Fig 97, we see that the expected control input for the velocity-controlled motors aligns with the capabilities of motors rated for the torque and speed demands of the Tunnel-Support system.

We plan to implement this Python-based control mechanism and perform live testing with the θ -axis motors, which will be controlled through a combination of embedded C and our message broker system, Redis. This process provides substantial confidence in the design of the θ -control system. However, we recognize that physical motor dynamics may differ from our Python-based simulations. As such, the control gains will be re-evaluated and adjusted progressively as the physical system assembly advances.

XIII. GNC System

In the following section, we will provide an in-depth exploration of the Guidance, Navigation, and Controls (Software Sub-system) for CU-Hyperloop's Autonomous Tunnel Boring Machine.

A. Guidance

1. Dig Path

A complete guidance system needs beacon points to aim towards during its run-time. We have implemented the same system from the previous two years to accomplish this task. For real-time trajectory planning and control, we'll utilize a series of pre-planned CSV points. These points serve as continuous reference markers, enabling our system to simulate and dynamically adjust the dig path to maintain alignment with our projected course. This CSV-based framework ensures a responsive trajectory planner, capable of adapting to in-tunnel variations and maintaining the desired path throughout the operation.

2. Trajectory Planner

The Look Ahead Path Finding Algorithm (LAPFA) is a point-pursuit algorithm designed to guide the Tunnel Boring Machine (TBM) along an intended path or correct deviations due to environmental factors. LAPFA uses six state inputs—current X , Y , Z , Roll, Pitch, and Yaw—from the Unscented Kalman Filter (UKF) to calculate the next best point on the path that the TBM should aim toward. This approach allows LAPFA to dynamically adapt to changes in the TBM's position and orientation, ensuring that it stays aligned with the dig path.

To assess proximity to each point on the path, LAPFA computes the Euclidean distance D_1 between the TBM's current position and each path point:

$$D_1 = \left\| \begin{bmatrix} X_0 \\ Y_0 \\ Z_0 \end{bmatrix} - \begin{bmatrix} X_{\text{PATH}} \\ Y_{\text{PATH}} \\ Z_{\text{PATH}} \end{bmatrix} \right\|_2$$

where D_1 is the L2 norm of the vector between the current position and the path point. This distance metric helps LAPFA determine the TBM's proximity to each path point, ensuring that the machine remains within a reasonable distance of the path.

In addition to distance, LAPFA calculates the pitch and yaw angles required to reach each path point, defined as:

$$\theta_1 = \arcsin\left(\frac{Z_{\text{PATH}} - Z_0}{D_1}\right), \quad \psi_1 = \arcsin\left(\frac{Y_{\text{PATH}} - Y_0}{D_1}\right)$$

These angles, θ_1 (pitch) and ψ_1 (yaw), represent the necessary orientation adjustments for the TBM to align with each point. Each path point is checked to ensure that the deviations in θ and ψ do not exceed the maximum turn angle α_{MAX} , and that D_1 remains within the maximum allowable push distance Δ_{MAX} . Points meeting these criteria are added to an array P of potential next steps.

To determine the optimal point to pursue, LAPFA employs a Hyper-Exponential Regression function to assign a "weight" or score to each point based on its suitability for guiding the TBM. This scoring system is designed to balance proximity to the TBM and alignment with the overall trajectory of the dig path. The regression function $F(x)$ is defined as:

$$F(x) = (1 - B(x))f(x) + B(x)L(x)$$

where $f(x)$ and $L(x)$ are two functions representing different scoring priorities:

- $f(x)$ is a right-skewed Gaussian function that assigns higher scores to points closer to the TBM. It is defined using the standard normal probability density function $\phi(x)$ and the cumulative distribution $P(x)$ as follows:

$$f(x) = k \cdot \phi\left(\frac{x - l}{w}\right) \cdot P\left(a \cdot \frac{x - l}{w}\right)$$

where the standard normal probability density function $\phi(x)$ and the cumulative distribution function $P(x)$ are given by:

$$\phi(x) = \frac{1}{\sqrt{2\pi}} e^{-\frac{x^2}{2}}$$

$$P(x) = \int_{-\infty}^x \phi(t) dt$$

and the parameters in $f(x)$ were tuned to $k = 2.8$, $l = 0.1$, and $w = 0.2$ to control the height, location, and skew of the distribution. This function prioritizes points near the TBM, especially when x (orthogonal distance to the path) is small.

- $L(x)$ is a logistic function that provides higher scores for points further along the path, encouraging alignment with the path's overall direction. It is defined as:

$$L(x) = \frac{1}{1 + \exp(-t(x - q))}$$

where t and q were tuned to $t = 7$ and $q = 1.4$, controlling the steepness of the curve and the location of the inflection point. This component becomes more influential for larger values of x , drawing the TBM toward points that support long-term alignment.

The blending function $B(x)$ enables a smooth transition between $f(x)$ and $L(x)$ based on the value of x relative to a threshold x_i . It is defined as:

$$B(x) = \frac{1}{2} \left(1 + \tanh\left(\frac{x - x_i}{r_t}\right) \right) \cdot \left(1 - \exp\left(-\frac{(x - x_i)}{r_r}\right) \right)$$

where the parameters were tuned to $x_i = 0.7$, $r_t = 0.1$, and $r_r = 0.1$ to control the smoothness of the transition and the influence of the exponential component. These values ensure that the function smoothly shifts emphasis between $f(x)$ and $L(x)$ as x increases, allowing for a dynamic balance between proximity and alignment.

Each point on the path receives a score based on this Hyper-Exponential Regression function, with the highest-scoring point representing the ideal target for the TBM to pursue. This approach enables LAPFA to continuously adjust its path selection based on real-time conditions, maintaining an optimal approach and alignment with the dig path.

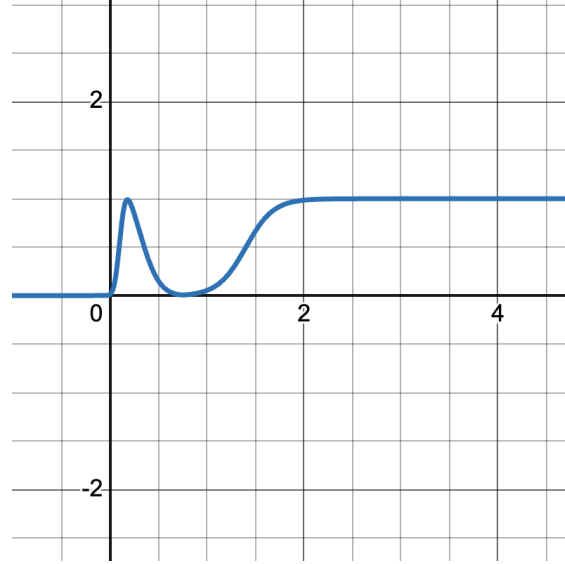


Fig. 98 Hyper-Exponential Regression Function $F(x)$ for Point Selection in LAPFA

Finally, the updated positions and orientations for the TBM are calculated as:

$$\begin{aligned} X_{\text{New}} &= X_0 + \Delta_{\text{MAX}} \cos(\theta_1), & Y_{\text{New}} &= Y_0 + \Delta_{\text{MAX}} \sin(\psi_1), & Z_{\text{New}} &= Z_0 + \Delta_{\text{MAX}} \sin(\theta_1) \\ \theta_{\text{New}} &= \theta_1, & \psi_{\text{New}} &= \psi_1, & \phi_{\text{New}} &= \phi_0 \end{aligned}$$

This systematic approach enables efficient path correction and alignment, as demonstrated in previous implementations. LAPFA's ability to dynamically select optimal path points allows the TBM to navigate its environment effectively, minimizing overshoot and maintaining the desired trajectory.

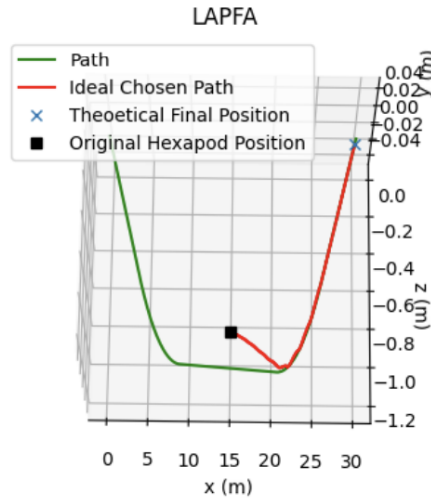


Fig. 99 Illustration of LAPFA Trajectory Correction

B. Navigation

As a standard for navigation, we define the *Inertial Frame* as the classic Newtonian non-accelerating reference frame, usually classified in *NED*, and the *Body Frame* as the accelerating frame placed at the center of mass of the TBM.

The following Sections outline *Sensors and Supporting Systems*:

1. Inclinometers

The inclinometer sensor system consists of three inclinometers in the front section of the TBM to measure tilt in all three axes, and three dual-axis inclinometers in the rear to verify position. If the single-axis front inclinometers fail, they can be replaced with dual-axis inclinometers. The tilt measured by the inclinometers provides the TBM's rotation, and combined with the push distance, allows for attitude estimate. This estimate is then incorporated into our sensor-fusing state estimator (UKF).

If the IMU system fails or becomes unreliable, the inclinometer system will take over attitude estimation, with measurement noise covariance R within the UKF being adjusted accordingly. The system operates by comparing the TBM's pre-push and post-push attitudes, deriving the current attitude. With the push length, calculated via inverse kinematics, it provides an updated state estimate, which is fed into the UKF along with IMU data. The system uses Direction-Cosine-Matrices derived from NASA-standard 3 – 2 – 1 Rotation Matrices and measured 3 – 2 – 1 Euler angles to estimate the TBM's state in the inertial frame. Although 3 – 2 – 1 Rotation Matrices and their derivatives are singular when $\theta = \pm\pi$, the TBM will never encounter situations where it is pitched completely vertically.

The inclinometer system is designed as a redundant system due to the potential failures and lack of in-ground testing of the IMU System in full-dig environments. Unlike IMU gyroscopes, inclinometers provide stable, comparatively drift-less measurements. Their calculations for determining TBM state are also simpler than those required for the IMU System's stochastic estimation filters.

2. Inertial Measurement Units

The main navigation sensors on the TBM from the previous year are a set of three Xsens MTi-3 AHRS 9-DOF IMUs. We have been using this set of three orthogonally mounted IMUs connected to a Teensy 4.0 microcontroller, communicating via I2C, to test the robustness of our navigation system.

We have since decided to transition from the MTi-3 sensors to a set of VectorNav VN-100 IMUs, which offer enhanced noise mitigation capabilities and improved accuracy. Alongside this hardware upgrade, we have implemented several new protocols to optimize the system, including the Rotational Inertial Measurement Unit (RIMU) used in last year's competition cycle. These protocols will be discussed in more detail below.

In the current implementation where we are testing our algorithms, we use a set of filters on our set of MTi-3s; a combination of a high-pass filter on our gyroscopes and a low-pass filter on our accelerometers. Below is the derivation for implementing these filters in discrete form.

A low-pass filter allows low-frequency signals from accelerometers to pass while attenuating high-frequency noise. The continuous-time form of a first-order low-pass filter is given by:

$$y(t) = \frac{1}{\tau s + 1} \cdot x(t)$$

where:

- $y(t)$ is the output,
- $x(t)$ is the input signal,
- τ is the time constant, and
- s is the Laplace variable.

To set a valid cutoff frequency f_c for this filter, we can relate it to the time constant τ at the -3 dB point as follows:

$$\tau = \frac{1}{2\pi f_c}$$

The cutoff frequency f_c can then be experimentally determined, for example, by conducting a long static test to identify the frequency where the amplitude response drops by -3 dB.

To discretize this filter, we use the backward Euler approximation for s

$$s \approx \frac{1 - z^{-1}}{T}$$

where T is the sampling period, and z^{-1} represents a one-step delay in discrete time.

Substituting s into the transfer function, and rearranging, the difference equation for the low-pass filter in discrete form is:

$$y_k = (\alpha x_k + (1 - \alpha)y_{k-1})_{lowpass}$$

where:

$$\alpha = \frac{T}{T + \tau}$$

A high-pass filter allows high-frequency signals from gyroscopes to pass while attenuating low-frequency noise. The continuous-time form of a first-order high-pass filter is given by:

$$y(t) = \frac{\tau s}{\tau s + 1} \cdot x(t)$$

Using the same backward Euler approximation we substitute s into the transfer function and simplify to the difference equation:

$$y_k = (\beta(y_{k-1} + x_k - x_{k-1}))_{highpass}$$

where:

$$\beta = \frac{\tau}{T + \tau}$$

These discrete filter equations can be implemented in embedded C by calculating the current output y_k based on the current and previous input values, as well as the previous output value, which is stored and updated each iteration. This approach provides a robust yet lightweight solution suitable for real-time applications on embedded systems, supporting effective noise reduction in the IMU measurements.

For modularity, the complementary filter is designed to handle changes in sensor characteristics without altering the core algorithm. When switching from MTi-3 to VN-100 sensors, adjustments can be made by tuning α , β , and experimentally reproducing an f_c to account for differences in sensor noise and drift profiles. This modular approach enables agile adaptation to various IMUs, maintaining consistent performance across different hardware setups. The filter's implementation in embedded C ensures efficient real-time processing, which is crucial for the TBM environment.

Rotational IMU (RIMU) Protocol The RIMU was selected as the primary bias estimation and navigation protocol because traditional tunnel boring navigation systems, which often rely on GPS/GNSS, are ineffective underground where these signals are inaccessible. Therefore, unique approaches like the RIMU system are essential for reliable underground navigation. In industry, prism systems are typically used for this purpose, where lasers are transmitted through prisms, and triangulation determines position. However, due to the compact size and safety requirements of the Hyperloop TBM, which creates a tunnel only around two feet in diameter, setting up tripod-mounted prism stations within the tunnel is impractical and unsafe.

The Rotational IMU Protocol (RIMU) is designed to enhance the TBM's orientation tracking by estimating and compensating for intrinsic gyro bias. This protocol uses the TBM's rotational data from the IMUs to maintain accurate orientation, even under conditions where most traditional gyroscopes will drift.

The system is implemented and designed around the Rotational Inertial Measurement Unit developed by Zheming Wu, Zhenguo Sun, Wenzeng Zhang, and Qiang Chen from Tsinghua University. See *Zheming Wu et al 2015 Meas. Sci. Technol. 26 125102* for further derivation on the gyro-bias estimation protocol.

The system makes one key assumption that allows us to make the approximations we do. We assume that the TBM is not accelerating nor is it precessing, rotating, or spinning at high magnitudes. These accelerations especially cannot take place *while* the IMU is rotating as all of the measurements in-between induced rotations are not taken into account when integrating gyro rate for attitude estimates.

Upon system initialization or power cycling, the Rotational Inertial Measurement Unit (RIMU) performs calibration in a static environment. This calibration captures initial estimates of gyro rate drift and accelerometer noise, essential for baseline attitude accuracy. An initial heading (ψ_B) is obtained from magnetometer measurements and correlated with above-ground readings (ψ_E) to synchronize system orientation.

For real-time operation, the RIMU can either run continuously or activate bias estimation only during static phases (between each push and retract motion of the TBM). During live operation, the RIMU follows a state machine with three distinct states:

- *State 0 and State 1:* These are data-acceptance states. In State 0, RIMU performs real-time bias estimation and data collection. When transitioning to State 1, RIMU incorporates a rotational transformation, factoring in a +90° or

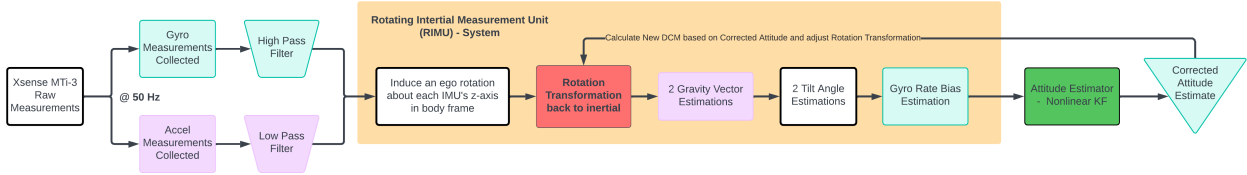


Fig. 100 Block diagram of RIMU state machine and bias estimation process

-90° rotation for IMU alignment depending on the transition direction. This enables accurate orientation compensation relative to the inertial frame.

- *State -1*: This state is used when a controlled rotation is induced through stepper motors, allowing the RIMU to generate bias estimation data by comparing angular rates with accelerometer-based tilt measurements.

Each IMU axis is converted from the left-handed MTi-3 coordinate system to a right-handed reference frame for compatibility. In States 0 and 1, the RIMU stores gyroscope and accelerometer readings for bias calculations. Bias is estimated by calculating the difference in tilt measured by the gyroscope and accelerometer, following the methodology described in the paper by Zheming Wu et al.

The bias estimation leverages the accelerometer's gravity vector to correct for gyro drift by comparing the "true attitude" derived from acceleration with the rotational data from the gyroscope. The bias-corrected gyroscope measurement, Ω_m , is modeled as:

$$\Omega_m = \Omega + b$$

where Ω is the true angular rate, and b represents the gyro bias.

To compute the tilt angles for any orientation k , we update the pitch (θ) and roll (ϕ) using the relations:

$$\begin{aligned} \Delta\theta_k &= \Omega_y \cdot \cos(\phi) - \Omega_z \cdot \sin(\phi), \\ \Delta\phi_k &= \Omega_x + (\Omega_y \cdot \sin(\phi) + \Omega_z \cdot \cos(\phi)) \cdot \tan(\theta). \end{aligned}$$

These updates allow for accurate tracking of the TBM's tilt angles, which are crucial for reliable navigation in an environment with limited external references.

When the IMU undergoes a controlled rotation, it provides multiple measurements, forming an overdetermined set of equations. Initially, we start with a 2×3 system that relates the observed tilt rate changes to the unknown bias vector. This system can be expressed as:

$$\begin{bmatrix} \Delta\theta_k \\ \Delta\phi_k \end{bmatrix} = \begin{bmatrix} \cos(\phi) & -\sin(\phi) & 0 \\ \sin(\phi) \cdot \tan(\theta) & \cos(\phi) \cdot \tan(\theta) & 1 \end{bmatrix} \begin{bmatrix} b_x \\ b_y \\ b_z \end{bmatrix} + \begin{bmatrix} \epsilon_\theta \\ \epsilon_\phi \end{bmatrix}$$

where ϵ_θ and ϵ_ϕ are the measurement noise terms in pitch and roll, respectively, and b_x , b_y , and b_z are the components of the bias vector b . Here, the 2×3 matrix cannot be directly inverted to solve for b , as there are only two equations for the three unknowns.

To resolve this, we induce additional rotations in the IMU to gather more measurements, effectively increasing the number of equations. For n induced rotations, the system expands to a $2n \times 3$ matrix, where each induced rotation provides an additional two equations. For example, with $n = 2$ rotations, we obtain a 4×3 matrix, and for $n = 3$ rotations, a 6×3 matrix, as follows:

$$\begin{bmatrix} \Delta\theta_{k_1} \\ \Delta\phi_{k_1} \\ \Delta\theta_{k_2} \\ \Delta\phi_{k_2} \\ \vdots \\ \Delta\theta_{k_n} \\ \Delta\phi_{k_n} \end{bmatrix} = \begin{bmatrix} \cos(\phi_1) & -\sin(\phi_1) & 0 \\ \sin(\phi_1) \cdot \tan(\theta_1) & \cos(\phi_1) \cdot \tan(\theta_1) & 1 \\ \cos(\phi_2) & -\sin(\phi_2) & 0 \\ \sin(\phi_2) \cdot \tan(\theta_2) & \cos(\phi_2) \cdot \tan(\theta_2) & 1 \\ \vdots & \vdots & \vdots \\ \cos(\phi_n) & -\sin(\phi_n) & 0 \\ \sin(\phi_n) \cdot \tan(\theta_n) & \cos(\phi_n) \cdot \tan(\theta_n) & 1 \end{bmatrix} \begin{bmatrix} b_x \\ b_y \\ b_z \end{bmatrix} + \begin{bmatrix} \epsilon_{\theta_1} \\ \epsilon_{\phi_1} \\ \epsilon_{\theta_2} \\ \epsilon_{\phi_2} \\ \vdots \\ \epsilon_{\theta_n} \\ \epsilon_{\phi_n} \end{bmatrix}$$

With sufficient rotations ($n \geq 2$), we achieve an overdetermined system that allows us to estimate the bias vector b using least squares estimation. This can be expressed as:

$$b = (V^T V)^{-1} V^T r$$

where V is the expanded $2n \times 3$ matrix representing the tilt angle transformations derived from the 3-2-1 angular rate to attitude rate transformation matrix, and r is the vector of measured tilt rate deviations. This method, as demonstrated in Wu et al.'s methodology, enables robust gyro bias estimation, ensuring that b converges to the true bias values over successive rotations.

The RIMU algorithm dynamically processes data by referencing the transition between the current state and the previously accepted state. When the algorithm enters State 1, it designates the State 1 measurements as the current data while leveraging the measurements collected during the prior State 0. This approach enables the algorithm to compute and apply bias corrections based on discrepancies observed between these two states. By comparing the current gyroscope and accelerometer readings with the stable measurements from the previous state, the RIMU can identify and adjust for any drift or bias that has accumulated. The current state and previous state will always switch as a transition between the two accepted states occurs. This is a vast improvement from last year's algorithm which only accepted and mitigated bias in rotation state 0. This transition-based approach ensures that each state's data is evaluated in the context of the previous state, maintaining continuity in orientation estimation. Consequently, the RIMU achieves accurate bias corrections by building on the immediate history of measurements, enhancing the reliability of real-time orientation tracking.

This RIMU process ensures consistent orientation data by continuously refining bias estimation, achieving high-accuracy orientation control. The design aligns with the bias correction methodology from Wu et al., addressing drift and enabling reliable navigation in tunnel environments without reliance on external magnetic reference frames.

Position Integrator: To track a position estimate of our system, the simplest approach is to double-integrate our acceleration measurements. However, with inherently noisy measurements, this approach leads to significant drift and noise in the resulting position estimates, making them unreliable. Therefore, a Kalman filter becomes essential to mitigate this noise and produce a more stable position estimate.

This Kalman filter revolves around a linear state and measurement model and is specifically designed to inhibit noise rather than serve as a complex sensor fusion algorithm. By selectively filtering out high-frequency noise from the accelerometer data, the Kalman filter reduces the impact of measurement errors and enhances the accuracy of position estimation over time. Its initially non-intuitive implementation allows us to maintain computational efficiency while improving the reliability of our estimates without the need to incorporate multiple sensor inputs.

We are using a simple Newtonian constant velocity A matrix, which gives us a discrete F_k matrix and a process covariance Q_k matrix. Since the IMU will experience unmodeled accelerations, we simulate the process noise with unmodeled accelerations, using the Γ vector to transform the noise matrix w_{tilde} to 6 dimensions to fit the state model's dimension. We then use actual acceleration measurements from the IMU to propagate our measurement model.

Our continuous state and measurement model is

$$\begin{aligned} \mathbf{x}(t) &= A\mathbf{x}(t) + w(t) \\ \mathbf{y}(t) &= C\mathbf{x}(t) + v(t) \end{aligned}$$

The process noise $w(t)$ is assumed to follow a normal distribution, $w(t) \sim \mathcal{N}(0, \Gamma \tilde{w} \Gamma^T)$, and the measurement noise $v(t)$ is similarly distributed as $v(t) \sim \mathcal{N}(0, R)$. The matrices are defined as follows:

$$\mathbf{x}(t) = \begin{bmatrix} x \\ \dot{x} \\ y \\ \dot{y} \\ z \\ \dot{z} \end{bmatrix}, \quad A = \begin{bmatrix} 0 & 1 & 0 & 0 & 0 & 0 \\ 0 & 0 & 0 & 0 & 0 & 0 \\ 0 & 0 & 0 & 1 & 0 & 0 \\ 0 & 0 & 0 & 0 & 0 & 0 \\ 0 & 0 & 0 & 0 & 0 & 1 \\ 0 & 0 & 0 & 0 & 0 & 0 \end{bmatrix}, \quad \Gamma = \begin{bmatrix} 0 & 0 & 0 \\ 1 & 0 & 0 \\ 0 & 0 & 0 \\ 0 & 1 & 0 \\ 0 & 0 & 0 \\ 0 & 0 & 1 \end{bmatrix}, \quad \tilde{w} = I$$

Since this state model is based on a Newtonian constant velocity assumption, unmodeled accelerations will inevitably occur. To account for this, we introduce the process noise covariance variable \tilde{w} , which primarily affects the velocity components within the state and represents the impact of unmodeled accelerations. We initialize \tilde{w} as a 3×3 identity matrix. Given that this noise covariance pertains to accelerations, we use the Γ matrix to map \tilde{w} to a 6-dimensional space, aligning with the state dimensions. Actual acceleration measurements from the IMU are then used to propagate the measurement model.

The initial estimate for the covariance matrix, \tilde{w} , is set as the identity matrix to provide a baseline for state propagation. We are currently conducting experiments to collect ground truth data by inducing controlled motion through our hexapod system. Using this data, we aim to implement a *Hidden Markov Model* (HMM) approach to estimate the \tilde{w} matrix, capturing how the Stewart platform introduces unmodeled accelerations into our state-space dynamics.

Our measurement model $y(t)$ with accelerometer measurements from the IMU in terms of acceleration is represented as:

$$\mathbf{y}(t) = H\mathbf{x}(t) + v(t), \quad H = \begin{bmatrix} 0 & 1 & 0 & 0 & 0 & 0 \\ 0 & 0 & 0 & 1 & 0 & 0 \\ 0 & 0 & 0 & 0 & 0 & 1 \end{bmatrix}$$

However, our Kalman filter operates in discrete time. The well-known solution to our first-order ordinary differential state-space equation when sampled at T is e^{AT} and therefore our discrete transfer functions and covariances are:

$$\begin{aligned} F_k &= e^{AT} = \mathcal{L}^{-1} \{(sI - A)^{-1}\}_{t=T} \\ H_k &= C \\ Q_k &= \int_{\tau=0}^T e^{A\tau} Q e^{A^T \tau} d\tau \\ R_k &= R \cdot \frac{1}{T} \end{aligned}$$

We can calculate our discrete state space transfer function F_k and process covariance Q_k through *Van Loan's Method*. This method involves constructing a specific block matrix Z and calculating its matrix exponential.

$$Z = \begin{bmatrix} -A & Q \\ 0 & A^T \end{bmatrix}$$

Next, we calculate the matrix exponential of Z :

$$G = e^{Z \cdot T} = \begin{bmatrix} \dots & F_k^{-1} Q_k \\ 0 & F_k^T \end{bmatrix}$$

In this result, $G = e^{AT}$ represents the discrete state transition matrix, and Q_k represents the discretized process noise covariance. This Q_k covariance ends up being coupled because of the relationship between our constant velocity model and taking the unmodeled acceleration into effect by setting $Q_{continuous} = \Gamma \cdot \tilde{w} \cdot \Gamma^T$.

From the matrix G , F_k can be identified as the lower-right partition of G , and Q_k can be determined from the upper-right partition of G as follows:

$$Q_k = (F_k^T)^T \cdot (F_k^{-1} Q_k) = F_k^t \cdot (\text{upper-right partition of } G)$$

The discrete process noise Q_k is thus evaluated by multiplying the transpose of the lower-right partition of G with the upper-right partition of G .

This model aims to capture the continuous dynamics of the system and incorporates unmodeled acceleration through process noise factors to account, for ensuring a more robust position estimation.

Nonlinear State Model for Attitude Estimator: Define the state vector, which consists of the Euler angles and gyro bias:

$$\mathbf{x} = \begin{bmatrix} \phi \\ \theta \\ \psi \\ b_x \\ b_y \\ b_z \end{bmatrix}$$

where:

- ϕ, θ , and ψ are the roll, pitch, and yaw Euler angles.
- b_x, b_y , and b_z are the biases in the gyroscope measurements.

The Euler angles evolve based on the current orientation and the corrected gyroscope measurements. Let $\omega_{meas} = [\omega_x, \omega_y, \omega_z]^T$ represent the measured angular rates, which include bias. The true angular rates $\omega = [p, q, r]^T$ are obtained by removing this bias:

$$\omega = \omega_{meas} - \begin{bmatrix} b_x \\ b_y \\ b_z \end{bmatrix}$$

The dynamics of the Euler angles are given by:

$$\begin{bmatrix} \dot{\phi} \\ \dot{\theta} \\ \dot{\psi} \end{bmatrix} = \mathbf{T}(\phi, \theta) \begin{bmatrix} p \\ q \\ r \end{bmatrix}$$

where $\mathbf{T}(\phi, \theta)$ is the transformation matrix defined as:

$$\mathbf{T}(\phi, \theta) = \begin{bmatrix} 1 & \sin(\phi) \tan(\theta) & \cos(\phi) \tan(\theta) \\ 0 & \cos(\phi) & -\sin(\phi) \\ 0 & \sin(\phi)/\cos(\theta) & \cos(\phi)/\cos(\theta) \end{bmatrix}$$

The gyro biases b_x, b_y , and b_z are estimated using the **RIMU Protocol**, which at each timestep k returns the updated bias values based on the latest gyroscope and accelerometer data and time increment Δt .

Thus, the continuous-time state dynamics can be summarized as:

$$\dot{\mathbf{x}} = \begin{bmatrix} \dot{\phi} \\ \dot{\theta} \\ \dot{\psi} \\ \dot{b}_x \\ \dot{b}_y \\ \dot{b}_z \end{bmatrix} = \begin{bmatrix} \mathbf{T}(\phi, \theta) (\omega_{meas} - \mathbf{b}) \\ \mathbf{RIMU}(\omega_{meas}, a_x, \Delta t) \end{bmatrix}$$

The accelerometer measurements provide gravity-based information to estimate roll and pitch. Let $\mathbf{a}_{meas} = [a_x, a_y, a_z]^T$ represent the accelerometer measurements, which are influenced by gravity as follows:

$$a_x = -g \sin(\theta), \quad a_y = g \sin(\phi) \cos(\theta), \quad a_z = g \cos(\phi) \cos(\theta)$$

Thus, the measurement vector is:

$$= \begin{bmatrix} a_x \\ a_y \\ a_z \end{bmatrix}$$

with the measurement function $h(\mathbf{x})$ defined as:

$$h(\mathbf{x}) = \begin{bmatrix} -g \sin(\theta) \\ g \sin(\phi) \cos(\theta) \\ g \cos(\phi) \cos(\theta) \end{bmatrix}$$

Complete State-Space Model

Combining the state and measurement equations, the state-space model for the attitude estimator is:

State Equation:

$$\dot{\mathbf{x}} = f(\mathbf{x}, \mathbf{u}, w) = \begin{bmatrix} \mathbf{T}(\phi, \theta) (\omega_{meas} - \mathbf{b}) \\ \mathbf{RIMU}(\omega_{meas}, a_x, \Delta t) \end{bmatrix}$$

Measurement Equation:

$$\mathbf{y} = h(\mathbf{x}, v) = \begin{bmatrix} -g \sin(\theta) \\ g \sin(\phi) \cos(\theta) \\ g \cos(\phi) \cos(\theta) \end{bmatrix}$$

This state model forms the basis for implementing a nonlinear filter such as the Unscented Kalman Filter defined below for attitude estimation.

3. Sensor Fusion - Unscented Kalman Filter

The Unscented Kalman Filter (UKF) is the industry standard when approaching nonlinear state estimation problems. This approach, derived in 1995 by Uhlmann and Julier, estimates the state with a second-order degree of accuracy while retaining the same level of covariance estimation capabilities as an EKF without the need to calculate Jacobian or Hessian matrices. We have several state estimators acting concurrently within our system to enhance the accuracy of inherently noisy and unreliable dead-reckoning information onboard the TBM.

This filter acts as a sensor fusion algorithm between our Inclinometers, IMU system, and inverse-kinematics calculations from our hexapod system's encoder measurements. The RIMU and Hexapod system have their own inherent filters and calculations being made such that the inputs to this sensor-fusing state estimator are purely partial or full state estimates.

We follow the direction and derivation provided by Haykin in *Kalman Filtering and Neural Networks*.

Initialization The UKF begins by initializing the state vector and covariance matrix. Let:

$$\hat{\mathbf{x}}_0 = \mathbf{E}[\mathbf{x}_0]$$

$$\mathbf{P}_0 = \mathbf{E}[(\mathbf{x}_0 - \hat{\mathbf{x}}_0)(\mathbf{x}_0 - \hat{\mathbf{x}}_0)^T]$$

Sigma Point Generation Given the current state estimate $\hat{\mathbf{x}}_k$ and its covariance \mathbf{P}_k , we generate $2L + 1$ sigma points \mathbf{X}_i using:

$$\begin{aligned} \mathbf{X}_0 &= \hat{\mathbf{x}} \\ \mathbf{X}_i &= \hat{\mathbf{x}} + \left(\sqrt{(L + \lambda)\mathbf{P}_x} \right)_i, \quad i = 1, \dots, L \\ \mathbf{X}_{i-L} &= \hat{\mathbf{x}} - \left(\sqrt{(L + \lambda)\mathbf{P}_x} \right)_{i-L}, \quad i = L + 1, \dots, 2L \end{aligned}$$

where $\lambda = \alpha^2(L + \kappa) - L$. Here, α , κ , and β are tuning parameters, with α controlling the spread of sigma points around the mean, κ typically set to 0, and $\beta = 2$ for Gaussian noise.

Nonlinear Transformation of Sigma Points The sigma points are propagated through the nonlinear system function f :

$$\mathbf{Y}_i = f(\mathbf{X}_i), \quad i = 0, \dots, 2L$$

Mean and Covariance of Transformed Points The mean $\bar{\mathbf{y}}$ and covariance \mathbf{P}_y of the transformed points are approximated as:

$$\begin{aligned}\bar{\mathbf{y}} &\approx \sum_{i=0}^{2L} W_i^{(m)} \mathbf{Y}_i \\ \mathbf{P}_y &\approx \sum_{i=0}^{2L} W_i^{(c)} (\mathbf{Y}_i - \bar{\mathbf{y}})(\mathbf{Y}_i - \bar{\mathbf{y}})^T\end{aligned}$$

where the weights $W_i^{(m)}$ and $W_i^{(c)}$ are given by:

$$\begin{aligned}W_0^{(m)} &= \frac{\lambda}{L+\lambda}, \quad W_0^{(c)} = \frac{\lambda}{L+\lambda} + 1 - \alpha^2 + \beta \\ W_i^{(m)} &= W_i^{(c)} = \frac{1}{2(L+\lambda)}, \quad i = 1, \dots, 2L\end{aligned}$$

Time-Update Equations (Prediction) The sigma points are then propagated through the system dynamics:

$$\mathbf{X}_{i,k|k-1}^* = F(\mathbf{X}_{i,k-1}, \mathbf{u}_{k-1})$$

The predicted mean and covariance of the state are then given by:

$$\begin{aligned}\hat{\mathbf{x}}_k &\approx \sum_{i=0}^{2L} W_i^{(m)} \mathbf{X}_{i,k|k-1}^* \\ \mathbf{P}_k &\approx \sum_{i=0}^{2L} W_i^{(c)} (\mathbf{X}_{i,k|k-1}^* - \hat{\mathbf{x}}_k)(\mathbf{X}_{i,k|k-1}^* - \hat{\mathbf{x}}_k)^T + \mathbf{R}^v\end{aligned}$$

Measurement-Update Equations (Correction) The propagated sigma points are passed through the measurement model:

$$\mathbf{Y}_{i,k|k-1}^* = H(\mathbf{X}_{i,k|k-1}^*)$$

The predicted measurement mean and covariance are calculated as:

$$\begin{aligned}\hat{\mathbf{y}}_k &\approx \sum_{i=0}^{2L} W_i^{(m)} \mathbf{Y}_{i,k|k-1}^* \\ \mathbf{P}_{\mathbf{y}_k \mathbf{y}_k} &\approx \sum_{i=0}^{2L} W_i^{(c)} (\mathbf{Y}_{i,k|k-1}^* - \hat{\mathbf{y}}_k)(\mathbf{Y}_{i,k|k-1}^* - \hat{\mathbf{y}}_k)^T + \mathbf{R}^n\end{aligned}$$

The cross-covariance matrix between the state and the measurement is:

$$\mathbf{P}_{\mathbf{x}_k \mathbf{y}_k} = \sum_{i=0}^{2L} W_i^{(c)} (\mathbf{X}_{i,k|k-1}^* - \hat{\mathbf{x}}_k)(\mathbf{Y}_{i,k|k-1}^* - \hat{\mathbf{y}}_k)^T$$

Kalman Gain and State Update The Kalman gain \mathbf{K}_k , updated state $\hat{\mathbf{x}}_k$, and updated covariance \mathbf{P}_k are computed as:

$$\begin{aligned}\mathbf{K}_k &= \mathbf{P}_{\mathbf{x}_k \mathbf{y}_k} \mathbf{P}_{\mathbf{y}_k \mathbf{y}_k}^{-1} \\ \hat{\mathbf{x}}_k &= \hat{\mathbf{x}}_k + \mathbf{K}_k (\mathbf{y}_k - \hat{\mathbf{y}}_k) \\ \mathbf{P}_k &= \mathbf{P}_k - \mathbf{K}_k \mathbf{P}_{\mathbf{y}_k \mathbf{y}_k} \mathbf{K}_k^T\end{aligned}$$

This cycle of prediction and update is repeated whenever the Guidance, Navigation, and Control (GNC) system requires an updated state estimate within the behavior tree. The UKF's use of sigma points and nonlinear transformations allows it to handle the TBM's nonlinear dynamics accurately and efficiently. We implement this architecture into Python such that it communicates with messages from other processes of the behavior tree and is only called when we need a localized position estimate and its corresponding covariance.

XIV. Electrical System

A. General Philosophy

Our philosophy towards designing PCBs is focusing on efficiency, reliability, and cost-effectiveness. This is achieved by standardizing components and creating a minimal viable product to use for testing purposes, then iterating on the design for final integration. Minimizing the amount of unique components allows us to simplify the design process and cut costs when ordering components.

B. Printed Circuit Board Overview

The electrical system contains 11 total PCBs each controlled by a Teensy 4.1 microcontroller: 7 in-machine PCBs, 1 in-machine daughterboard, and 4 above-ground PCBs. All in-machine boards are powered by 2 redundant 12VDC, 3000W power supplies located in the rear section of the TBM. All above-ground boards are powered by a single 960W, 24VDC power supply located in the high-power enclosure. Furthermore, each board steps down and filters the input voltage to 5VDC to power the microcontroller and other low-power components.

All boards have a 24V operational E-STOP input which is activated at the ground station and stops all moving parts. All PCBs communicate via Ethernet which is connected to network switches in the rear section of our machine. All PCBs have reverse polarity protection, internal and external indicator LEDs, and test points for debugging. Additionally, we are using vertical connectors for easier integration into our 3D-printed PCB enclosures.

In-Machine PCBs

- 1) Hexapod Board
- 2) Tunnel Support Board
- 3) Excavation Board
- 4) Rotational Inertial Measurement Unit (RIMU) Board
- 5) Front Inclinometer Board
- 6) Rear Gripper Board
- 7) Segment Ejection Board

Above Ground PCBs

- 8) Ground Conditioning System (GCS) Board
- 9) Pneumatic Board
- 10) Power Board
- 11) Cooling Board

1. Hexapod Board

- 1) Board Overview

The Hexapod board controls six electric linear actuators that generate forward thrust for the TBM. Each actuator is controlled using a water-cooled full-bridge motor driver IC which has built-in high-side and low-side thermal shutdown, under and over-voltage shutdown, output short protection, and current sensing capability. The Hexapod

board also uses the actuators' built-in Hall-effect sensors for precise position control and uses the full-bridge chips' current sensing capability to modulate actuator force.

2) Sensor List

Sensor	Part Count	Accuracy	Data Frequency	Nominal Range	Interface Type	Supply Voltage (VDC)
Hall Effect Sensor	6	N/A	92 Pulses/inch	-40 to 60°C	Analog	5V
Ambient Temperature	1	$\pm 0.25^\circ\text{C}$	continuous	-55°C to 125°C	I ² C	5V

Table 14 Hexapod Sensor List

3) Power Consumption

Component	Component Count	Current Draw Per Component (mA)	Total Current Draw (mA)	Power Consumption (W)
Fully Integrated H-Bridge motor driver	6	20.5A	123A	1476
Reverse Polarity	1	6.5	6.5	0.078
I ² C Multiplexor	1	75	75	0.375
HALL Effect Sensor	6	15	0.09	0.45
Teensy 4.1	1	0.25	0.25	1.25
Totals				1478 W

Table 15 hexapod Power Consumption

4) Schematic

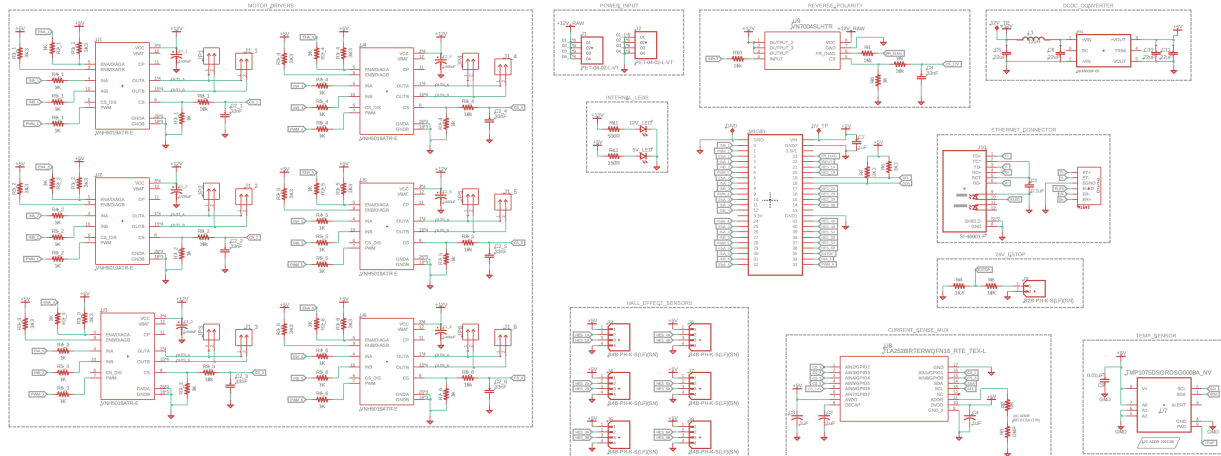


Fig. 101 Hexapod Schematic

5) Board Layout

2. Tunnel Support Board

1) Board Overview

The Tunnel Support Board is responsible for controlling all relevant tunnel support subsystems including the R-Z-Theta 3D-printer mechanism. It controls two theta-axis stepper motors, four stepper motors for the filament extrusion system, two linear actuators for the R axis, two stepper motors for the Z axis, as well as limit switches for the R, Z, and theta axes. The tunnel support board also controls two solid-state relays which control the nozzle heating elements.

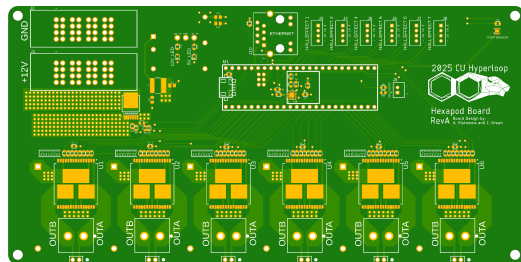


Fig. 102 Hexapod PCB Top

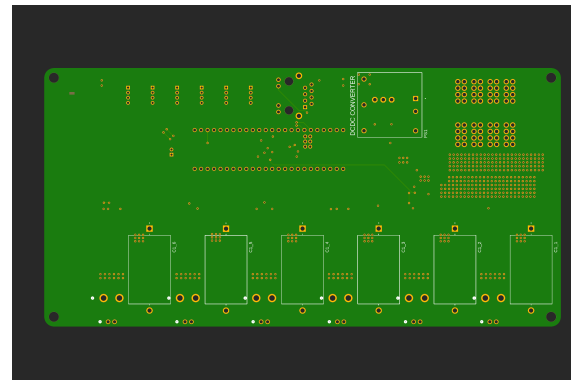


Fig. 103 Hexapod PCB Bottom

2) Sensor List

Sensors	Part Count	Accuracy	Data Frequency	Nominal Range	Interface Type	Supply Voltage (VDC)
Ambient Temperature	1	$\pm 0.25^\circ\text{C}$	continuous	-55°C to 125°C	I ² C	5V
Limit Switches	4	N/A	continuous	N/A	Digital	24V

Table 16 Tunnel Support Sensor List

3) Power Consumption

Component	Component Count	Current Draw Per Component (mA)	Total Current Draw (mA)	Power Consumption (W)
R & Z Limit Switches	4	20	80	1.92
Z - Stepper Motors	2	1.5A	3.0A	36
Stepper Motor Driver	2	8	16	0.008
Theta Motor	2	6A	12A	288
Extrusion Motors	4	2.8A	5.6A	134.4
Thermistor	4	5mA	20mA	0.2
Solid State Relay	2	25mA	50mA	1.2
Totals				461.728 W

Table 17 Tunnel Support Power Consumption

4) Schematic [N/A]

5) Board Layout [N/A]

3. Excavation Board

1) Board Overview

The Excavation board is the interface between the ground station and the excavation motor controller. This board allows us to set up the conditions necessary to control the excavation motor. This board controls the direction of the motor and controls the speed of the motor with an analog signal. The board uses a CAN transceiver to read motor parameters such as RPM and temperature.

2) Sensor List

Sensors	Part Count	Accuracy	Data Frequency	Nominal Range	Interface Type	Supply Voltage (VDC)
Pressure Transducer	2	$\pm 0.05\%$	N/A	-20 to 15°C, 0 to 5800 psi	Analog	12V

Table 18 Excavation Sensor List

3) Power Consumption

Component	Component Count	Current Draw Per Component (mA)	Total Current Draw (mA)	Power Consumption (W)
100VDC Contactor	1	1.5A	1.5A	18
Pressure Transducer	2	20	40	1.28
CAN Transceiver	1	70	70	0.23
Teensy 4.1	1	250	250	1.25
			Totals	19.5 W

Table 19 Excavation Power Consumption

4) Schematic

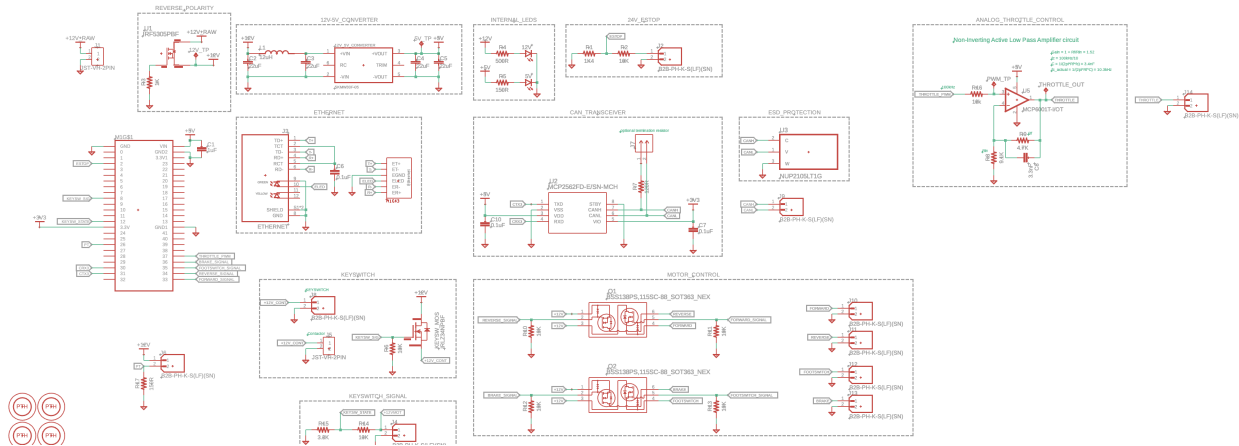


Fig. 104 Excavation Schematic

5) Board Layout

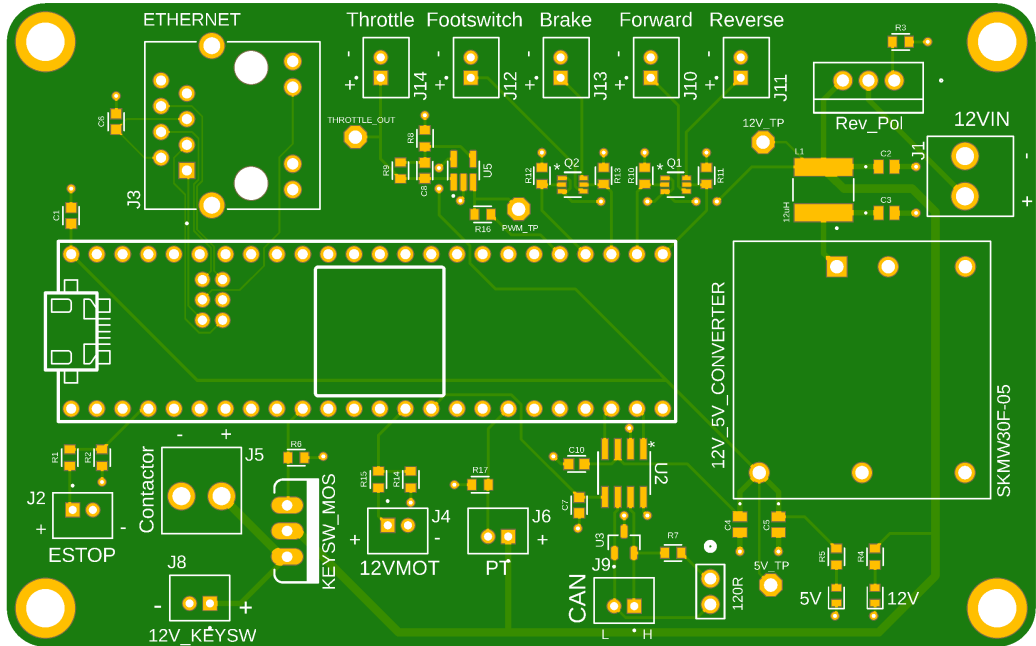


Fig. 105 Excavation PCB Top

4. Rotational Inertial Measurement Unit (RIMU) Board

1) Board Overview

The Rotational Inertia Measurement Unit (RIMU) Board is part of our navigational system. It rotates three VectorNav IMUs using stepper motors, enabling precise collection and monitoring of accelerational data which we then integrate for position. The board leverages UART communication and software synchronization to validate incoming data. Additionally, the board integrates a pressure transducer to monitor pressure in one front gripper for redundancy and includes a methane sensor for safety.

2) Sensor List

Sensors	Part Count	Accuracy	Data Frequency	Nominal Range	Interface Type	Supply Voltage (VDC)
Stepper Motor Driver	3	200 steps per revolution	N/A	-20 to 85°C	PWM	12V
Methane Sensor	1	±2%	N/A	200-10000 ppm, -20 to 70°C	Analog	5V
Pressure Transducer	1	±0.4%	N/A	0-100 PSI, -28 to 71°C	Analog	5V
Vectornav IMU	3	800 Hz Sample, (2 deg)	Output: 1 kHz	-40 to 85°C	UART	5V

Table 20 RIMU Sensor List

3) Power Consumption

Component	Component Count	Current Draw Per Component (mA)	Total Current Draw (mA)	Power Consumption (W)
Stepper Motor Driver	3	8	24	0.12
Stepper Motors	3	600	1800	21.6
Methane Sensor	1	150	150	0.75
Pressure Transducer	1	20	20	0.1
Vectornav IMU	3	40	120	0.6
Teensy 4.1	1	250	250	1.25
		Totals		24.42 W

Table 21 RIMU Power Consumption

4) Schematic

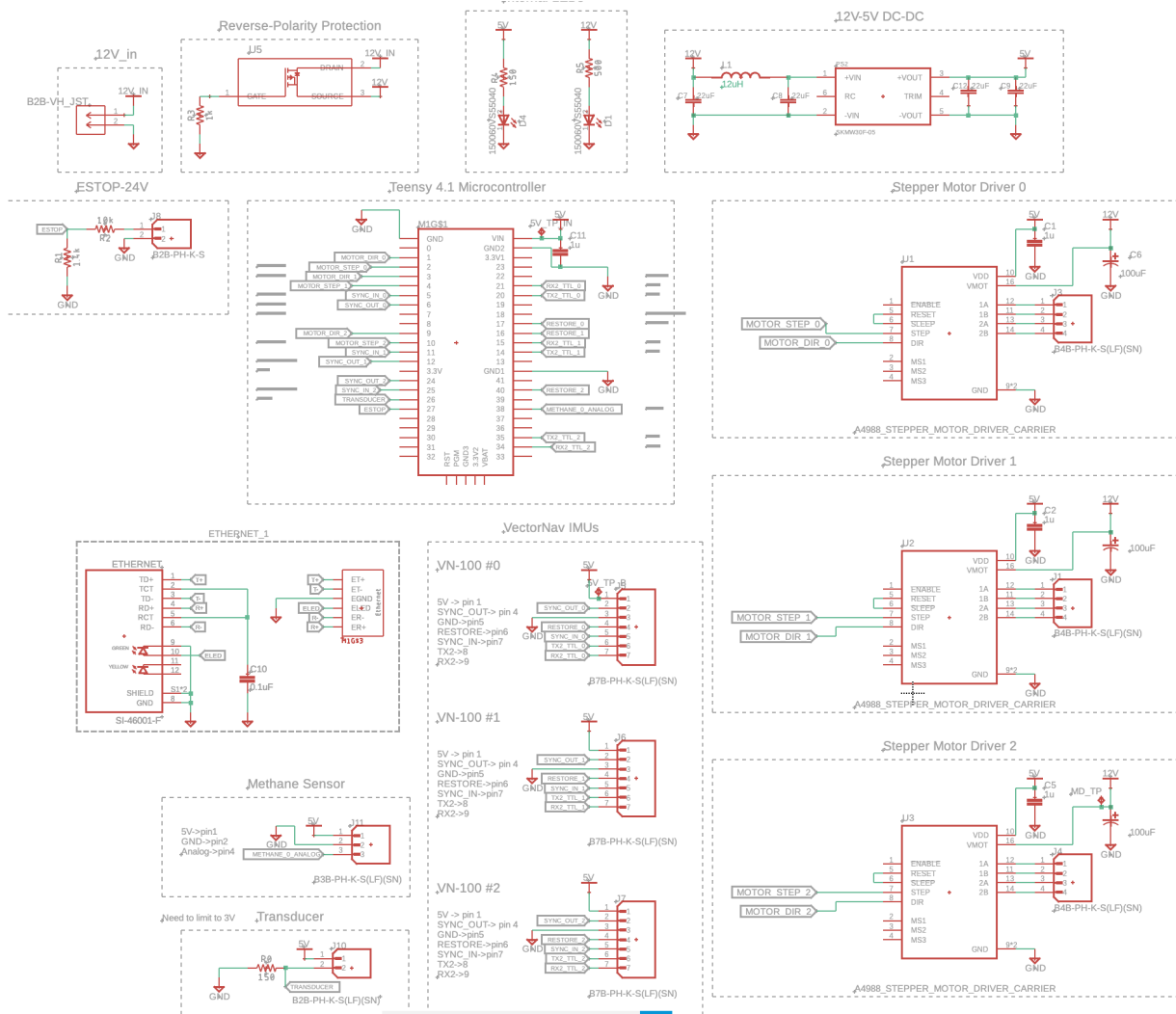


Fig. 106 RIMU Schematic

5) Board Layout

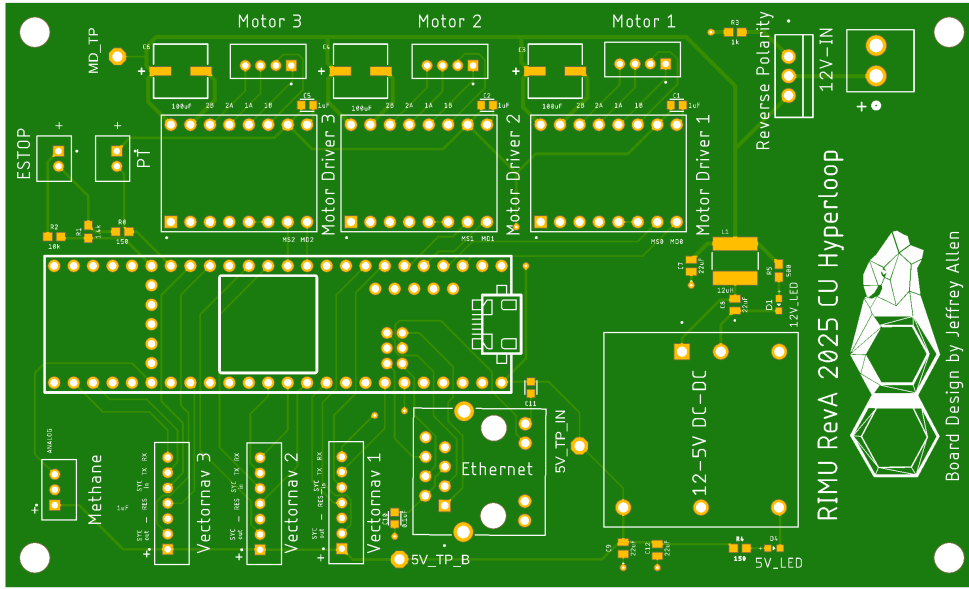


Fig. 107 RIMU PCB Top

5. Front Inclinometer Board

1) Board Overview

The front inclinometer board is the second board in our navigation system. It has two inclinometers that measure the pitch and roll angles of the front of the TBM. The front inclinometers are used in conjunction with two additional inclinometers placed in the rear of the machine to find the orientation of the TBM. This board also has two pressure transducers which measure the pressure in two of the three front grippers, and two methane sensors to detect the presence of methane gas.

2) Sensor List

Sensors	Part Count	Accuracy	Data Frequency	Nominal Range	Interface Type	Supply Voltage (VDC)
Inclinometers	2	$\pm 0.25^\circ$	80Hz	-40 to +80°C	Analog	24V
Pressure Transducer	2	$\pm 0.4\%$	N/A	-20 to 70°C	Analog	5V
Methane Sensor	2	$\pm 0.4\%$	N/A	0-100 PSI, -28 to 71°C	Analog	5V
Motor Thermistors	2	$\pm 1\%$	Continuous	-40 to 105°C	Analog	12V

Table 22 Front Inclinometer Sensor List

3) Power Consumption

Component	Component Count	Current Draw Per Component (mA)	Total Current Draw (mA)	Power Consumption (W)
Inclinometers	2	20	40	0.96
Pressure Transducer	2	20	40	0.48
Motor Thermistors	2	15	30	0.36
Methane Sensor	2	150	300	1.5
			Totals	3.3 W

Table 23 Front Inclinometer Power Consumption

4) Schematic

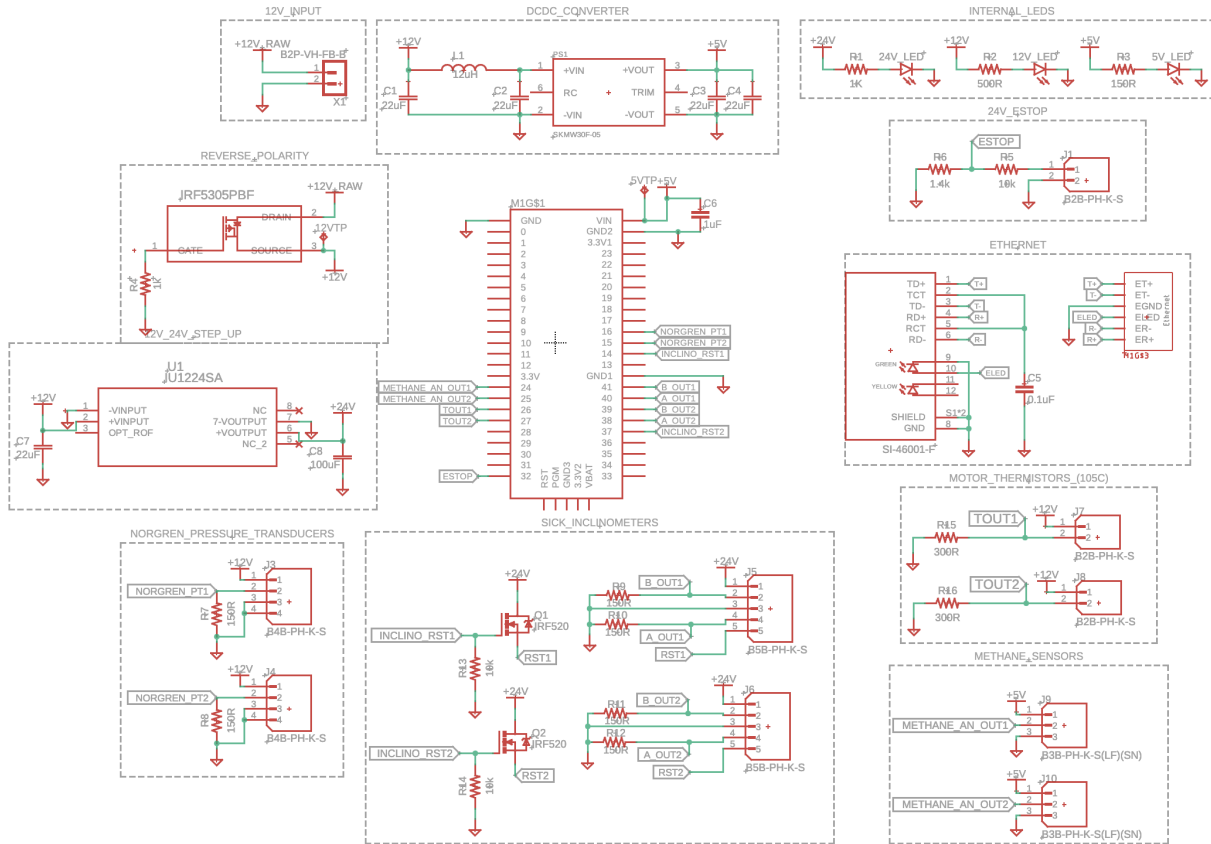


Fig. 108 Front Inclinometer Schematic

5) Board Layout

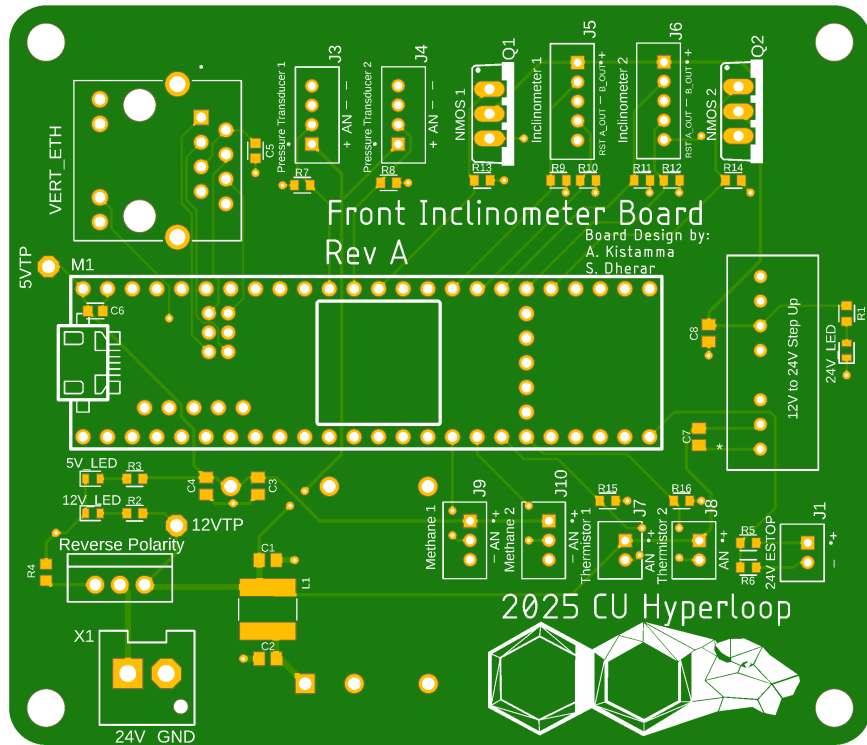


Fig. 109 Front Inclinometer PCB Top

6. Rear Gripper Board

1) Board Overview

The Rear Gripper Board monitors the temperature for the hexapod actuators using 12 thermistors and monitors ambient temperature in the hexapod section of the TBM. Additionally, it monitors the pressure of two rear grippers, and checks pressure levels in the soil removal hose to detect blockages.

2) Sensor List

Sensors	Part Count	Accuracy	Data Frequency	Nominal Range	Interface Type	Supply Voltage (VDC)
Thermistors	13	$\pm 1\%$	Continuous	-40 to 105°C	Analog	12V
Pressure Transducer	3	$\pm 0.4\%$	Continuous	-28 to 71°C, 0-100 PSI	Analog	12V

Table 24 Rear Gripper Sensor List

3) Power Consumption

Component	Component Count	Current Draw Per Component (mA)	Total Current Draw (mA)	Power Consumption (W)
Teensy 4.1	1	250	250	1.25
LED Driver	1	45	45	7.2
Solenoid Valves	6	270	270	19.44
Totals				27.89 W

Table 25 Rear Gripper Power Consumption

4) Schematic

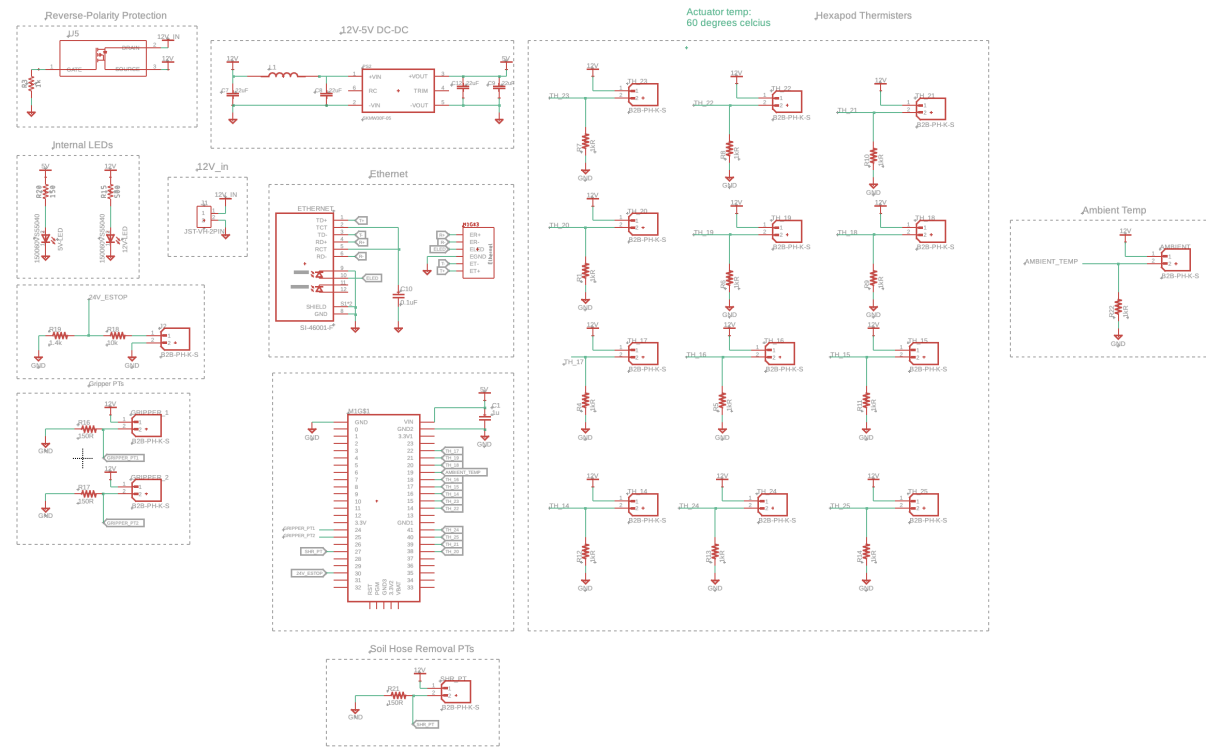


Fig. 110 Rear Gripper Schematic

5) Board Layout

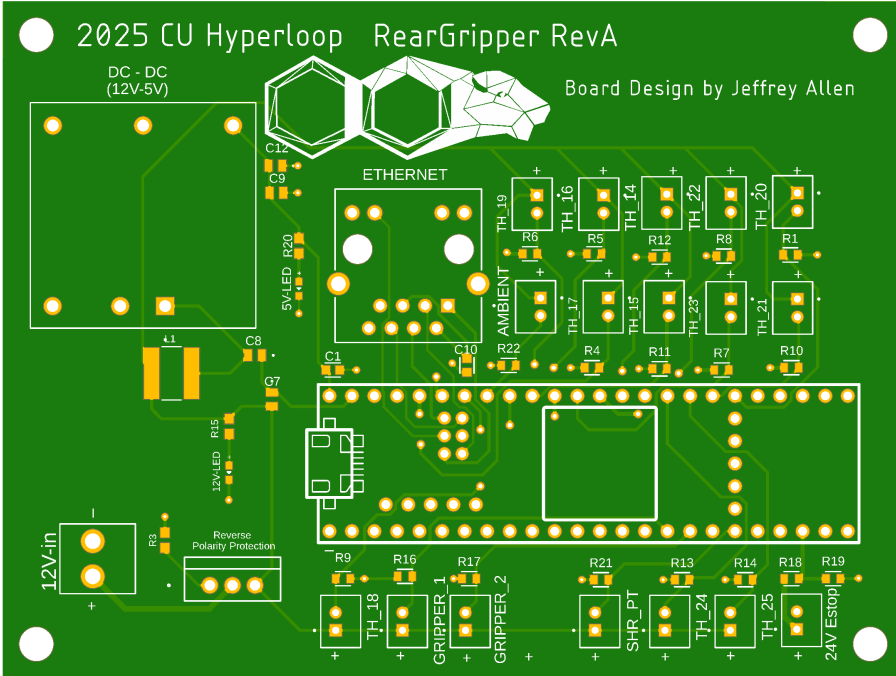


Fig. 111 Rear Gripper PCB Top

7. Segment Ejection Board

1) Board Overview

The Segment Ejection Board controls six electric linear actuators that push completed sections of 3D-printed tunnel support out of the TBM. It also collects data from two inclinometers that measure the pitch and roll angles of the rear of the TBM. These inclinometers are used in conjunction with two additional inclinometers placed in the front of the machine to find the orientation of the TBM. This board has not been completed due to the delayed timeline of the tunnel support system.

2) Sensor List

Sensor	Part Count	Accuracy	Data Frequency	Nominal Range	Interface Type	Supply Voltage (VDC)
Inclinometers	2	$\pm 0.25^\circ$	80 Hz	-40 to 80°C	Analog	24V
Actuators	6	N/A	N/A	10" stroke	N/A	12V
Thermistor	1	$\pm 1\%$	Continuous	-40 to 105°C	Analog	12V

Table 26 Segment Ejection Sensor List

3) Power Consumption

Component	Component Count	Current Draw Per Component (mA)	Total Current Draw (mA)	Power Consumption (W)
Inclinometers	2	35	70	1.68
Segment Ejection Actuators	6	4.6A	27.6A	331
Ambient Temperature Thermistor	1	15	15	0.18
Totals				332.86 W

Table 27 Segment Ejection Power Consumption

- 4) Schematic [N/A]
- 5) Board Layout [N/A]

8. Ground Conditioning System (GCS) Board

1) Board Overview

The GCS Board enables precise monitoring and control of fluid flow for the ground conditioning system. It controls two electric pumps by regulating current draw through current sense resistors. Additionally, two flowmeters are used to monitor the flow of water and solution fluids, providing real-time feedback for fluid mixing.

2) Sensor List

Sensors	Part Count	Accuracy	Data Frequency	Nominal Range	Interface Type	Supply Voltage
Flow Meter	1	$\pm 5\%$	1062 pulse/Liter	40°C max, 145 PSI max	Digital	120VAC
Digital Flow Meter	1	$\pm 0.5\%$	112 Pulses/Liter	-40 to 80°C	ADC	24V

Table 28 GCS Sensor List

- 3) Power Consumption

Component	Component Count	Current Draw Per Component (mA)	Total Current Draw (mA)	Power Consumption (W)
Fluid Pump	1	1.61A	1.61A	38.64
Fluid Pump	1	5.2A	5.2A	124.8
Digital Flow Meter	1	20	20	0.48
Inductive Proximity Sensor	1	15	15	0.36
Teensy 4.1	1	250	250	1.25
LED Driver	1	45	45	7.2
Totals				172.73 W

Table 29 GCS Power Consumption

- 4) Schematic

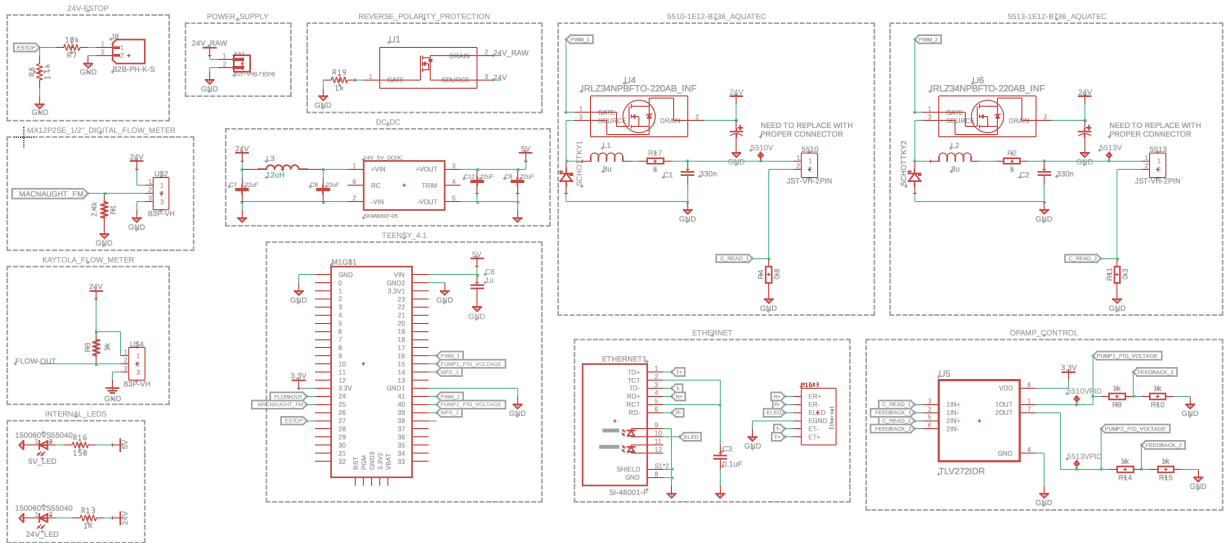


Fig. 112 GCS Schematic

5) Board Layout

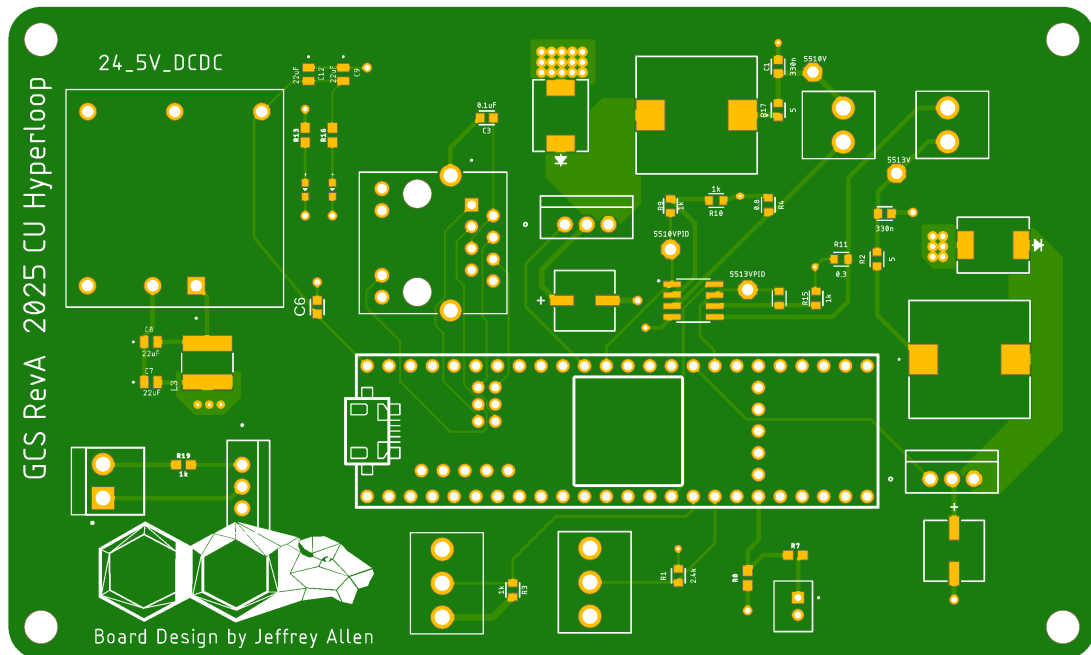


Fig. 113 GCS PCB Top

9. Pneumatic Board

1) Board Overview

2) Sensor List

Sensor	Part Count	Accuracy	Data Frequency	Nominal Range	Interface Type	Supply Voltage (VDC)
Solenoid Valves	6	N/A	N/A	-29°C to 71°C	4.91 to 150 PSI	12V

Table 30 Pneumatic Sensor Specifications

3) Power Consumption

Component	Component Count	Current Draw Per Component (mA)	Total Current Draw (mA)	Power Consumption (W)
Teensy 4.1	1	250	250	1.25
LED Driver	1	45	45	7.2
Solenoid Valves	6	270	270	19.44
			Totals	27.89 W

Table 31 Pneumatic Power Consumption

4) Schematic

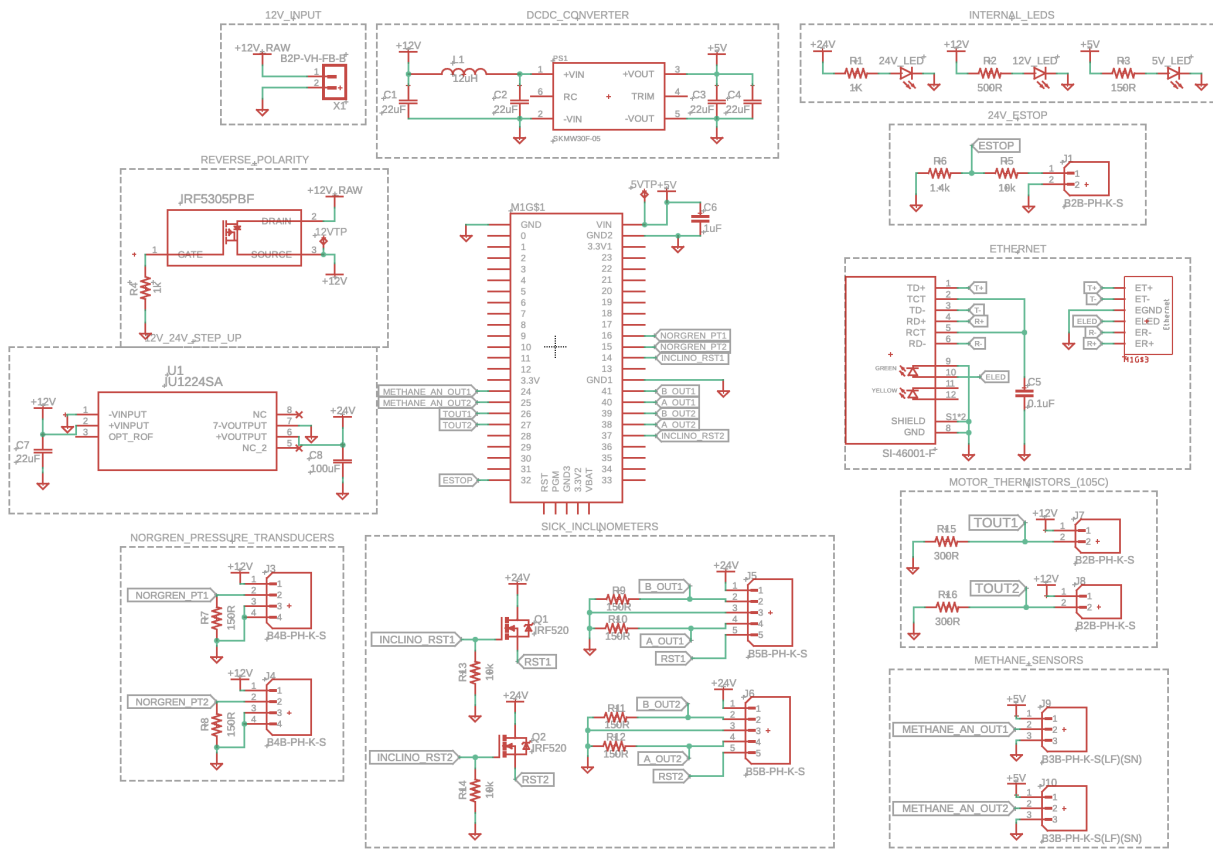


Fig. 114 Front Inclinometer Schematic

5) Board Layout

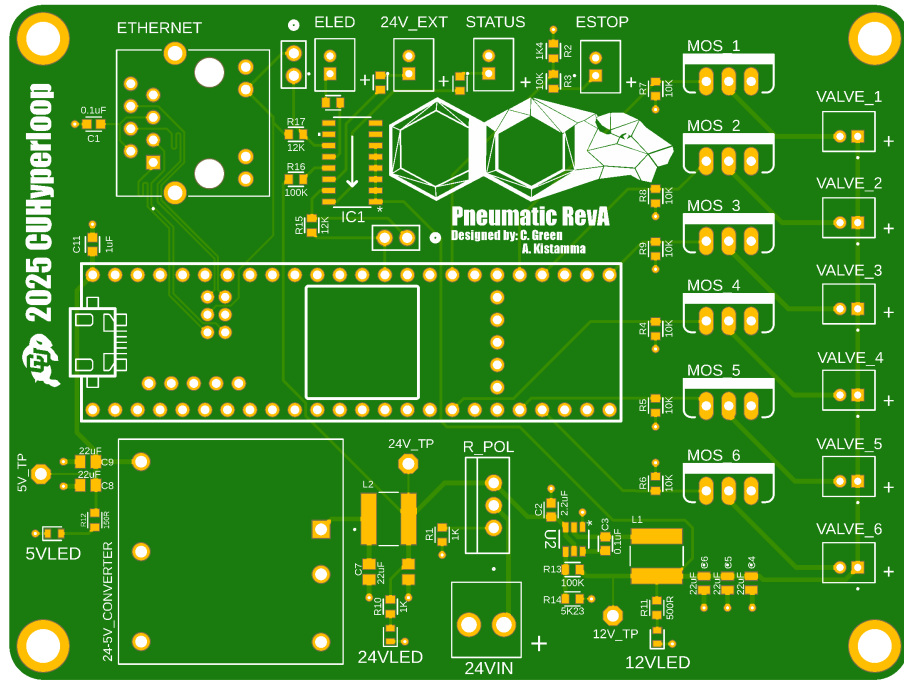


Fig. 115 Pneumatic PCB Top

10. Power Board

1) Board Overview

The Power Board monitors the different power distributions and ensures that the high power system is operating within expected levels. This board is located in the high power box and collects data from the voltage transducers, current transducers, and GFCIs outputs, relaying data back to our ground station for interpretation.

2) Sensor List

Sensor	Part Count	Accuracy	Data Frequency	Nominal Range	Interface Type	Supply Voltage (VDC)
480VAC GFCI	1	N/A	N/A	-20°C to 50°C	Digital	120VAC
120VAC GFCI	1	N/A	N/A	-20°C to 50°C	Digital	24V
100VDC GFCI	1	N/A	N/A	-20°C to 50°C	Digital	24V
480VAC Current Transducer	1	1.0%	30-100Hz	0-50A	Analog	24V
120VAC Current Transducer	1	1.0%	4-400Hz	0-200A	Analog	24V
100VDC Current Transducer	1	2.0%	4-400Hz	0-300A	Analog	24V
480VAC Voltage Transducer	1	0.5%FS	25Hz to 1kHz	0% 120% measuring range	Analog	24V
120VAC Voltage Transducer	1	<1%	0-5kHz	0-150VAC	Analog	24V
100VDC Voltage Transducer	1	<1%	0-5kHz	0-150VDC	Analog	24V

Table 32 Power Sensor Specifications

3) Power Consumption

Component	Component Count	Current Draw Per Component (mA)	Total Current Draw (mA)	Power Consumption (W)
480VAC GFCI	1	20	20	2.4
120VAC GFCI	1	20	20	0.48
100VDC GFCI	1	20	20	0.48
480VAC Current Transducer	1	80	80	1.92
120VAC Current Transducer	1	20	20	0.48
100VDC Current Transducer	1	20	20	0.48
480VAC Voltage Transducer	1	10	10	0.24
120VAC Voltage Transducer	1	20	20	0.48
100VDC Voltage Transducer	1	20	20	0.48
Totals				7.44 W

Table 33 Power Board Power Consumption

4) Schematic

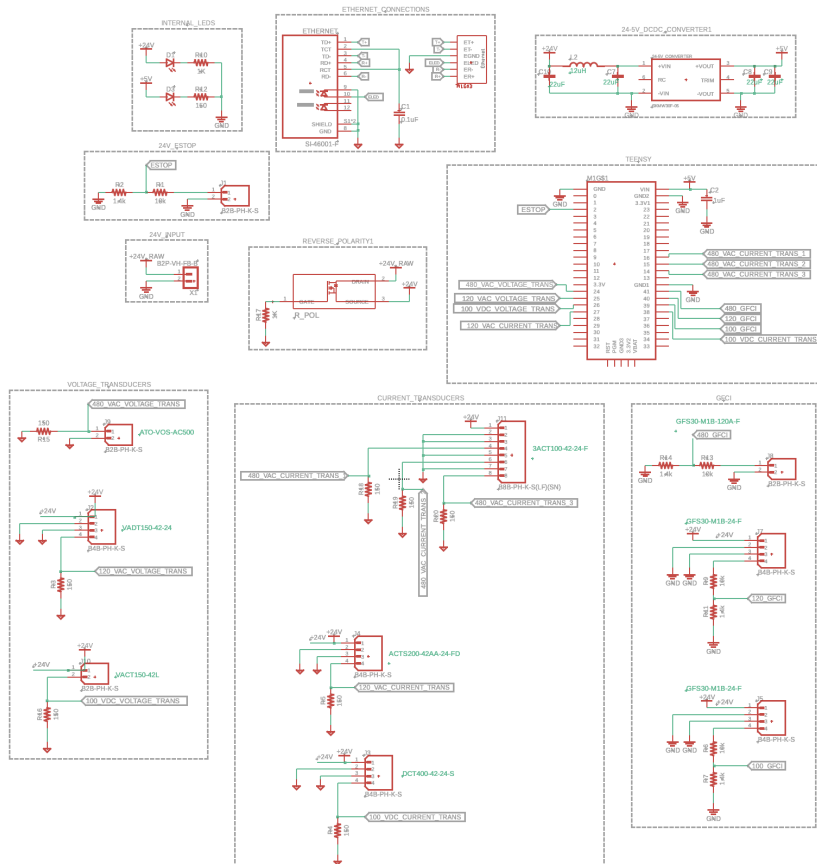


Fig. 116 Power Board Schematic

5) Board Layout

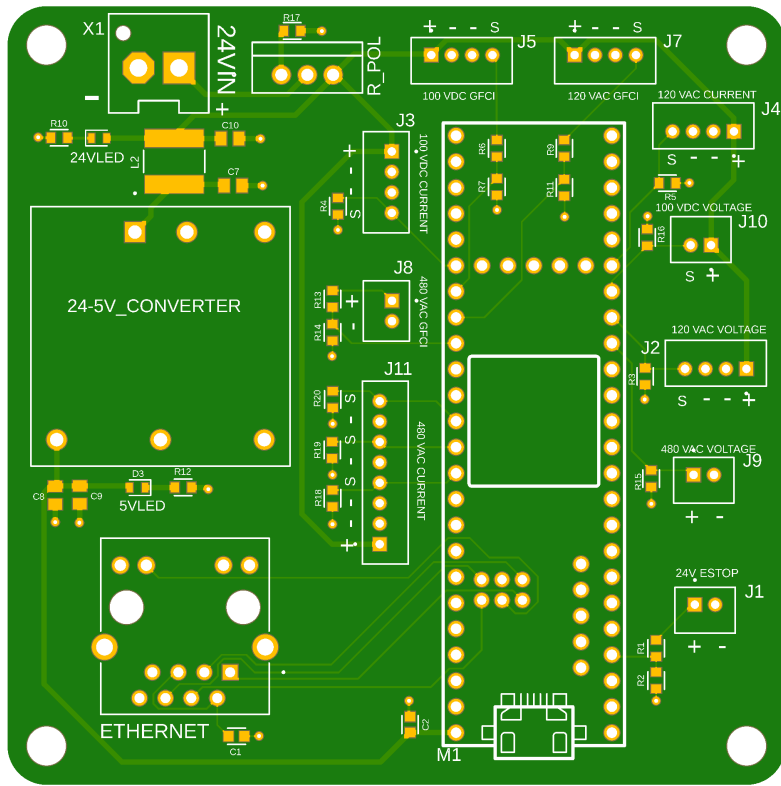


Fig. 117 Power PCB Top

11. Cooling Board

1) Board Overview

The cooling board pumps cooling fluid to all components in the TBM that need to be cooled. This board has three pumps (TBD).

2) Sensor List

Sensors	Part Count	Accuracy	Data Frequency	Nominal Range	Interface Type	Supply Voltage (VDC)
Pump 1	1	TBD	TBD	TBD	TBD	24V
Pump 2	1	TBD	TBD	TBD	TBD	24V
Pump 3	1	TBD	TBD	TBD	TBD	24V

Table 34 Specifications of Pumps

3) Power Consumption

Component	Component Count	Current Draw Per Component (mA)	Total Current Draw (mA)	Power Consumption (W)
Pump 1	1	TBD	TBD	TBD
Pump 2	1	TBD	TBD	TBD
Pump 3	1	TBD	TBD	TBD
Teensy 4.1	1	250	250	1.25
Totals				TBD

Table 35 Cooling Power Consumption

4) Schematic [N/A]

5) Board Layout [N/A]

C. Excavation Harnessing

Controlling the excavation motor is a pre-manufactured motor controller from a third party, Kelly Controls. To interface with the rest of the TBM the excavation board has two forms of communication to integrate motor controls with the same software architecture as the rest of the machine: read-only broadcast type CAN, and analog signaling. This means the loss of the CAN bus does not result in the loss of control of the motor controller. During normal operation, the CAN bus communication method is preferred for its increased scope of feedback information. The cables and connectors for these modes of communication are separated to ensure minimal EMI on the CAN bus and ease of service and troubleshooting during in-field operations.

In normal operation, the CAN bus is used in a ‘read-only’ mode while either simulated or real physical controls (for bench testing or in-situ troubleshooting) are performed via the analog inputs of the motor controller. Additionally, standard serial receive and transmit pins are provided on the Kelly controller making direct connection to the motor controller itself possible using the provided software or a Bluetooth connection. Although each provides a varying amount of information, together they provide redundant troubleshooting capabilities.

Some higher-level controls are simulated with the excavation board rather than requiring a dedicated physical extension to the ground level. The pre-charge and contactor circuits are controlled through the excavation board, capacitor discharge is handled through these two circuits and the control of the DC rectifier (see power section below for more information). Energizing the motor and controller requires an established connection with the excavation board, reducing the risk of unsafe operation. Combined with the layers of redundant communication and operation, this ensures efficient and effective troubleshooting in situ.

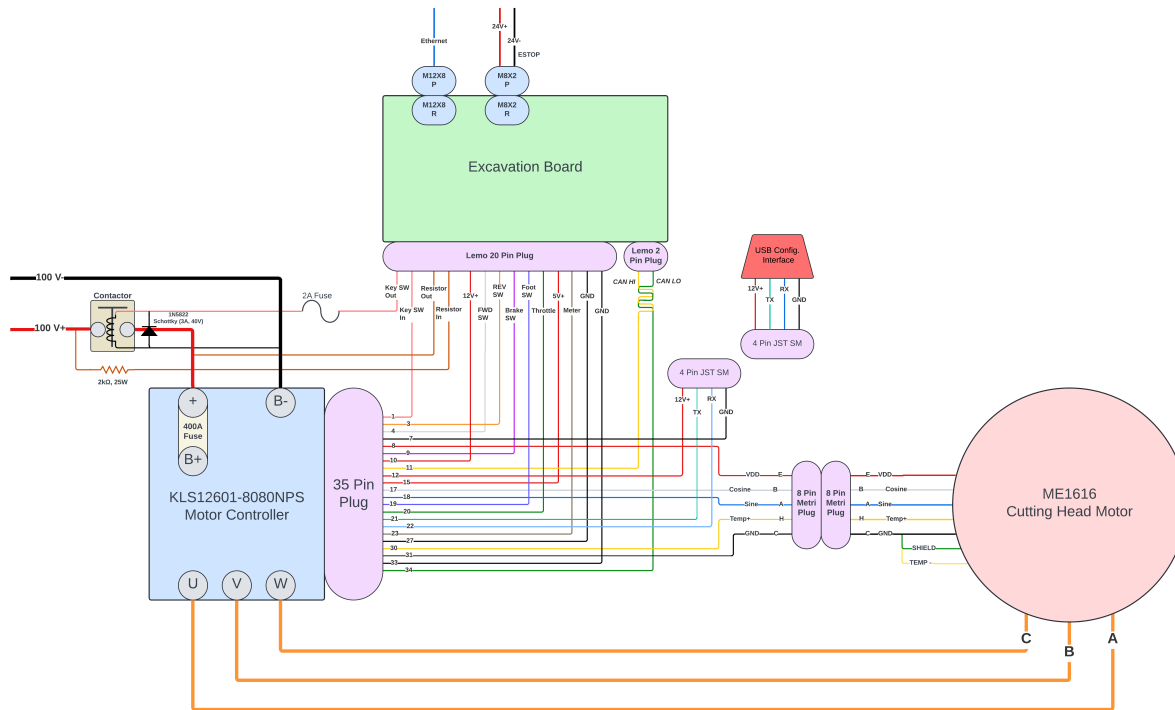


Fig. 118 Excavation Subsystem Diagram

XV. High Power

A. General Overview

The high-power system is designed with strict adherence to regulatory standards, with safety and functionality as top priorities. All protective equipment, monitoring sensors, and power interfaces are housed within a high-power enclosure to ensure secure and reliable operation. There are monitoring LED's and test points for 480VAC, 120VAC, and 100VDC located on the front of the panel. Power is supplied by a TBC-provided three-phase, 480VAC, 100kW generator, which distributes energy through multiple pathways. The total expected load on this generator is around 36.6 kW, which is well below the maximum power output of the generator.

B. Power Budget

The generator's two 120VAC auxiliary outlets, each rated at 20A, are used to support essential subsystems. One of these 120VAC outlets powers a 1.5kW air compressor for inflating TBM grippers, while the other supports a 24V, 960W AC-to-DC converter, 2 18W cooling fans and the 480VAC GFCI. This 24V power supply has an inrush current of 15A and a sustained 9A current draw at 120VAC. This power supply provides power to four above-ground PCBs and all monitoring sensors across the system's power lines.

The system includes a 15kVA transformer that steps down 480VAC to 120VAC to support various subsystems. The 120VAC output is used to power two redundant 12V, 3000W power supplies located in the rear of the TBM, as well as a 24V, 480W power supply dedicated to two motors integral to the tunnel support system. Additionally, the 120VAC powers heating elements as part of the same support system. The total expected load on these power supplies is approximately 2200W, while the overall load on the transformer, including power for the heating elements and 24V power supply, is approximately 9000W.

In a separate stage, the system's rectifier converts 480VAC to 100VDC, capable of delivering a maximum output current of 300A. This AC-to-DC converter is designated to provide power to our main drive motor that spins the cutting head. The main drive motor has a max expected load of 25kW, which is 250A of current from the rectifier.

C. Protective Equipment

The high-power enclosure houses a range of protective equipment to ensure safe operation. Designed to remain closed during normal operation, the enclosure automatically disconnects all power outputs when opened, immediately cutting power to the machine. An emergency stop (ESTOP) button is mounted on the front of the enclosure, providing a quick means to disable power to all outputs. A second ESTOP is located on the operator's table, offering another convenient shutdown point for added safety.

The system includes three contactors, each rated for specific current loads to ensure reliable power distribution. The primary 480VAC contactor, rated at 38A, manages the main power feed. Downstream of the transformer, a 95A-rated contactor is installed to handle all current demands for the TBM. Following the rectifier, a 350A contactor safely exceeds the maximum expected load of 250A. Each contactor operates on a 24V control logic and is governed by safety relays that disconnect power in the event of a fault. The two primary fault conditions are a GFCI trip or an ESTOP activation.

Ground Fault Circuit Interrupters (GFCIs) are installed on the 480VAC, 120VAC, and 100VDC lines, each rated for its specific voltage to provide comprehensive protection. To prioritize personnel safety, each GFCI has a sensitivity setpoint of 5mA, minimizing the risk of harm in the event of a fault. The normally-closed (N/C) contacts of the GFCIs, which open upon detecting a fault, are integrated with safety relays that control the contactors supplying power to each respective system. This configuration ensures prompt disconnection of power to any affected system, increasing overall operational safety.

Breakers have been specified for both the input and output sides of the transformer and rectifier to protect equipment and prevent cable insulation failure if currents exceed their rated limits. For the transformer, a 25A input breaker and a 90A output breaker safeguard both upstream and downstream components and cabling. The rectifier features a built-in 80A breaker; although this exceeds the expected current load, the input cabling for the rectifier is specified accordingly to manage any unexpected current surges above the 250A load. On the rectifier's output side, a 250A breaker is selected based on the requirements of the main drive motor, rated at 250A. While this rating matches the motor's capacity, the motor is not anticipated to operate at full load.

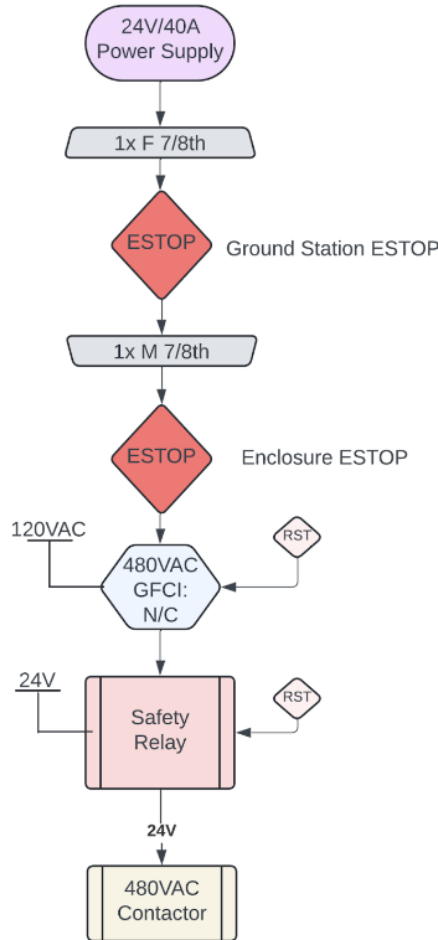
There are voltage and current monitoring sensors for each power distribution. All of these sensors have an analog output which collects data that is sent back to the ground station for interpreting.

D. 2 Step Re-energization

The system is equipped with a two-step re-energization process that is entirely mechanical. Although competition rules allow for software in this process, we have chosen a fully mechanical approach for increased reliability. The first possible fault is triggered by an ESTOP activation. When an ESTOP is pressed, a safety relay within the high-power enclosure cuts power to the 480VAC contactor, shutting down power to the entire machine. To re-energize, the ESTOP must be released, and a manual reset button must be pressed to reset the safety relay, establishing a two-step, purely mechanical reset sequence.

In the case of a GFCI fault, the normally-closed (N/C) contact opens, prompting the safety relay to disconnect power from the contactor. After this occurs, a manual reset button on both the GFCI and safety relay has to be pressed. GFCI faults can occur independently on the 480VAC, 120VAC, or 100VDC lines, allowing targeted shutdowns while maintaining system protection across all voltage levels. The diagram below represents how the 2-step reenergization process works for both 480VAC and the 100VDC/100VAC faults.

2 STEP RE-ENERGIZATION LOGIC (480V)



2 STEP RE-ENERGIZATION LOGIC (120VAC & 100VDC)

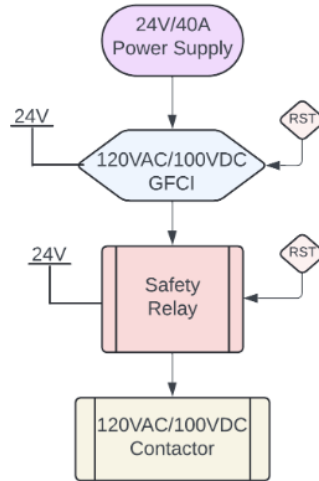
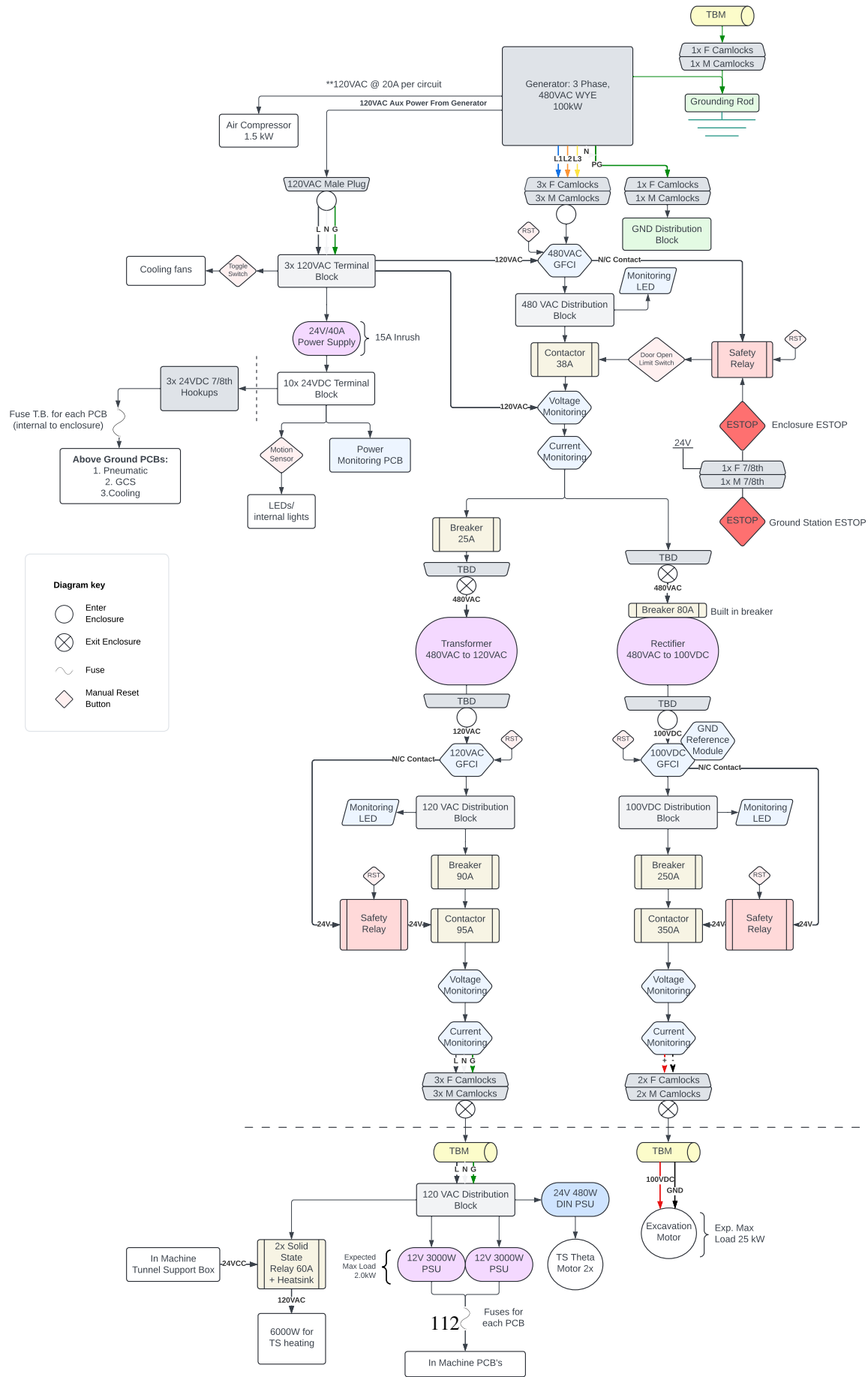


Fig. 119 2 Step Re-energization Logic



E. Completed

XVI. TBM Production Schedule

A. Provide a Breakdown of What Has Been Produced Already vs What Still Needs to Be Produced

B. Already Produced

- **Software**
 - GUI
 - Manual and Autonomous Behavior Tree
 - Excavation Motor Test
 - Hexapod Actuators Test
 - RIMU Position Data Measurements
- **Electrical**
 - Seven RevA Electrical Boards
 - Wire Harnessing Diagram
 - High Power Harnessing Diagram
- **Mechanical**
 - All Machine CAD
 - Front Section of the machine structure
 - Tunnel Support Soil Segment Test
 - Tunnel Support Nozzle Test
 - Select Machine Structure Weldments

C. Needs to Be Produced

- **Software**
 - Tunnel Support Controls in Python
 - Software Unit Testing Harness
 - Python Guidance Navigation and Control
 - Software Integration
 - Software HITL(Hardware In The Loop) Testing for each subsystem
 - Excavation Drive System Test
 - Hexapod Push Test With Front Section
 - Gripper Test
 - Tunnel Support Print Test
- **Electrical**
 - All Revision B Electrical Boards
 - Electrical Boxes Manufacturing
 - Machine Wire Harnessing
 - High Power Distribution System Assembly
 - Electrical System Integration
- **Mechanical**
 - Launch Stand Push Plate CAD
 - DAWGs(Gantries) CAD
 - Electrical Boxes CAD
 - Grippers Manufacturing
 - Hexapod Manufacturing
 - TBM Back Section Manufacturing
 - Cooling Plate Manufacturing
 - GCS Manufacturing
 - Launch Stand Push Plate Manufacturing
 - DAWGs(Gantries) Manufacturing
 - Mechanical Integration

XVII. Full TBM Functional Test Program

A. Provide Minimum Viable Test Plans for Critical Machine Systems

- High power distribution testing
- Software Network Testing
- Hexapod Software Testing
- Excavation Software Motor Testing
- Gripper Inflation Testing
- GCS Pump Testing
- Simultaneous Hexapod and Excavation Motor Testing

B. Provide All Available Test Results of Tests Already Conducted

- Hexapod Moves
- Excavation Motor moves based on our PWM signal

XVIII. Hazardous Materials

A. None

There are no hazardous materials being used for CU Hyperloop TBM.



Fig. 121 Hazardous Materials

XIX. Materials Injected into the ground

A. ACP 214

The anti-clay polymer used will be injected into the ground. ACP 214 is in accordance with GHS classification of the OSHA Hazard Communication Standard (29 CFR 1910.1200). For more information regarding the environmental safety of ACP 214 please follow the following link ACP 214 Safety Data Sheet.

XX. Description of Safety Features

A. Mechanisms to mitigate a Complete loss of TBM Power

Hardline Power + operational "Don't Unplug" policy. IP65 steel high-power distribution system. Bolt in connectors. High power distribution current and voltage monitoring.

B. Single Points of Failure withing the TBM

Single points of failure include:

- Components in the exca-train (Motor controller, motor, gearbox, exca-shaft, couplers, etc.)
- Loss of control over any hexapod actuators
- Soil hose malfunction/rupture
- Compressor failure
- Loss of High Power systems
- Router
- Rectifier failure
- Transformer failure
-

C. Recovery Plan if TBM becomes Immovable

In the event that the machine becomes immovable underground, we have budgeted \$250 in our Tools and Consumables budget for shovels to retrieve the TBM (in the event that there are no excavators available on site). We will then remove machine shells, forcefully if necessary, exposing designated lift points. Lifting straps will be attached and the machine will be removed from the ground.

D. Description of Failure Modes

- Launch Stand tipping - should thrust force exceeds the moment created by the weight of the machine on the launch stand (and additional weight placed on the launch stand), the machine will tip backward, not penetrating the ground.
- Gripper Puncture - a sharp rock or abrasion over the course of the dig may puncture inner tubes.
- High power distribution failing under poor weather conditions
- Gripper Force not high enough - machine will slide backward (during a push) or not retract forwards (during a pull)
- Cooling or GCS line bursting in the machine and flooding the machine
- Exceed maximum gearbox torque - should we encounter an unplanned obstacle during the dig, our actuators are capable of pushing the cutter head hard enough into the obstacle that we exceed the maximum torque the gearbox is rated for
- motor controller failure
- Actuator bending and breaking due to software misconfiguration
- Tunnel Support theta motor failure - may encounter issues with back driving motors
- Tunnel Support adhesion issues - may be caused by imperfect surface, nozzle distance, nozzle temperature, or surface temperature
- Tunnel Support ejection actuators don't place tunnel support segment in the correct position, or don't eject segment cleanly (broken off pieces etc)

E. Descriptions of Safety Interlocking Mechanisms

Using the software system, we monitor all sensor values and are constantly checking if certain sensor values are within a certain safe interval. If one of those values goes above the unsafe threshold we stop all movement on the machine and wait for further instruction. The other physical interlock we have is the E Stop button. The Estop button is in series with all of the circuit boards, nominally allowing 24VDC power to flow to a pin on each board. If any of the boards read 0VDC on that pin all movement stops on the controls software and the abort signal is propagated to the rest of the system ensuring a safe fast stop of all moving components.

XXI. Budget and Financial Overview

A. Total Budget for 2024-2025 Competition Season

The total budget for the 2024-2025 competition season is \$231,801.25, which includes materials for all sub-teams, tools, and logistics expenses. A 20% cost overrun has been added to all expenses to account for fluctuations in pricing and potential unforeseen additional expenses. A list of all the anticipated expenses can be seen in the appendix.

B. Current Financial State

Out of the total budget of \$231,801.25, \$100,328 has been raised from corporate sponsors, grants, and personal donations. Our total budget with no cost overruns is \$193,167.71. Currently, there is \$36,000 in outstanding grants and sponsorships that we expect to receive within the next two months, and \$56,381 of liquid funds available. Assuming we receive the outstanding \$36,000 of funds, this leaves a remaining \$95,473 that needs to be raised to meet our total budget. Of our total budget of \$231,801.25, \$23,203 has already been spent on logistics, overhead, equipment, components, and consumables.

C. Funding Plan

CU Hyperloop is funded by the generosity of our sponsors, in addition to the University of Colorado Boulder, which has provided funding through various grants. Sponsors receive recruitment and advertising benefits depending on the level of donation. Companies that donate materials are recognized as sponsors for the equivalent value of the materials up to the value of \$15,000. A majority of funding comes from companies that sponsor CU Hyperloop. Students reach out to companies through email, calling, LinkedIn, and in-person events, but occasionally through personal connections.

1. Current Industry Sponsors and Contribution Level

D. Team Sponsors

- 1) University of Colorado Boulder, Engineering Excellence Fund
- 2) University of Colorado Boulder, College of Engineering
- 3) Kenesto
- 4) Electro Tabacist
- 5) Trimble
- 6) Kytola
- 7) Aldea
- 8) Chevron
- 9) Mach Industries
- 10) Macnaught
- 11) Norgren
- 12) Premier Pathology
- 13) TrendNet
- 14) Sick
- 15) Automation Direct
- 16) HRE Real Estate
- 17) MEAN WELL
- 18) Wicks
- 19) flexpowermodules
- 20) MatterHackers
- 21) Ansys
- 22) Plus One Robotics
- 23) Sunbelt Rentals
- 24) Marvs Towing
- 25) Master Builders Solutions
- 26) XP Powe
- 27) Master Builders Solutions
- 28) DH Casters
- 29) Automation Direct

E. Anticipated Expenses

Part	Cost (2024-2025)	Quantity	Total Cost
Motor Controller	\$777.00	2	\$1,554.00
Motor	\$1,170.00	2	\$2,340.00
Gear Box	\$5,809.00	1	\$5,809.00
Coupler	\$888.88	1	\$888.88
Motor Controller	\$800.00	2	\$1,600.00
Cutting Head	\$3,732.00	1	\$3,732.00
Tools and Consumables	\$0.00	1	\$0.00
Other	\$3,101.63	1	\$3,101.63
Total			\$19,025.51

Part	Cost (2024-2025)	Quantity	Total Cost
Actuators	\$679.00	6	\$4,074.00
Pneumatic Solenoids	\$209.00	5	\$1,045.00
Pressure Regulator	\$50.00	3	\$150.00
Pressure Transducers	\$220.00	3	\$660.00
Pneumatic Fittings	\$500.00	1	\$500.00
Gripper Chains (225 ft)	\$1,112.16	1	\$1,112.16
Tools and Consumables	\$276.27	1	\$276.27
Other	\$6,805.16	1	\$6,805.16
Total			\$14,346.32

Part	Cost (2024-2025)	Quantity	Total Cost
Cooling Print Plate	\$2,457.65	1	\$2,457.65
Copper Helix	\$2,328.89	1	\$2,328.89
Water Pump	\$749.97	2	\$1,499.94
Tools and Consumables	\$1,725.35	1	\$1,725.35
Other	\$1,000.00	1	\$1,000.00
Total			\$7,286.48

Part	Cost (2024-2025)	Quantity	Total Cost
Machine Plates	\$6,224.00	21	\$6,224.00
Launch Structure	\$4,500.00	1	\$4,500.00
Caster	\$47.53	18	\$855.54
Launch Plates	\$518.50	1	\$518.50
Steel Sheets	\$176.85	8	\$1,414.80
Tools and Consumables	\$4,413.62	1	\$4,413.62
Other	\$3,963.94	1	\$3,963.94
Total			\$17,476.78

Part	Cost (2024-2025)	Quantity	Total Cost
Theta Axis Bearing	\$3,933.41	1	\$3,933.41
Theta Axis Motor	\$327.74	2	\$655.48
Z Axis Actuators	\$131.00	8	\$1,048.00
3D Printer Filament	\$1,367.33	1	\$1,367.33
Nozzle Heating Elements	\$53.53	8	\$428.24
General System Sensors	\$3,856.82	1	\$3,856.82
FDM Custom Nozzle	\$2,500.00	2	\$5,000.00
Segment Ejection System	\$10,000.00	1	\$10,000.00
Tools and Consumables	\$1,000.00	1	\$1,000.00
Other	\$0.00	1	\$0.00
Total			\$26,289.28

Part	Cost (2024-2025)	Quantity	Total Cost
ACP	\$6,000.00	1	\$6,000.00
GCS Pumps	\$157.89	2	\$315.78
275 Gallon Tote	\$500.00	2	\$1,000.00
Tools and Consumables	\$288.86	1	\$288.86
Other	\$1,738.07	1	\$1,738.07
Total			\$9,053.85

Part	Cost (2024-2025)	Quantity	Total Cost
480VAC to 120VAC Transformer	\$1,613.00	1	\$1,613.00
480VAC to 100VDC Rectifier	\$2,530.00	1	\$2,530.00
DC Ground Fault Detector	\$1,396.57	1	\$1,396.57
AC/DC Converter 3000W	\$1,449.00	2	\$2,898.00
High Power Electrical Cabinet	\$2,500.00	1	\$2,500.00
100VDC Wire	\$4,500.00	1	\$4,500.00
Tools and Consumables	\$11,037.62	1	\$11,037.62
Other	\$5,382.00	1	\$5,382.00
Total			\$20,819.57

Part	Cost (2024-2025)	Quantity	Total Cost
PCB Manufacturing Revision A	\$1,500.00	1	\$1,500.00
PCB Components Revision A	\$1,500.00	1	\$1,500.00
PCB Manufacturing Revision B	\$1,500.00	1	\$1,500.00
PCB Components Revision B	\$1,500.00	1	\$1,500.00
Electrical Box Connectors	\$1,000.00	1	\$1,000.00
Tools and Consumables	\$9,486.34	1	\$9,486.34

Other	\$500.00	1	\$500.00
Total			\$7,500.00

Part	Cost (2024-2025)	Quantity	Total Cost
Tools and Consumables	\$5,065.94	1	\$5,065.94
Other	\$1,643.52	1	\$1,643.52
Total			\$6,709.46

F. Summary

Category	Total Cost (2024-2025)
Logistics	\$70,000.00
Tools/Consumables	\$33,294.00
Machine	\$128,507.25
Grand Total	\$231,801.25